



**HAL**  
open science

# Experimental study of flow behaviour and thermal loads in dual bell nozzles

Chloé Génin

► **To cite this version:**

Chloé Génin. Experimental study of flow behaviour and thermal loads in dual bell nozzles. Engineering Sciences [physics]. Université de Valenciennes et du Hainaut-Cambrésis, 2012. English. NNT : 2010VALE0004 . tel-03003250

**HAL Id: tel-03003250**

**<https://uphf.hal.science/tel-03003250>**

Submitted on 13 Nov 2020

**HAL** is a multi-disciplinary open access archive for the deposit and dissemination of scientific research documents, whether they are published or not. The documents may come from teaching and research institutions in France or abroad, or from public or private research centers.

L'archive ouverte pluridisciplinaire **HAL**, est destinée au dépôt et à la diffusion de documents scientifiques de niveau recherche, publiés ou non, émanant des établissements d'enseignement et de recherche français ou étrangers, des laboratoires publics ou privés.



**THÈSE**

Présentée à

---

**L'Université de Valenciennes et du Hainaut Cambresis**

Ecole doctorale ED 072 - Sciences pour l'Ingenieur

---

*en vue de l'obtention du titre de*

**DOCTEUR**

Spécialité: Mécanique énergétique

*par*

**Chloé Génin**

---

**Experimental study of flow behaviour and thermal  
loads in dual bell nozzles**

---

**Etude expérimentale de l'écoulement et des charges  
thermiques dans une tuyère dual bell**

---

Soutenue le 01/02/2010

devant la commission d'examen

Prof. N. Adams	TU Munich, Fakultät für Maschinenwesen	Rapporteur
Prof. A. Chpoun	Université d'Evry, Laboratoire de Mécanique et d'Énergétique	Rapporteur
Prof. L. Labraga	Université de Valenciennes, Laboratoire de Mécanique et Energétique	Examinateur
R. Stark	DLR, Lampoldshausen	Examinateur
Prof. B. Desmet	Université de Valenciennes, Laboratoire de Mécanique Énergétique	Directeur de thèse



# Contents

<b>1</b>	<b>Introduction</b>	<b>1</b>
1.1	Motivation of the study . . . . .	1
1.2	Literature overview . . . . .	2
1.3	Objectives and construction . . . . .	6
<b>2</b>	<b>Nozzle theory and definitions</b>	<b>9</b>
2.1	Space propulsion . . . . .	9
2.2	Nozzle flow . . . . .	11
2.2.1	Isentropic flow in Laval nozzles . . . . .	11
2.2.2	Boundary layer . . . . .	12
2.2.3	Nozzle expansion and flow separation . . . . .	13
2.2.4	Conventional nozzles . . . . .	18
2.2.5	Adaptive nozzles . . . . .	20
2.3	The dual bell nozzle . . . . .	23
2.3.1	Principle . . . . .	23
2.3.2	Performances . . . . .	25
2.3.3	Geometry . . . . .	26
<b>3</b>	<b>Experimental flow study</b>	<b>33</b>
3.1	Test conditions . . . . .	33
3.1.1	Test facility . . . . .	33
3.1.2	Nozzle model . . . . .	36
3.1.3	Instrumentation . . . . .	41
3.1.4	Test configurations . . . . .	45
3.2	General flow behavior . . . . .	49
3.2.1	The two operating modes . . . . .	49
3.2.2	Sneak transition . . . . .	51
3.2.3	Flow model during transition . . . . .	54
3.3	Geometrical study . . . . .	59
3.3.1	The different parameters of influence . . . . .	59

---

3.3.2	Hysteresis effect by the change of operating mode . . . . .	67
3.3.3	Transition duration . . . . .	71
3.4	Side loads . . . . .	79
3.5	Conclusion . . . . .	86
<b>4</b>	<b>Thermal study</b>	<b>87</b>
4.1	Test conditions . . . . .	87
4.1.1	Test bench M11.4 . . . . .	87
4.1.2	Nozzle model . . . . .	89
4.1.3	Instrumentation . . . . .	91
4.1.4	Test sequence . . . . .	98
4.2	Flow behaviour under hot gas conditions . . . . .	101
4.2.1	Pressure distribution . . . . .	101
4.2.2	Transition conditions . . . . .	102
4.2.3	Conclusion . . . . .	105
4.3	Thermal behaviour . . . . .	107
4.3.1	Response time of the system . . . . .	107
4.3.2	Temperature distribution . . . . .	108
4.3.3	Thermography . . . . .	110
4.3.4	Inner wall temperature . . . . .	118
4.3.5	Conclusion . . . . .	122
<b>5</b>	<b>Summary and conclusion</b>	<b>125</b>

# List of Figures

2.1	Definition of the nozzle geometry and its flow variables . . . . .	11
2.2	Flow boundary layer . . . . .	13
2.3	Nozzle flow for various configurations . . . . .	14
2.4	Wall pressure distribution and flow separation . . . . .	15
2.5	Separation conditions as a function of the Mach number . . . . .	16
2.6	Thrust coefficient as a function of altitude . . . . .	17
2.7	Mach number distribution in an ideal nozzle . . . . .	18
2.8	Mach number distribution in TOP nozzle . . . . .	19
2.9	Flow in a plug nozzle and an Expansion-Deflection nozzle . . . . .	20
2.10	Flow in a dual-throat nozzle . . . . .	21
2.11	Extendible nozzle a) at sea level altitude and b) at high altitude . . .	22
2.12	Dual bell nozzle . . . . .	23
2.13	Dual bell flow at sea level mode . . . . .	24
2.14	Dual bell flow at high altitude mode . . . . .	24
2.15	Specific impulse for conventional and dual bell nozzles . . . . .	26
2.16	Wall pressure distribution in dual bell extensions . . . . .	27
2.17	Evolution of the separation condition in CP extension . . . . .	28
2.18	Evolution of the separation condition in NP extension . . . . .	29
2.19	Evolution of the separation condition in a PP extension . . . . .	30
2.20	Geometric parameters in a dual bell nozzle . . . . .	31
3.1	Schema of high altitude chamber . . . . .	34
3.2	Horizontal test rig at the P6.2 test bench . . . . .	35
3.3	Method of characteristics for dual bell design . . . . .	37
3.4	Nozzle model contours . . . . .	39
3.5	Photo of the three tested nozzles . . . . .	40
3.6	Distribution of the wall pressure sensors in the nozzle DB3 . . . . .	41
3.7	Wall pressure measurement . . . . .	42
3.8	Schlieren optic functioning principle . . . . .	42
3.9	Bending tube and dual bell nozzle model . . . . .	44

3.10	Calibration of the side load measurement installation . . . . .	45
3.11	Pressure variation by a typical test of series A . . . . .	46
3.12	Pressure variation by a typical test of series B and C . . . . .	47
3.13	Wall pressure evolution in base and extension nozzles . . . . .	49
3.14	Wall pressure distribution in dual bell nozzle . . . . .	50
3.15	Wall pressure distribution in the vicinity of the inflection . . . . .	51
3.16	Pressure evolution in the extension . . . . .	52
3.17	Values of the NPR at the sneak transition and at the transition . . . . .	53
3.18	Schlieren pictures of the flow before and during the transition . . . . .	54
3.19	Measured points on the shock system . . . . .	55
3.20	Flow jet angle over the separation point position . . . . .	56
3.21	Evolution of the shock system during flow transition . . . . .	57
3.22	Tilted separation plane during flow transition . . . . .	58
3.23	NPR at the transition for the various nozzle geometries . . . . .	59
3.24	Geometry of the recirculation area . . . . .	60
3.25	NPR at the pressure jump in each measurement point . . . . .	61
3.26	Parameters of the inflection angle . . . . .	62
3.27	Mach number in the extension as a function of the inflection angle . . . . .	63
3.28	Transition NPR as a function of inflection angle . . . . .	64
3.29	Transition NPR as a function of base length $L_b$ . . . . .	65
3.30	NPR at retransition for the various nozzle geometries . . . . .	66
3.31	Retransition NPR as a function of the base length $L_b$ . . . . .	66
3.32	Hysteresis effect as a function of the relative extension length . . . . .	68
3.33	Hysteresis as a function of $L''$ for the different test configurations . . . . .	69
3.34	Hysteresis as a function of the geometry . . . . .	70
3.35	Total transition duration as a function of $L'$ . . . . .	71
3.36	Transition duration for various $P_0$ gradients . . . . .	72
3.37	Transition duration relative to NPR gradient . . . . .	73
3.38	Transition and total duration with the relative extension length . . . . .	74
3.39	Position of the separation point in the extension . . . . .	74
3.40	Evolution of the separation position for configurations B1 to B4 . . . . .	75
3.41	Transition front velocity as a function of $L'$ . . . . .	76
3.42	Evolution of the separation point during retransition . . . . .	77
3.43	Side load measurements for various configurations of nozzle DB2 . . . . .	79
3.44	Side loads during flow transition . . . . .	81
3.45	Side load generation for $L_b$ and $L_{ext}$ . . . . .	82
3.46	Side loads during flow retransition . . . . .	83
3.47	Side loads and wall pressure measurements during sneak transition . . . . .	83
3.48	Side loads in ideal and dual bell nozzles . . . . .	85

---

4.1	Principle scheme of test bench M11.4 . . . . .	88
4.2	Dual bell nozzle model mounted on test rig M11.4 . . . . .	89
4.3	Nozzle contour geometry . . . . .	90
4.4	Nozzle model and section contraction geometries . . . . .	91
4.5	Fixation system of the wall pressure sensors on the nozzle . . . . .	93
4.6	Evolution of the measured wall pressure value . . . . .	93
4.7	Temperature and pressure measurement positions . . . . .	95
4.8	Distance $\delta$ between thermocouple and hot inner wall . . . . .	96
4.9	Fixation system for the thermocouples . . . . .	97
4.10	Typical test sequence at M11 test bench . . . . .	99
4.11	Pressure distribution under sea level and high altitude mode . . . . .	101
4.12	Transition conditions as a function of the total temperature . . . . .	103
4.13	Nozzle geometry variation under hot flow conditions . . . . .	104
4.14	Transition NPR as a function of T (cold flow case) . . . . .	104
4.15	Nozzle geometry variation under cold flow conditions . . . . .	105
4.16	Evolution of the temperature along the nozzle wall . . . . .	108
4.17	Position of the thermocouples T1 to T7 in the nozzle wall . . . . .	109
4.18	Temperature distribution along the outer wall . . . . .	110
4.19	Thermal imaging of the nozzle under sea level mode . . . . .	111
4.20	Thermal imaging of the nozzle under high altitude mode . . . . .	112
4.21	Outer wall temperature distribution . . . . .	113
4.22	Outer wall temperature measured with infrared photo and film . . . . .	114
4.23	Evolution of the outer wall temperature for various positions . . . . .	115
4.24	Temperature distribution at various instants of the test . . . . .	116
4.25	Thermal imaging and thermocouple measurement comparison . . . . .	117
4.26	Thermocouple signal correction . . . . .	118
4.27	Distribution of the recovery temperature . . . . .	119
4.28	Thermography and thermocouple measurement at 1 mm to hot wall . . . . .	121
4.29	Comparison of the inner wall temperature . . . . .	122



# Nomenclature

## Latin symboles

A	[m <sup>2</sup> ]	area
$c_f$	[-]	thrust coefficient
F	[N]	thrust
$I_{sp}$	[s]	specific impulse
k	[W/(m.K)]	thermal conductivity
L	[m]	length
L'	[-]	relative extension length $L' = L_{ext}/L_{tot}$
$\dot{m}$	[kg/s]	mass flow
M	[-]	Mach number
R	[m]	radius
Re	[-]	Reynolds number
T	[K]	temperature
P	[bar]	pressure
Pr	[-]	Prandtl number
v	[m/s]	velocity

## Greek symboles

$\alpha$	[°]	wall contour inflection angle
$\beta$	[°]	jet angle
$\delta$	[mm]	boundary layer thickness
$\epsilon$	[-]	area ratio
$\phi$	[W/m <sup>2</sup> ]	local heat flux
$\gamma$	[-]	specific heat ratio
$\mu$	[Pa.s]	dynamic viscosity
$\rho$	[kg/m <sup>3</sup> ]	density
$\Pi$	[N]	thrust loss term

## Indices

0	total conditions
a	ambient
b	base
e	exit
ext	extension
init	initial conditions
sep	separation
trans	transition
retrans	retransition
th	throat
tot	total
w	wall

## Abbreviations

CFD	Computational fluid dynamics
CP	Constant pressure
DLR	Deutsches Zentrum für Luft und Raumfahrt e.V.
EADS	European Aeronautic Defence and Space Company
ESA	European Space Agency
FESTIP	Future European Space Transportation Investigation Programme
FSCD	Flow Separation Control Device
MOC	Method of the characteristics
NASA	National Aeronautics and Space Administration
NP	Negative pressure
NPR	Nozzle pressure ratio $P_0/P_a$
PP	Positive pressure
SSME	Space Shuttle Main Engine
SSTO	Single Stage To Orbit
TDK	Two Dimensional Kinetics program for liquid rocket engines
TIC	Truncated ideal contour
TOP	Thrust optimised parabola

# Chapter 1

## Introduction

### 1.1 Motivation of the study

The constant mass increase for low earth orbit (LEO) payloads imposed in the past new performance requirements on heavy launchers. The current launchers changed from classical tandem to parallel configuration (Ariane IV to Ariane V in Europe, Saturn to Space Shuttle in the USA,...).

The thrust generated by the engines has to lift the heavy launcher and its payload. The thrust is directly proportional to the mass flow through the nozzle. In order to increase the overall lift-off thrust value, solid boosters with their high density exhaust flow are implemented for sea level operation. The boosters of the European launcher Ariane V yield about 90% of the start thrust and burn for about 150 s (up to an altitude of 70 km). Once these are separated, the main stage engine is responsible for the whole thrust generation. The cryogenic main stage engine Vulcain 2 must be started before the lift off for security reasons, in spite of its low thrust compared to the solid booster. The ambient pressure at which the main engine operates covers a wide range: from 1 bar at sea level to almost vacuum at 150 km, when the engine is shut down.

The high temperature combustion chamber exhaust gases are expanded and accelerated by the supersonic nozzle and the thrust value is proportional to the pressure difference between the nozzle exhaust jet and ambience and therefore to the nozzle end section area. Nozzles with high exit area yield better performance. However, over expansion at low altitude (ambient pressure higher than jet pressure) leads due to a negative pressure thrust to performance losses. At a certain value of nozzle pressure ratio (total pressure through ambient pressure, NPR) the flow even separates from the nozzle wall. This limits the nozzle's maximum size.

The problems of over expansion and flow separation in conventional nozzles have created the need for new altitude adaptive nozzle concepts. The dual bell nozzle studied in this work is one of the new concepts proposed to circumvent nozzle geometry limitations.

## 1.2 Literature overview

Many experimental and analytical studies have shown in the 1960's and the 1970's the effects of over expansion. Full scale testing on the J-2S engine at Rocketdyne Division by Nave and Coffey [41] pointed out the non symmetrical character of the flow separation in an over expanded nozzle. Lawrence [28] showed in his PhD. thesis the formation of side loads in over expanded separated nozzles. The consequence of these loads is possible harm of engine, launcher and even payload structure. Current research efforts are still concentrated on the prediction and the prevention of flow separation. The nozzle geometry has to be limited and the optimal high altitude performance cannot be reached.

International aerospace research is interested in new nozzle concepts in the frame of projects regarding reusable single stage space engines (SSTO - Single Stage to Orbit). The European project FESTIP (Future European Space Transportation Investigations Program) studies the possibilities of combustion chamber improvement, the concept of advanced nozzles and turbine technologies ([21], [4], [22] and [19]). Similar research campaigns are also carried out in the USA [20] and Japan [26].

The European Flow Separation Control Device (FSCD) was initiated to study both flow separation in classical bell nozzles and altitude adapting rocket nozzles such as plug nozzles, dual bell nozzles or nozzles with an extendible exit cone. As a result the dual bell nozzle was identified as the most promising concept [9], [18], [48].

The concept of a dual bell nozzle first appears in the literature in 1949 in a study of Foster and Cowles [6] on the conditions and consequences of flow separation in supersonic nozzles. Various solutions were proposed to circumvent the problem of unsteady flow separation that appears to be inevitable in high area ratio nozzles. A forced separation under chosen conditions allows high area ratios with flow stability. The altitude adaptive nozzle concept was patented by Rocketdyne in the 60's as the dual bell nozzle.

The proposed concept of dual bell nozzles consists of a conventional bell type base nozzle linked to an extension nozzle through an abrupt wall inflection angle. Foster and Cowles pointed out an operation with well defined separation characteristics under sea-level as well as under high altitude conditions. The characteristic wall inflection offers a good altitude adaptation, without any moving parts. The flow separation is forced at the wall inflection under sea-level condition. The small area ratio leads to higher thrust compared to a conventional bell nozzle. At a certain altitude, the flow attaches suddenly at the extension wall during the transition from the sea-level to the high altitude operating mode. The high area ratio leads to an optimised high altitude performance.

The first experimental studies on the dual bell concept were performed in the early 1990's, as the state of the art in flow separation comprehension was previously not deep enough to truly understand the phenomena that occur in a dual bell nozzle during the transition from one mode to the other. Cold tests on dual bell models were conducted in 1994 in the USA by Horn and Fischer [20] at Rocketdyne to experimentally verify the theoretical flow behaviour in the nozzle and the existence of two distinct operating modes. The test campaign was then simulated by Goel and Jensen in 1995 [11]. The general flow behaviour was also numerically verified by research groups in Europe (by Karl and Hannemann [23], by Nasuti et al. [39], [46]) or in Japan (by Miyazawa et al.[37]) .

Once the system analysis had proven the advantages of the new nozzle concept, many studies were conducted to better understand the functioning of the system. Experimental studies were made mostly in Europe and Japan: Haidinger performed cold flow and hot flow test campaign in Germany in 1998 [19], Kumakawa et al. [26] and Kusaka et al. [27] both conducted hot gas test campaign on dual bell flow.

Many studies have been conducted to evaluate the potential performance gains of the dual bell nozzle. However, the values found in the literature strongly depend on the application examined. The Future European Space Transportation Investigations Programme (FESTIP) proposed the dual bell concept for future space applications, as sustainer engine for vertical take off, horizontal landing all-rocket-propelled engine (FSS-1) [21] [22]. The performances and the limits of the concept have been investigated. The losses indentified, due to the wall inflection whilst operating in the high altitude mode, were approximated between 0.1% and 1.2% of the total performance.

Manski et al.[29] predicted 1998 an effective launcher mass decrease of 3% using a dual bell nozzle instead of a classical bell nozzle for reusable SSTO vehicle applica-

tions. The authors also evaluated the aspiration drag losses at sea level operating mode to 3 to 4% of the performance.

Hagemann investigated, analytically and experimentally, into the performances of dual bell nozzles. The payload increase was evaluated of 1446 kg gain [18] or 72% using the FSS-1 as reference vehicle and a dual bell geometry with area ratios  $\epsilon_b = 30$  and  $\epsilon_e = 100$  [13]. The aspiration drag losses corresponded to maximum 3% of the performance.

A Japanese research group with Miyazawa et al. [38] calculated the potential specific impulse gain increase of 10 s compared to the reference engines RD180 (first stage engine of Atlas 5) and LE-7A (first stage of H-2A). However, those calculations were made with many assumptions like instantaneous transition and absence of losses during the sea-level mode, so that the performance gain may have been overestimated.

At Beijing Aerospace Propulsion Institute, Zheng et al. simulated the influence of the base nozzle geometry ( $\epsilon_b$  and  $L_b$ ) on the general dual bell performance [65]. A potential impulse increase of 1.8% averaged along the flight trajectory was found.

The influence of the various geometric parameters has already been studied by various authors. Hagemann and Frey [13] researched analytically into the effect of the inflection angle and the nozzle exit angle on the performance. They also proposed an extension contour design using a transcendental function in order to limit the region of negative pressure in the vicinity of the inflection [12]. An experimental parametrical study has been conducted by the author of this work [44] at the DLR Lampoldshausen.

Since 2001, Nasuti and Martelli have worked on dual bell contour optimisation proposing an alternative design method to the method of characteristics (MOC) used in this study (see details in [39] and [40]) for the design of the extension. The results shows numerically better wall pressure distribution, with a shorter inflection region (region in the extension, near the inflection with a negative wall pressure gradient), but no contour has yet been tested to verify the calculation experimentally. Another numerical study [31] investigates into the influence of the inflection angle on the transition time and the performance. In a recent numerical study, Martelli et al. investigated into the influence of film cooling on mode transition [35].

In order to qualify the new dual bell concept for main stage rocket nozzle applica-

tions, the limiting parameters have also been investigated. The two critical questions are the stability between the two operating modes and the evaluation of the potential additional loads compared to conventional nozzles.

Perigo et al. [48] pointed out that during ascent of a rocket engine, combustion chamber fluctuations can lead to small total pressure variation. The buffeting effect around the nozzle induces ambient pressure variation of up to  $+/- 10\%$  at the nozzle end. To ensure a stable flow behaviour, the transition from one mode to the other must resist such variations of the nozzle pressure ratio. A hysteresis behaviour between flow transition and retransition was first documented by Hagemann et al. in an experimental study conducted at the DLR Lampoldshausen [18]. Further experimental studies by Stark et al. [57] and the author of this work [42], [43] were performed in order to quantify and optimise this hysteresis effect. A numerical analysis realised by Karl and Hannemann [23] calculated this effect for an existing nozzle model (experimental results in [18] and [57]).

The second limiting factor for dual bell nozzle application is the generation of additional structural and thermal loads. During mode change, the separation front moves from the wall inflection down to the nozzle lip for the transition and back to the inflection for retransition. The time needed and the amplitude of the generated side loads are critical for the structural loads. Side loads were experimentally measured during various test campaigns e.g. in Europe [18] or in China (by Zheng et al. [65]). A very high side load peak has been measured for some configurations during transition and a smaller by retransition. The tests conducted by Zheng et al. showed no high amplitude load peak, but as the test were made only on retransition, no conclusion can be directly inferred about the behaviour during transition. Numerical study could also show the side loads peak during the change of mode (see details in the study conducted by Martelli et al. in [30] and [31]).

Dumnov et al. [5] studied the wall temperature in the dual bell extension for using low cost heat resistant materials. The concept showed diminished thermal loads in the extension, however, the flow variations were not taken into account. Temperature measurements and numerical simulation were also made to evaluate the thermal loads in a dual bell nozzle ([19] and [18]). The heat fluxes are shown to be reduced by the pressure drop in the nozzle extension.

### 1.3 Objectives and construction

Prior to the implementation of dual bell nozzle in a rocket engine, some questions still have to be answered. The altitude for the change of operating mode is established from the transition and retransition nozzle pressure ratio. The objectives of this Ph. D. thesis was to investigate experimentally the dependency of these two values as well as the hysteresis effect with the nozzle geometry and to optimise the stability of the two flow operating modes. The transition duration had to be measured and the influence of the nozzle geometry pointed out. The additional side loads working on the dual bell contour in comparison to a conventional one were evaluated by varying the NPR for various configurations. Another focus was set on the thermal loads in the extension and in the vicinity of the inflection that are determinant for the implementation of an adapted cooling system.

Numerical studies found in the literature have shown their limits: the grid resolution and the chosen turbulence model have a high influence on separation conditions in a dual bell nozzle. Furthermore, the hysteresis effect between transition and retransition conditions make the prediction of the flow operating mode for steady calculations difficult. For this reason this study focussed on an experimental investigation, in order to collect information which will be necessary for the validation of future numerical studies.

Three sub scale nozzles with various geometrical parameters (inflection angle  $\alpha$ , base length  $L_b$  and total length  $L_{tot}$ ) were tested at the DLR's cold gas test bench P6.2. The test were performed under ambient pressure with positive and negative ramping of the feed pressure  $P_0$ . Two of the three contours were then shortened to collect information on the influence of the extension length on the flow behaviour. Schlieren pictures of the flow in the shortened nozzles allows the observation of flow phenomena inside the nozzle extension. Pressure and side load measurements were made for each nozzle configuration to determine the transition conditions, the hysteresis and the transition duration. Side loads measurements were recorded for the various configurations to experimentally confirm the peak of structural loads mentioned in the literature.

A second test campaign was conducted at the sub scale hot air test bench M11.4. A nozzle contour was designed and tested in order to evaluate the thermal loads. Temperature measurements were made in the nozzle wall and observation were obtained using an infra-red camera under steady conditions (constant value of NPR).

In the first part of this work, the flow relations and phenomena are presented for conventional and dual bell nozzles. A description of the cold gas test set up introduces the experimental parametric study. Flow observation using schlieren installation yields a view in the dual bell nozzle flow transition. The side loads generation is then investigate for the various nozzle geometries and configurations. To conclude, the parameters for dual bell geometry optimisation and flow transition are summarised. The measurement and evaluation of wall temperature and thermal loads in this new nozzle concept are also dealt with.

The extensive experimental study presented in this work offers a new frame for the dual bell application as launcher main engine.



# Chapter 2

## Nozzle theory and definitions

The following chapter briefly presents some of the important definitions in nozzle flow, characterises conventional nozzles and describes the state of the art in the research on a new concept of altitude adaptive nozzle: the dual bell nozzle.

### 2.1 Space propulsion

The principle of space propulsion is the application of a force to the launcher through the expulsion of combustion gases at high velocity. The equations of mechanics, thermodynamics and chemistry are the basis of propulsion theory. The propellants react in the thrust chamber to form hot gases which are then accelerated and ejected through a supersonic nozzle. A large part of the thermal energy generated during combustion is transformed into kinetic energy. The exit velocity attained by the flow is defined by the nozzle geometry, in particular the geometry of the diverging part. Nozzles currently represent the most promising elements for optimisation in space propulsion applications.

The total impulse delivered from the engine is the integration of the thrust over time. The specific impulse is calculated according to:

$$I_{sp} = F/(\dot{m}g_0) \quad (2.1)$$

for constant thrust  $F$  and mass flow  $\dot{m}$ . The thrust is the reacting force of the gases ejected at high velocity. For a rocket operating under varying ambient pressure  $P_a$ , the thrust can be written as follow:

$$F = \dot{m}v_2 + (P_e - P_a)A_e \quad (2.2)$$

The first term, the momentum thrust, is the product of the propellant mass flow  $\dot{m}$  and its averaged velocity  $v_2$  (relative to the vehicle). The second term, the pressure thrust depends on the altitude. It is the product of the difference between the nozzle exit pressure  $P_e$  and the ambient pressure  $P_a$  and the nozzle exit cross section area  $A_e$ . The pressure thrust varies with altitude and reaches its maximum value for  $P_a = 0$ , under vacuum conditions. The nozzle geometry defines the remaining parameters: the throat cross section  $A_{th}$  fixes the mass flow; the diverging part sets the exit pressure and velocity. A large area ratio  $\epsilon = A_e/A_{th}$  assures high performance under high altitude conditions (term  $P_e - P_a > 0$ ). At sea level, a smaller area ratio limits the losses due to the negative pressure thrust term and thus increases the performance.

The thrust coefficient is the ratio of the thrust to the throat section area and the total pressure:

$$c_F = \frac{F}{P_0 A_{th}} \quad (2.3)$$

Its maximum value is reached when  $P_e = P_a$  and corresponds to the optimum thrust coefficient. This coefficient is used to describe the influence of chamber pressure and altitude variations for a given nozzle geometry.

## 2.2 Nozzle flow

### 2.2.1 Isentropic flow in Laval nozzles

The ideal flow through a nozzle corresponds to the thermodynamic expansion of the combustion chamber exhaust gases. In the ideal case, the flow is assumed to be homogeneous, steady, adiabatic non reacting and uniform in every normal section and the boundary layer is neglected. The flow can be modelled as an isentropic flow process. Its characteristics are obtained from the three following relations: the conservation of mass, the conservation of energy and the perfect gas law. The isentropic relations can be derived from these assumptions. The flow properties are thus related to each other and to the nozzle geometry. The definition of the flow characteristics in a nozzle are summarised in figure 2.1.

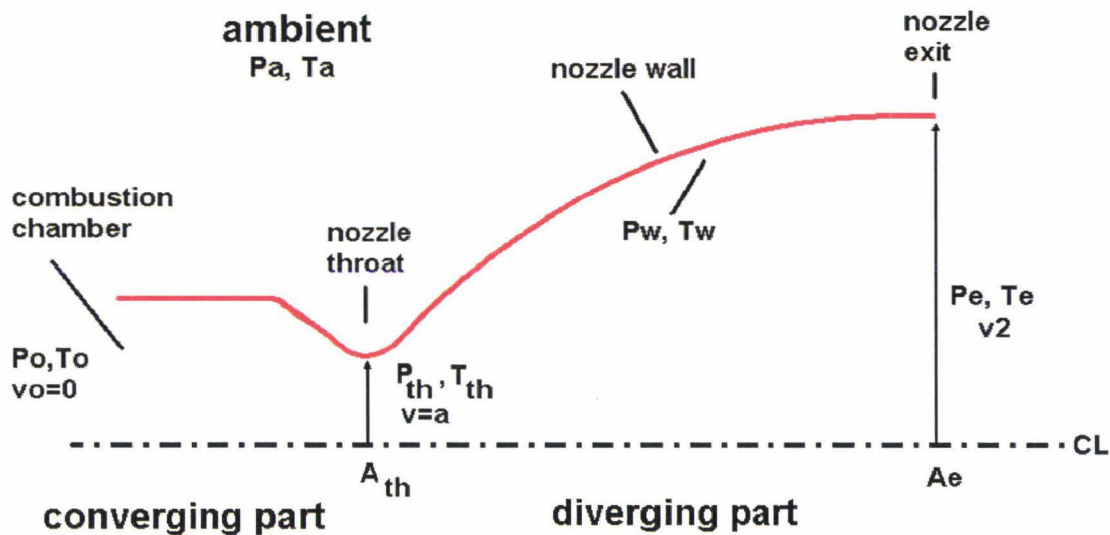


Figure 2.1: Definition of the nozzle geometry and its flow variables

The temperature ratio between the total conditions and temperature at a given position  $T_0/T(x)$  is related to the local Mach number  $M(x)$  according to equation (2.4):

$$\frac{T_0}{T(x)} = 1 + \frac{\gamma - 1}{2} M(x)^2 \quad (2.4)$$

The variable  $\gamma$  is the specific heat ratio and is assumed constant in perfect gas flow. The pressure ratio  $P_0/P(x)$  between total and local conditions can be calculated

with a similar relation:

$$\frac{P_0}{P(x)} = \left(1 + \frac{\gamma - 1}{2} M^2(x)\right)^{\frac{\gamma}{\gamma - 1}} \quad (2.5)$$

The variable  $\epsilon(x) = A(x)/A_{th}$  corresponds to the area ratio between the local area in the nozzle and the throat area and is related to the Mach number in the flow at a given nozzle section by the following relation:

$$\epsilon(x) = \frac{A(x)}{A_{th}} = \frac{1}{M(x)} \left( \frac{1}{\gamma + 1} \left(1 + \frac{\gamma - 1}{2} M(x)^2\right) \right)^{\frac{\gamma + 1}{2(\gamma - 1)}} \quad (2.6)$$

The velocity reached by the flow at the nozzle end can be calculated as a function of the flow characteristics, the total conditions, and the exit flow pressure  $P_e$  with relation (2.7).

$$v_2 = \sqrt{\frac{2\gamma}{\gamma - 1} RT_0 \left(1 - \left(\frac{P_e}{P_0}\right)^{\frac{\gamma - 1}{\gamma}}\right)} \quad (2.7)$$

The variable  $R$  stands for the specific gas constant, ratio of the universal gas constant  $\mathbf{R} = 8.314 J.K^{-1}.mol^{-1}$  over the molar mass  $\mathbf{M}$  (e.g.  $R = 287.06 J.kg^{-1}.K^{-1}$  for dry air). Further information on nozzle flow can be found in Sutton et al. in [59].

## 2.2.2 Boundary layer

In the vicinity of the wall, the isentropic flow model fails due to the flow viscosity. The flow is slowed down, the velocity decreases in the direction normal to the wall, and reaches zero at the wall (fig. 2.2). The thickness  $\delta$  of this boundary layer is defined as the limit at which the velocity reaches 99% of the undisturbed flow velocity  $U$ . It is a function of the Reynolds number  $Re$ . The flow properties in the boundary layer can be calculated using the following Prandtl relations:

$$u \frac{\partial u}{\partial x} + v \frac{\partial u}{\partial y} = -\frac{1}{\rho} \frac{\partial p}{\partial x} + \nu \frac{\partial^2 u}{\partial y^2} \quad (2.8)$$

$$\frac{\partial p}{\partial y} = 0 \quad (2.9)$$

$$\frac{\partial u}{\partial x} + \frac{\partial v}{\partial y} = 0 \quad (2.10)$$

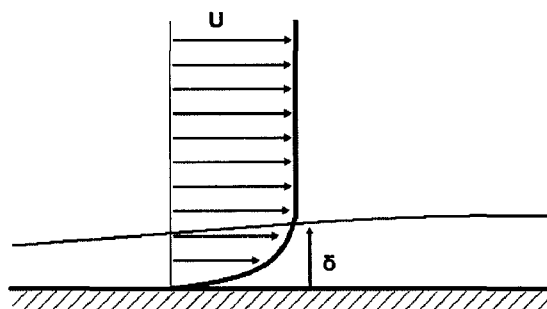


Figure 2.2: Flow boundary layer

The flow temperature increases in the vicinity of the wall (when not cooled): a part of the kinetic energy is converted back to thermal energy. Significant heat transfer take place between the boundary layer flow and the nozzle wall. The flow temperature at the wall  $T_w$  can be approximated with the adiabatic recovery temperature:

$$T_w = T_E \left( 1 + \frac{\gamma - 1}{2} M^2 Pr^{1/3} \right) \quad (2.11)$$

The term  $T_E$  is the flow temperature at the edge of the thermal boundary layer. The Prandtl number  $Pr$  is the ratio of viscous to thermal diffusivity. The temperature boundary layer thickness  $\delta_t$  is a function of the Prandtl number:  $\delta/\delta_t = \sqrt{Pr}$ .

### 2.2.3 Nozzle expansion and flow separation

During ascent of a rocket engine, the ambient pressure falls from 1 bar at sea level to vacuum at very high altitudes. The thrust generated by the nozzle is then a function of the altitude via the pressure thrust term. The flow is said to be adapted when the exhaust pressure corresponds to the ambient pressure (pressure thrust is equal to zero). Figure 2.3 represents the flow in a conventional nozzle for various configurations. The first graph 2.3 a) illustrates the flow in an adapted configuration:  $P_e = P_a$ .

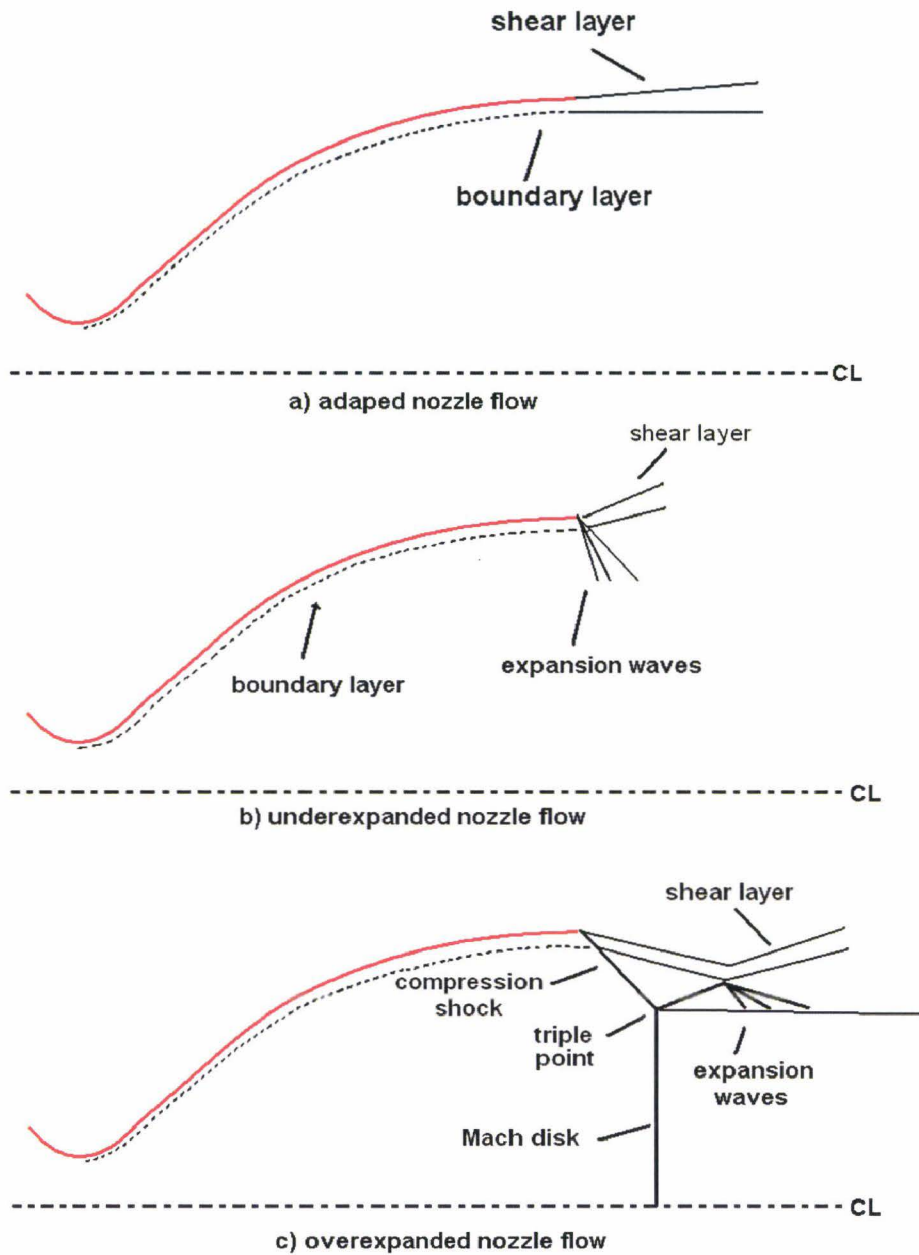


Figure 2.3: Nozzle flow for various configurations

At higher altitudes, the ambient pressure becomes smaller than the nozzle exit pressure  $P_e$ , which is only a function of the total pressure  $P_0$  for a given geometry. The pressure thrust term becomes positive. The flow is then said to be underexpanded and is illustrated in figure 2.3 b). Flow expansion takes place partially outside of the nozzle through expansion waves at the nozzle lip.

The third possible configuration is over expansion of the flow: the exit pressure  $P_e$

is lower than the ambient pressure  $P_a$ . The pressure thrust term is then negative. The flow must adapt to the ambient conditions: a compression shock appears at the nozzle lip. The shock system is represented in figure 2.3 c).

Under sea level conditions, as the ambient pressure is very high compared to the exhaust gas pressure, significant over expansion can take place, leading to a flow separation from the nozzle wall. Figure 2.4 illustrates the pressure distribution along the nozzle wall under vacuum conditions and for a value of the ambient pressure  $P_a$  much higher than the pressure at the nozzle exit  $P_e$ . The wall pressure decreases along the nozzle wall. When the pressure reaches the critical value  $P_{sep}$ , the flow separates from the wall and a recirculation region develops then at the wall (refer to Lawrence [28] and Nave and Coffey [41] for additional details).

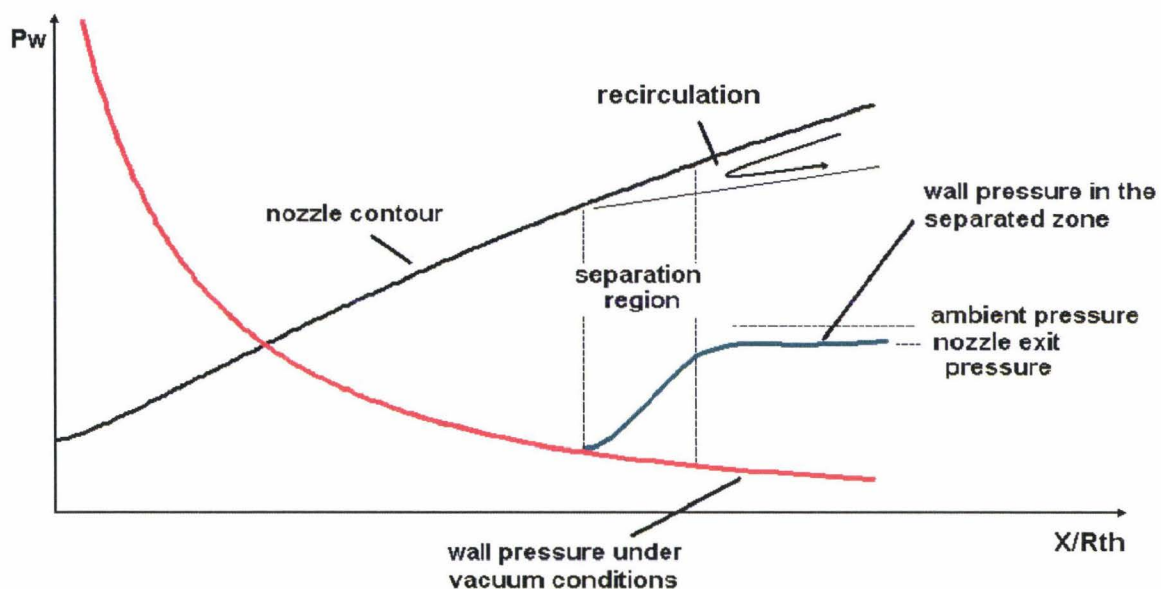


Figure 2.4: Wall pressure distribution and flow separation

The effects of over expansion and flow separation in nozzles are of great interest for rocket engine applications. Many studies have investigated into the calculation of the critical pressure value which can be approximated with different criteria. One of them is currently in use in Europe to approximate the separation pressure: the Schmucker criterion [55].

$$\frac{P_{sep}}{P_a} = (1.88M - 1)^{-0.64} \quad (2.12)$$

A simple relation developed by Stark [56] gives very good separation prediction especially for cold gas nozzle flow.

$$\frac{P_{sep}}{P_a} = \frac{1}{M_{sep}} \quad (2.13)$$

These two criterion use the pressure ratio  $P_{sep}/P_a$  to define the separation conditions at each axial position. In the following sections, the separation will be defined by the pressure ratio:

$$\frac{P_0}{P_a} = \frac{P_0}{P_{w,sep}} \frac{P_{w,sep}}{P_a} \quad (2.14)$$

To each axial position corresponds a value of the separation nozzle pressure ratio  $P_0/P_a = NPR$ . Figure 2.5 illustrates the flow separation condition. The ratio  $P_{sep}/P_a$  is only a function of the Mach number and hence of the geometry. When varying the conditions (NPR value), the curves of  $P_w/P_a$  and  $P_{sep}/P_a$  intersects: separation conditions are reached.

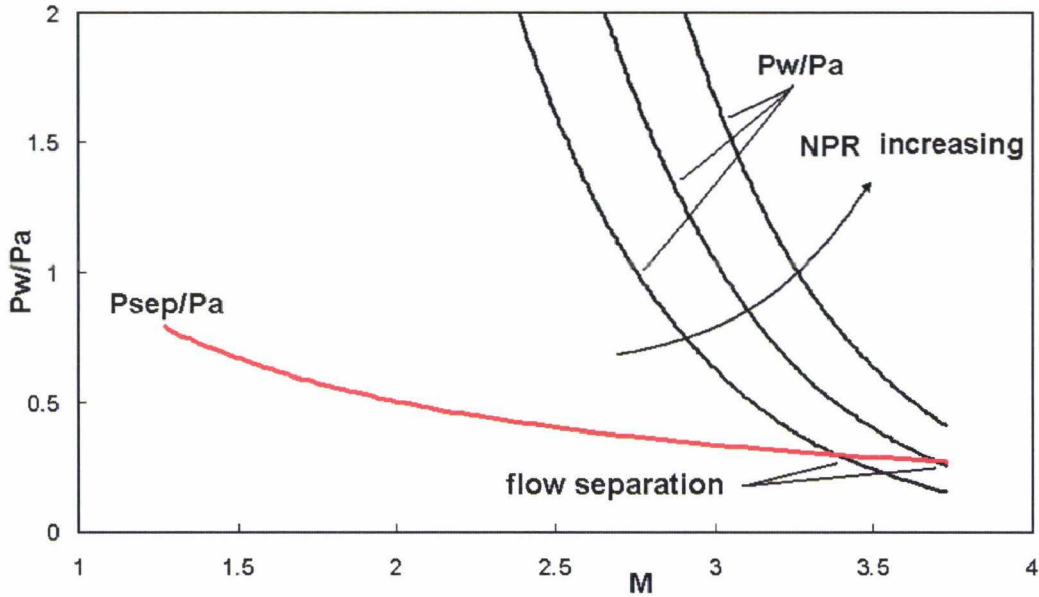


Figure 2.5: Separation conditions as a function of the Mach number

The higher ambient pressure leads to an increase of the thickness of the subsonic part of the boundary layer. This induces a recompression shock in the supersonic flow and to the separation of the flow from the wall. The backflow of the ambient air is unsteady and unsymmetrical and therefore generates high side loads on the nozzle. The high vibrations induced can damage the nozzle and also the rocket

structure and its payload. The separation phenomena are complex and still under research in many studies (for example ref. [3], [7], [8], [52] and [58]).

As the thrust generated by a nozzle depends on the altitude, the optimal efficiency is only reached at a given altitude. Figure 2.6 illustrates the difference between the thrust coefficient generated by an ideally nozzle that would be adapted to every altitude and the value reached by a real nozzle. At low altitudes, a smaller area ratio increases the thrust coefficient of the ideal adapted nozzle. When the altitude corresponds to its design altitude, the conventional nozzle yields its optimal performance. At high altitudes, the adapted nozzle leads to a better performance thanks to a higher area ratio.

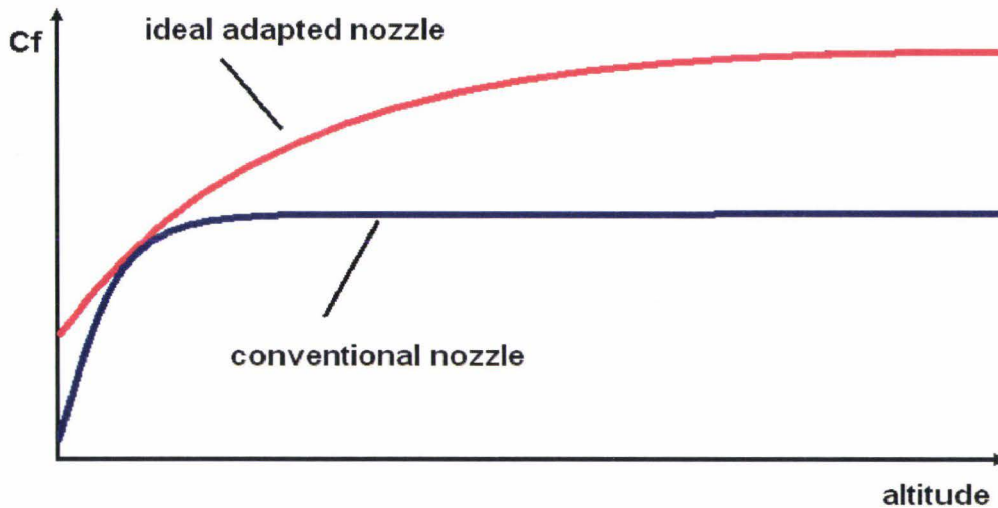


Figure 2.6: Thrust coefficient as a function of altitude

Conventional nozzles in use for rocket engines are thus designed to minimize flow separation effects: the length of the nozzle is shortened in order to maintain the wall pressure value over the critical pressure value. This however limits the potential high altitude performance of the nozzle. In order to improve both sea level and high altitude performance, research takes a great interest in altitude adaptive nozzle concepts.

### 2.2.4 Conventional nozzles

Conventional converging-diverging Laval nozzle contours feature various geometries, leading to various flow behaviours. The first nozzles in use were designed with a conical divergent section. The contour half angle is chosen as a compromise of length, weight and performance; a value of about  $15^\circ$  has shown good results for rocket engine applications. They still are in use for small applications, because they are well-known and easy to design and manufacture.

As part of the bell nozzle family, two other geometries are of particular interest for propulsion research: the ideal nozzle and the thrust optimised nozzle. The ideal nozzle is designed, usually using the method of the characteristics, in order to generate an parallel exit flow thus limiting the divergence losses.

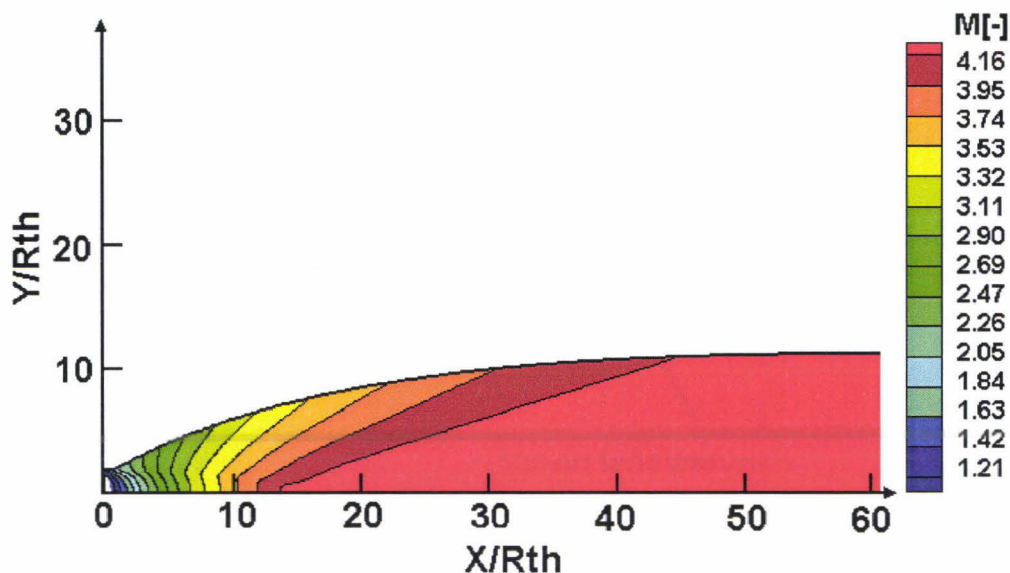


Figure 2.7: Mach number distribution in an ideal nozzle

The method of characteristics yields a first approximation of steady, two-dimensional, irrotational and compressible flow behaviour. It results from the equation of gas dynamics, the irrotational property of the flow and the perfect gas law. The theory is described in detail by Zucrow in [66]. The main drawback of such a geometry is the significant length necessary to attain a fully parallel flow: even longer than a conical nozzle for a comparable exit area. The problem of length and weight can be circumvented by shortening the nozzle. In the last part of the nozzle, the wall angle variation is very low: the impulse gain in this part is negligible compared to the additional friction losses at the wall. The ideal contour can be shortened down to 75% of the reference conical nozzle length without important divergence losses or

performance decrease into a truncated ideal contour (TIC). Figure 2.7 illustrates the Mach number distribution in an ideal nozzle calculated using an in-house program based on the method of the characteristics. The contour is defined by its throat geometry ( $R_{th}$ ), the total conditions of the flow ( $P_0$  and  $T_0$ ), the ambient pressure and the design Mach number reached by the flow at the nozzle end.

The thrust optimised contour (TOC) was first proposed by Rao in the 60's ([49] and [50]) and is designed to generate an optimal thrust for a given throat geometry and nozzle length. The contour presents a high divergence angle at the throat which leads to a greater expansion than in a comparable ideal contour. The flow is then deflected to limit the divergence losses at the exit area, this leads to a weak internal shock at the interface between the throat radius and the deflection contour. The contours can be approximated with a parabola (TOP - Thrust Optimised Parabola), which simplify the design but amplify the shock generation. The Ariane V main engine (Vulcain II) and the American Space Shuttle Main Engine (SSME) are both designed as TOP nozzles. However the absence in ideal nozzles of any shock wave generation at the interface between the start radius and the diverging part makes the ideal (or TIC) nozzle the most interesting as basis for new alternative nozzle contours. The distribution of the Mach number in a TOP nozzle is represented in figure 2.8; the discontinuity is caused by the internal shock.

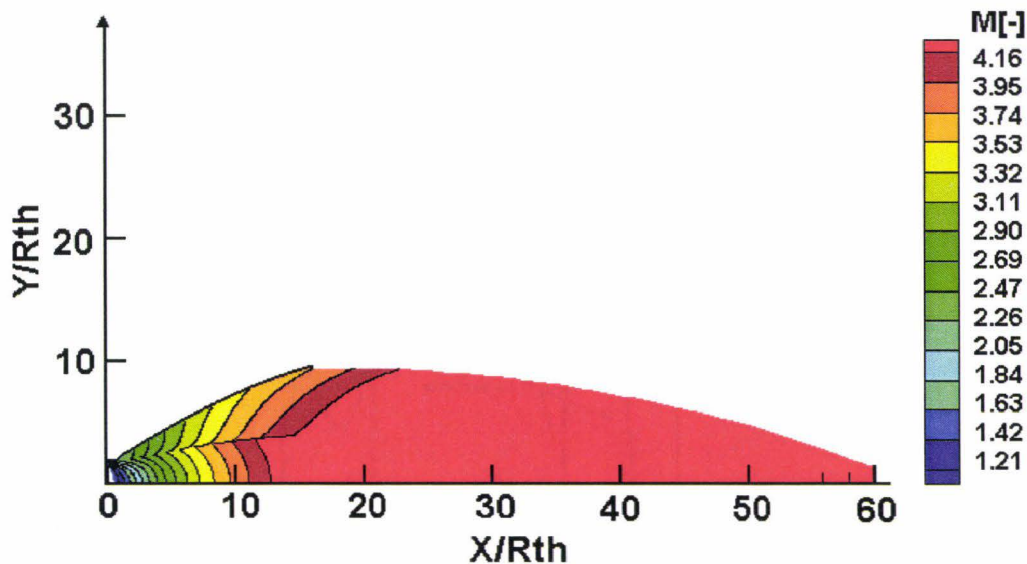


Figure 2.8: Mach number distribution in TOP nozzle

In the past, the use of tandem systems for aerospace engines led to a rather small

altitude range for nozzle use. The parallel system in use for most of the current main stage engines impose a large range of ambient pressure (from 1 bar to almost 0 bar). The nozzle flow has to be slightly over expanded on the ground in order to limit the under-expansion losses at high altitude. This leads to an increasing interest for new nozzle concepts with altitude adaptation properties.

## 2.2.5 Adaptive nozzles

The problems of over expansion and flow separation in conventional nozzles have created the need for new altitude adaptive nozzle concepts. In this section, the solutions, which are currently investigated, are presented.

### 2.2.5.1 Plug nozzles

Many concepts of altitude adaptive nozzles can be found in literature, see for example [29] and [17]. They are classified into two nozzle families: the nozzles which continuously adapt to altitude and two-step nozzles which possess two operating modes. The nozzles of the first family are called plug nozzles. They feature a central body and a free stream shear layer. Two of them are presented below in figure 2.9: an aerospike (a) and (b) and a expansion-deflection (ED) nozzle (c).

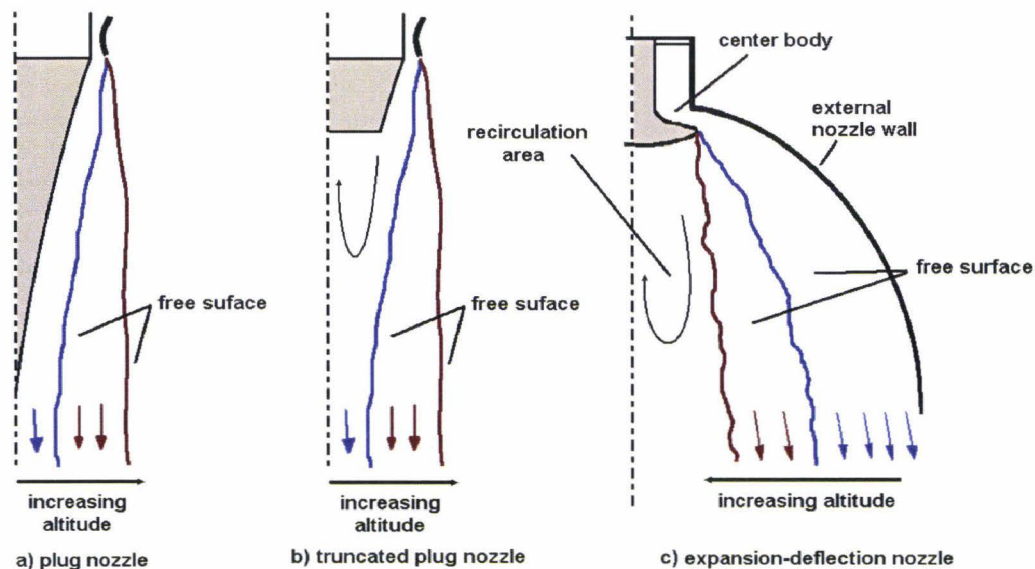


Figure 2.9: Flow in a plug nozzle and an Expansion-Deflection nozzle

The aerospike nozzle features no outer wall. The flow expands along the central body and the free boundary between hot gas and ambient air allows a continuous adaptation of the plume. The optimal contour generates a parallel exhaust flow, without internal shocks, but like in the case of the ideal nozzle, the contour is very long.

In an ED nozzle, the flow first expands around the central body and is then deflected by the outer wall back in the axial direction. The recirculation area in front of the central body provides a free boundary for altitude adaptation. Although plug nozzles permit a good altitude adaptation, they also have a significant limitation: aerospikes are very long and thus heavy; they can be shortened (see fig. 2.9 b)) but are then confronted with a recirculation area in front of the central body, like in ED flow, which generates high instabilities and aspiration losses. A second disadvantage of using plug nozzles for space engines is the necessity to adapt the whole system to the annular nozzle throat. The combustion chamber must figure a very large diameter or must also be annular.

### 2.2.5.2 Dual mode nozzles

The second nozzle adaptive family comprises dual mode nozzles. These offers two operating modes, as they are adapted to two different altitudes by using a moving mechanism or thanks to an appropriate geometry [15]. Some of the most interesting concepts are listed below.

- The dual-throat nozzle presents two coaxial throats. Under low altitude conditions both throats are open. This allows a moderate area ratio. At high altitudes the external throat is closed thus leading to a higher area ratio (see fig. 2.10).

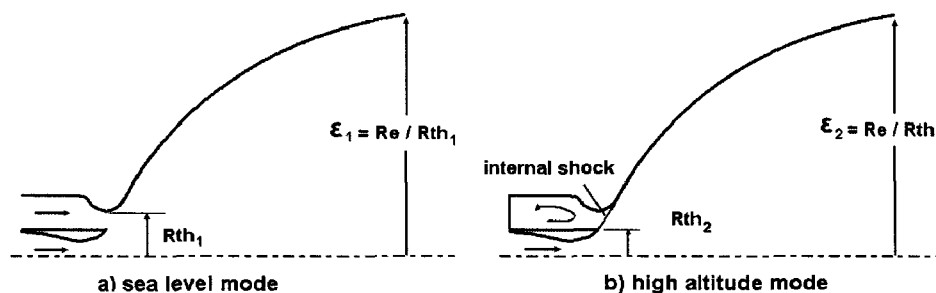


Figure 2.10: Flow in a dual-throat nozzle

- The extendible nozzle (fig. 2.11) is composed of two parts: a small conventional nozzle assures attached flow at sea level and the extension is mounted by a mechanical system at the end of the nozzle to improve performance at high altitude.
- One other possibility for altitude adaptation is the use of a small nozzle placed in a larger one. When a certain altitude is reached a mechanical release system ejects the inner nozzle and the whole external nozzle wall is used.
- The dual bell nozzle forces the flow separation at sea level conditions through its contour inflection. This concept will be described in detail in the next section.

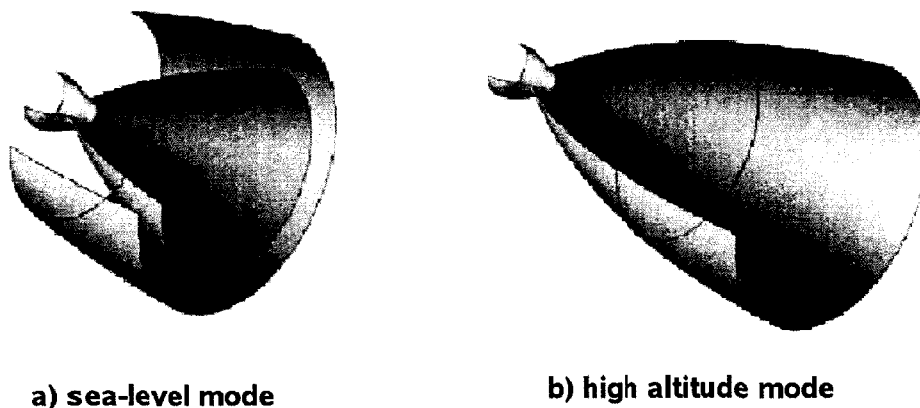


Figure 2.11: Extensible nozzle a) at sea level altitude and b) at high altitude

All the concepts of dual mode nozzles are based on limiting of the area ratio at low altitude to avoid separation and to optimise the sea level performance. At high altitudes the area ratio is then increased to improve the performance in vacuum.

The European Flow Separation Control Device group (FSCD) was initiated to study both flow separation in classical bell nozzles and altitude adapting rocket nozzles such as plug nozzles, dual bell nozzles or nozzles with an extendible exit cone ([60], [14], [45]). As result of their research, the dual bell was identified as the most promising concept. Its characteristics are presented in detail in the next section.

## 2.3 The dual bell nozzle

With its two operating modes, the dual bell nozzle belongs to the two-steps adaptive nozzle family, that is with two distinct operating modes. Its principle is presented in the next sections, as well as its performance and geometric parameters.

### 2.3.1 Principle

A dual bell nozzle consists of a conventional bell nozzle as base nozzle linked with an abrupt change of wall angle to the extension nozzle (as illustrated in figure 2.12).

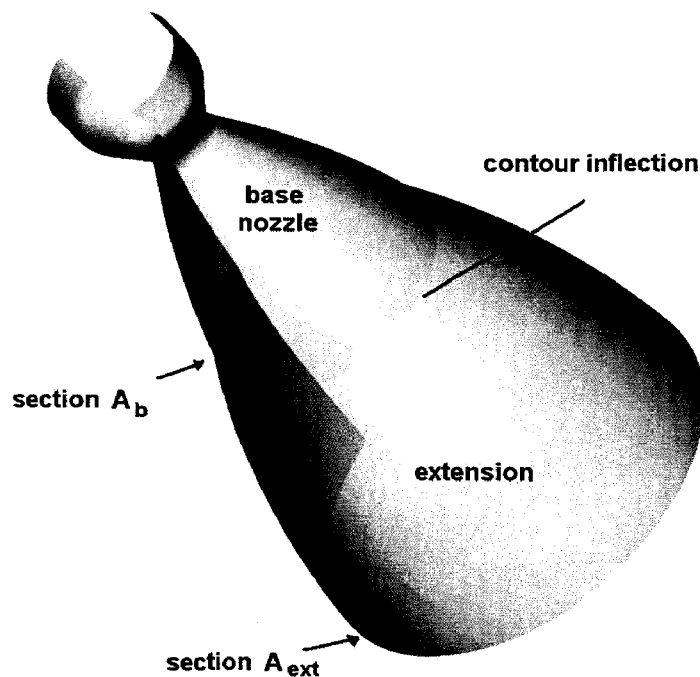


Figure 2.12: Dual bell nozzle

In its sea level mode, the wall inflection forces flow separation at a controlled and symmetrical position: dangerous side loads are avoided and due to a smaller effective area ratio the sea level thrust increases. The dual bell behaves like a small conventional nozzle with an exit section of  $A_b$  (exit section of the base nozzle). During ascent of the launcher, at a certain altitude, the nozzle flow attaches down to the exit section. In this high altitude mode the full expansion area ratio is used resulting in a higher vacuum performance. The behaviour is then comparable to a

bell nozzle with the extension exit section  $A_e$  as exit area.

Figures 2.13 and 2.14 represent the flow in a dual bell during, respectively, sea level and high altitude operating modes. In the following sections, the jump of the flow from sea level mode to high altitude mode is designated as transition and the return to sea level mode as retransition.

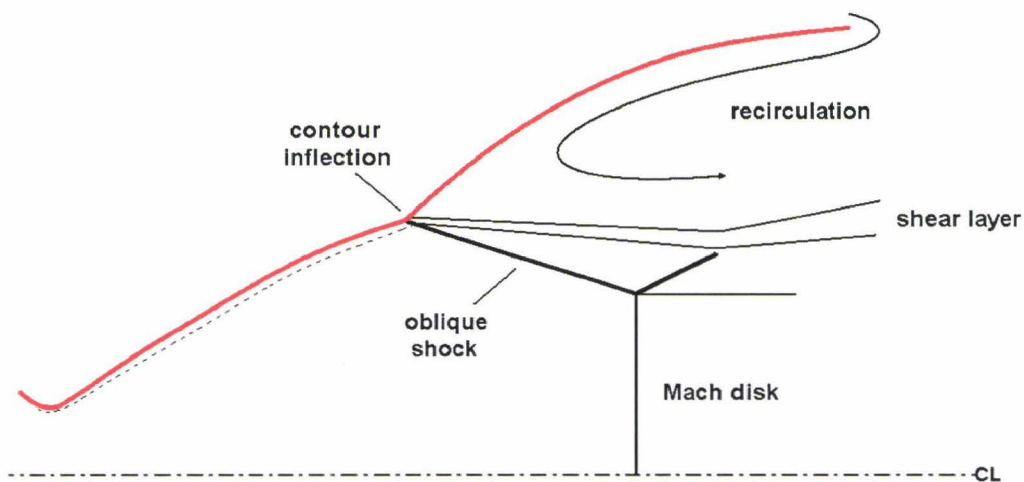


Figure 2.13: Dual bell flow at sea level mode

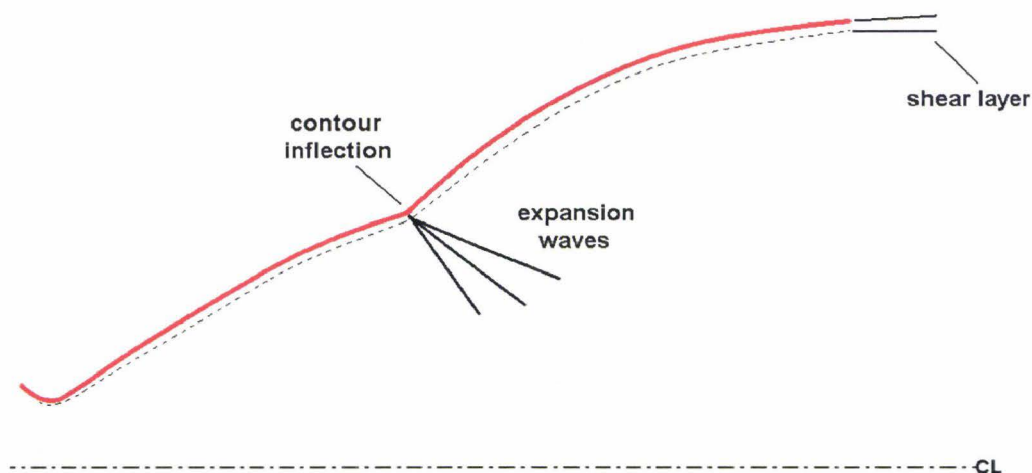


Figure 2.14: Dual bell flow at high altitude mode

With its classical and simple bell design of the base and extension nozzles only a few

changes on existing rocket engines become necessary. Compared to other advanced nozzle concepts, the absence of mechanical parts, which would increase its weight, is one of the outstanding features.

### 2.3.2 Performances

The thrust generated by a dual bell nozzle during sea level operating mode can be written as:

$$F = \dot{m}v_2 + (P_{e,b} - P_a)A_b - \Pi_{sea-level} \quad (2.15)$$

It corresponds to the thrust generated by a conventional nozzle with an exit area of  $A_b$ , the base nozzle exit area. The average exit pressure from the base nozzle is represented by  $P_{e,b}$ . The term  $\Pi_{sea-level}$  indicates the losses due to the aspiration drag induced by the recirculation of ambient air in the separated region of the nozzle extension. It has been evaluated to about 3 % of the sea level thrust ([13] [29]). This term is a function of the extension length and geometry, which determines the shape and length of the recirculation area and thus the pressure and velocity of the recirculating flow.

During the high altitude operating mode, the generated thrust becomes:

$$F = \dot{m}v_2 + (P_{e,ext} - P_a)A_e - \Pi_{high-altitude} \quad (2.16)$$

which corresponds to the thrust generated by a similar conventional nozzle with  $A_e$  as exit ratio. The term  $P_{e,ext}$  represents the average extension exit pressure. The term  $\Pi_{high-altitude}$  designates a term of losses due to the non optimal nozzle contour (compared to a conventional nozzle without any contour inflection). A loss between 0.1% and 1.2 % has been calculated from FESTIP [22].

The specific impulse generated by a dual bell nozzle is depicted in figure 2.15 together with the specific impulse of two conventional nozzles featuring the same area ratios as the base nozzle ( $A_e/A_{th} = 45$ ) and the extension nozzle ( $A_{ext}/A_{th} = 100$ ). The characteristics of the Ariane main engine Vulcain 2 is also presented for comparison purposes.

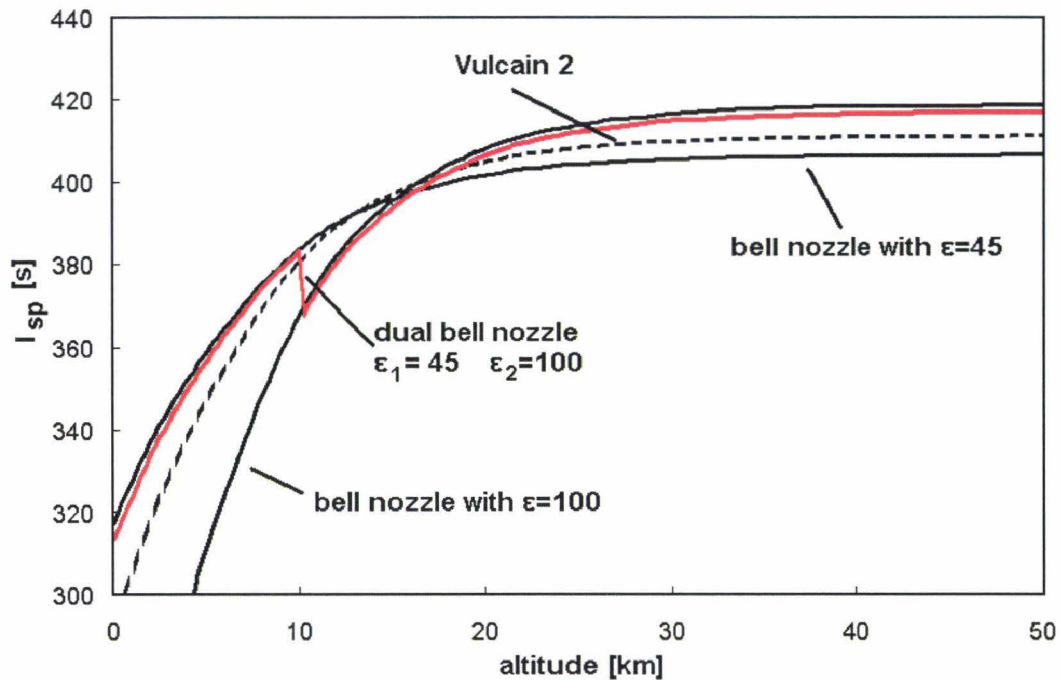


Figure 2.15: Specific impulse as a function of the altitude for two conventional nozzles, the Vulcain 2 and a dual bell nozzle

The performance increase depends on the geometrical parameters of the nozzle and on the flight trajectory of the launcher. All studies have shown potential performances increase, however with very significant variations depending on the nozzle geometry and engine characteristics:

- a payload gain of up to 72 % [13]
- or an effective mass reduction of the vehicle of up to 3 %
- or a potential  $I_{sp}$  gain of up to 10 s [37]
- or a trajectory averaged  $I_{sp}$  increase of up to 1.8% [65]

### 2.3.3 Geometry

The optimisation of the contour geometry for dual bell nozzle is critical to ensure the feasibility of this new nozzle concept. The principle of a dual bell is simple: two

bell nozzles are linked by a wall angle inflection. In order to simplify the study of the flow, this work only deals with dual bells using a TIC as base nozzle. The exhaust flow is almost uniform, without any internal shock wave system which would interfere with the shock system at the inflection, in contrary to TOP nozzle contours, and yields therefore optimal input conditions for the study of the flow downstream of the inflection point.

The contour of the extension must be carefully chosen to avoid any undesired flow separation in the extension before the transition from one operating mode to the other. Therefore, the wall pressure distribution in the extension is decisive. To simplify, only the cases with monotone variation of  $P_w$  are described in detail. Three distribution models are possible: the wall pressure increases along the extension wall, it decreases, or stays constant. These correspond to a positive pressure gradient (PP extension), a negative gradient (NP) or a constant pressure distribution (CP). The wall pressure distribution for these three contour configurations are illustrated in figure 2.16.

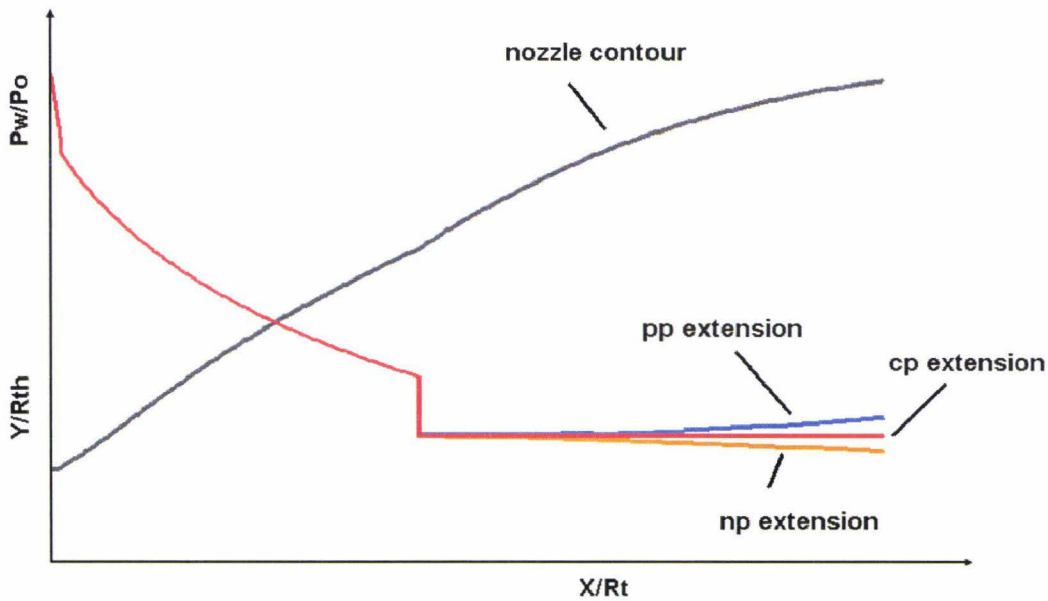


Figure 2.16: Wall pressure distribution in dual bell with CP, PP and NP extension

During ascent of the rocket, the ambient pressure  $P_a$  continuously decreases and the nozzle pressure ratio  $P_0/P_a$  increases. As the separation conditions are reached in the nozzle extension, the transition to high altitude mode starts. The transition conditions are determined by the pressure ratio  $P_{sep}/P_a = f(M)$ . The Mach number  $M$  is only a function of the axial position  $X/R_{th}$  for a given geometry. So that

for each position in the extension corresponds a separation nozzle pressure ratio  $NPR_{sep}$ , which is the product of  $P_0/P_w = constant$  and the ratio  $P_{sep}/P_a$ . That is, when using the Stark separation criterion:

$$NPR_{trans} = \left( \frac{P_0}{P_a} \right)_{trans} = \frac{P_o}{P_w} \cdot \frac{P_{sep}}{P_a} = \frac{P_0}{P_w} \cdot \frac{1}{M} \quad (2.17)$$

In case of a dual bell with a CP extension contour, the wall pressure  $P_w$  and the Mach number  $M$  are the same for every point of the extension wall, i.e. the separation conditions are identical at every point of the extension. When the separation NPR is reached at the first point in the extension, in the vicinity of the inflection, it is also reached for all the points, up to the nozzle extension end. The flow separation point leaves the inflection corner and jumps instantaneously to the end of the nozzle. It attaches abruptly to the whole extension wall; transition is achieved.

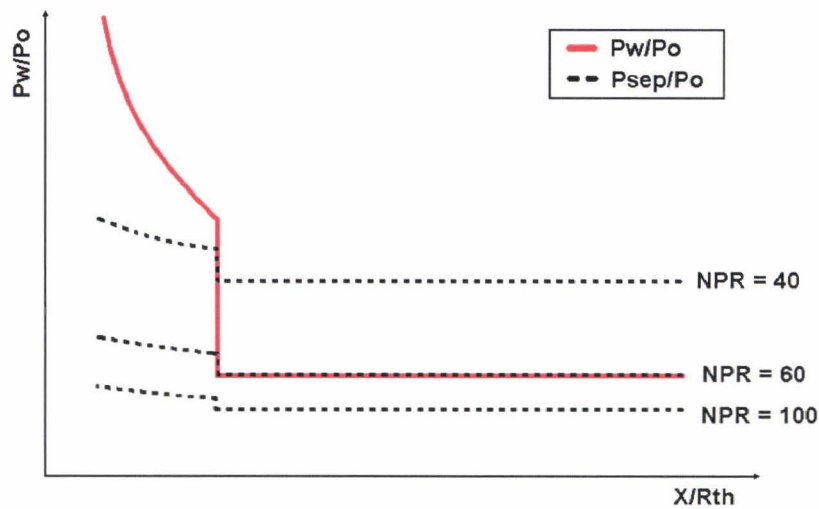


Figure 2.17: Evolution of the separation condition in CP extension

Figure 2.17 illustrates the transition process for a CP extension. The wall pressure distribution is presented together with the separation conditions in the nozzle for various values of the NPR. A wall pressure  $P_w/P_0$  higher than the separation pressure ratio  $P_{sep}/P_0$  indicates an attached flow, a lower value indicates the flow separation at this position. For low values of the NPR (e.g.  $NPR = 40$ ), the curve of separation conditions intersects the curve of wall pressure  $P_w/P_0$  at the inflection position: the flow separates at the contour inflection. When increasing the NPR value, the separation conditions are reached in the whole extension simultaneously

( $\text{NPR} = 60$ ): the flow separation point jumps into high altitude mode. When further increasing the NPR, the flow remains attached to the extension wall.

In a dual bell with NP extension contour, the wall pressure is the highest near the inflection and decreases down to the nozzle end. That is, separation conditions are first reached in the vicinity of the inflection. When further increasing the pressure ratio, the separation point moves downstream in the extension to the nozzle end. To each value of the pressure ratio between the separation NPR in the vicinity of the inflection and the transition NPR corresponds a position of the flow separation point in the extension. Figure 2.18 depicts the steps of the transition in a dual bell with NP extension. When the separation NPR of the first point in the extension is reached, the flow separation point remains at the inflection (e.g.  $\text{NPR} = 40$ ). For NPR value of 60, the flows attaches in the extension up to the position defined as the crossing point of the wall conditions and the separation conditions curves. The transition is achieved only when the separation NPR is reached for every point at the extension wall (in this case, for  $\text{NPR} = 100$ ).

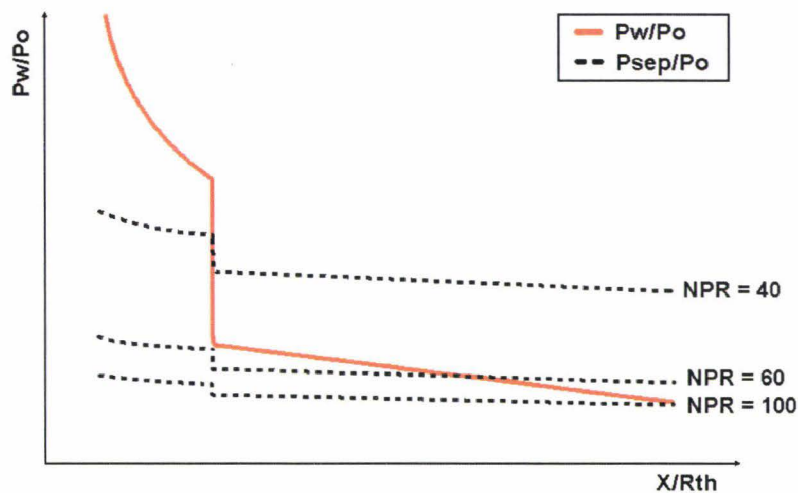


Figure 2.18: Evolution of the separation condition in NP extension

The separation is controlled and symmetric during the sea level mode, but the transition to the high altitude mode is critical for NP extensions and leads to usual flow separation problems of conventional nozzles. High side loads are generated during the duration of the transition. The extension presents then the same drawbacks as a conventional nozzle. A dual bell with a NP extension loses its altitude adaptation characteristics, is therefore of no interest and will not be treated in this study.

A contour with positive pressure gradient (PP) extension yields similar results to those presented for the CP extension: as the separation NPR is reached in the vicinity of the inflection, the conditions are already reached at every point of the nozzle extension (fig. 2.19). The separation NPR in the vicinity of the inflection is lower than the separation NPR at the nozzle end. This configuration is supposed to lead to a better stability against small NPR fluctuations of the flow system than the CP extension configuration and a faster flow transition [13].

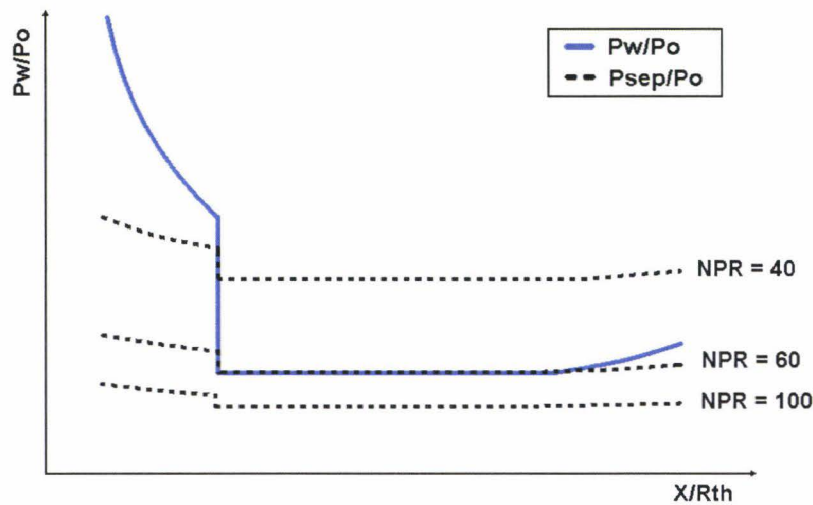


Figure 2.19: Evolution of the separation condition in a PP extension

Although both CP and PP extension are theoretically possible for dual bell nozzles, this work concentrates on the study of CP extension contours. The study of a PP extension would necessitate taking the pressure gradient value into account as a supplementary parameter. All three extension contours have been tested by Horn and Fisher at the Rocketdyne centre and have shown a behaviour corresponding to the analytical study [20].

The geometric parameters for description of a dual bell contour are summarised in figure 2.20. The base nozzle length is designated by  $L_b$ , the extension length by  $L_{ext}$ , the total length by  $L_{tot}$  and the contour inflection angle by  $\alpha$ .

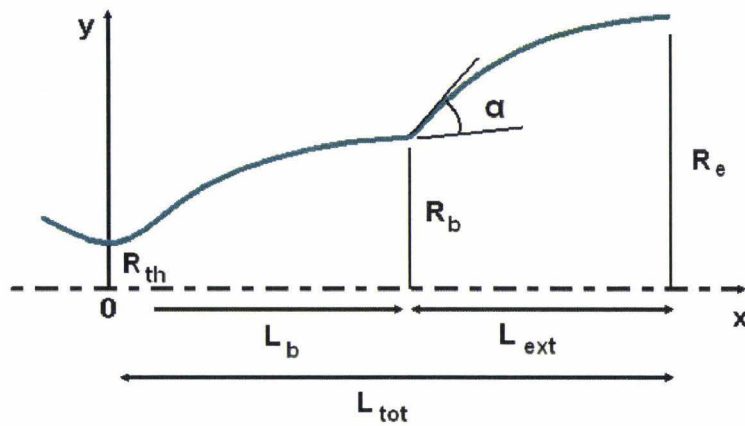


Figure 2.20: Geometric parameters in a dual bell nozzle

In the following sections, the extension length is normalised with the total nozzle length  $L' = L_{ext}/L_{tot}$ . The base nozzle radius and the extension radius are also normalised in the non dimensional characteristic parameters  $\epsilon_b = (R_b/R_{th})^2 = A_b/A_{th}$  and  $\epsilon_e = (R_e/R_{th})^2 = A_e/A_{th}$ .



# Chapter 3

## Experimental flow study

In order to fully understand the flow behaviour in dual bell nozzles, three cold flow sub-scale tests campaigns have been conducted. During the first campaign, three different nozzle geometries were tested and compared. In the second and third campaigns, two of the previous nozzles were shortened to yield information for length optimisation and to allow the observation of the flow in the extension before and during the flow transition. The following chapter summarises the test conditions and subsequently presents experimental results and conclusions drawn.

### 3.1 Test conditions

#### 3.1.1 Test facility

Dual bell cold flow tests have been conducted at the P6.2 test bench at DLR Lampoldshausen. Investigation areas for this test bench are the testing of supersonic nozzles, diffusers and ejectors. For the testing of nozzle models two test rigs are available: the high altitude chamber to work under variable ambient pressure,  $P_a$ , and the horizontal rig to work under sea level conditions. The driving gas is dry nitrogen which presents the advantages of being cheap, easy and safe to use. Besides, in contrary to air, no water condensation appears in dry nitrogen.

The high altitude chamber is an auto-evacuating system. The pressure in the chamber is evacuated by a supersonic nozzle flow, leading to very low pressure conditions. The ambient pressure in the chamber can be decreased to 100 mbar, for a feeding gas pressure varying between 1 and 55 bar (the installations are described in detail in [25] and presented schematically in figure 3.1). This installation presents good characteristics to test dual bell nozzles under various altitude conditions and thus to study the evolution of the flow transition and retransition. However, a series of

tests performed in the past (see [57] and [53]) have shown the incompatibility of the high altitude chamber for dual bell testing, as the abrupt variation of the specific impulse from:

$$I_{sp} = \frac{F}{\dot{m}g_0} = \frac{v_2}{g_0} + \frac{(P_b - P_a)A_b}{\dot{m}g_0} \quad (3.1)$$

in sea level mode to:

$$I_{sp} = \frac{v_2}{g_0} + \frac{(P_{ext} - P_a)A_e}{\dot{m}g_0} \quad (3.2)$$

after the transition cannot be instantly evacuated by the system, leading to a rapid increase of the chamber pressure and hence a decrease of the NPR. This causes the retransition of the flow to sea level mode, followed by a fall in chamber pressure (and increase of NPR), which leads back to transition. This oscillating (flip-flop) effect ends only when the feed pressure increases up to a value that doesn't permit any retransition of the flow. This effect is directly related to the functioning of the high altitude chamber and does not correspond to any real effect that could exist under real flight conditions. This flip-flop effect is described in detail by Stark in [57]. The results obtained in the high altitude chamber are therefore not reliable for the study of dual bell flow behaviour and this installation was not used for this study.

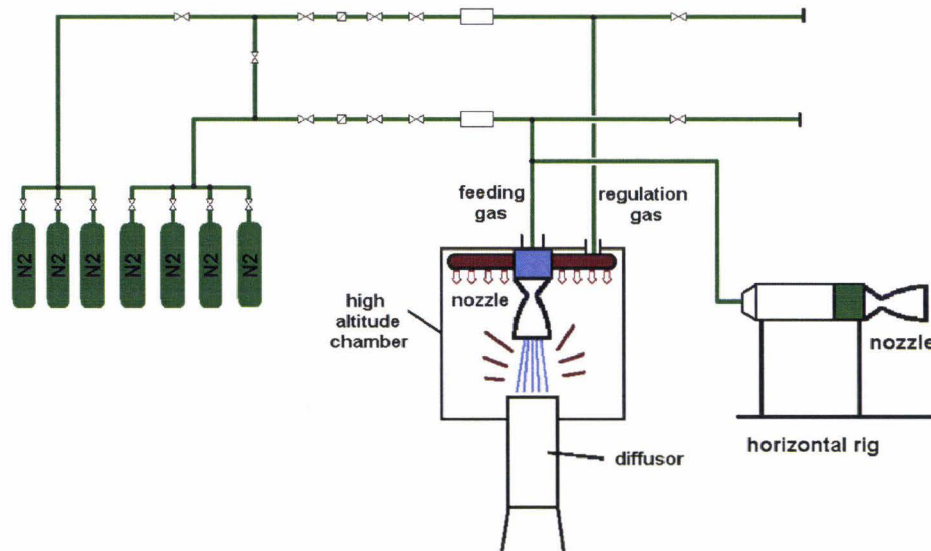


Figure 3.1: Schema of high altitude chamber

The second available installation at the P6.2 facility is the horizontal test rig (photo figure 3.2). The nozzle can be driven with varying feed pressure  $P_0$  under constant ambient pressure  $P_a$ . In this case, the values reached by the NPR are limited to a maximum of 55, which allow investigations to be performed only with dual bell nozzle of small dimensions with a transition NPR smaller than 55. All the tests described in the following sections were conducted on the horizontal rig.

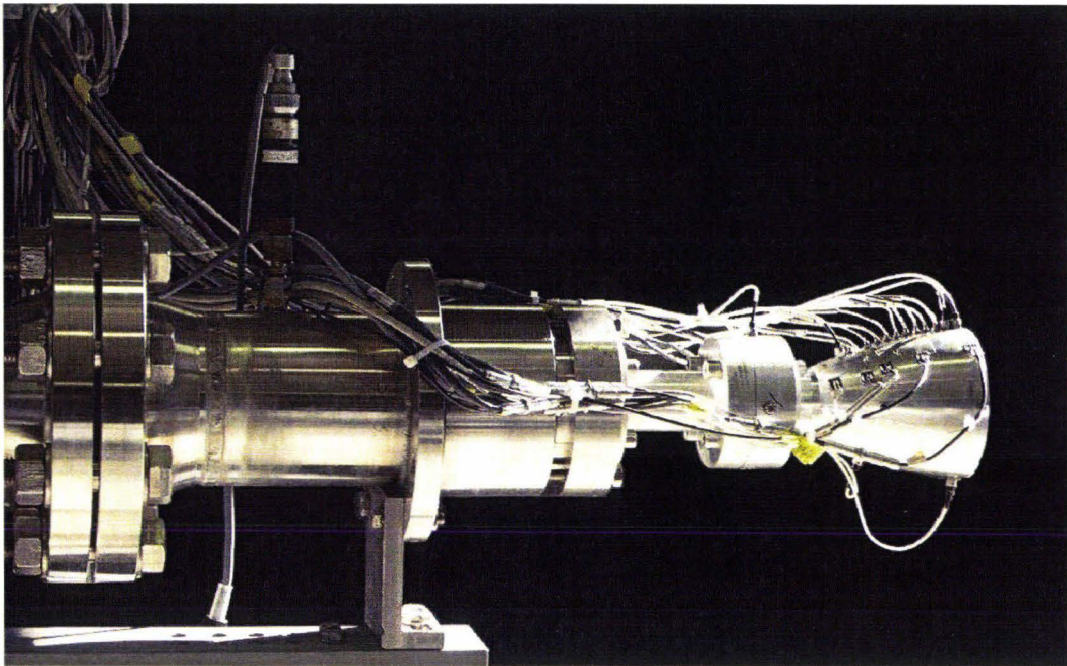


Figure 3.2: Horizontal test rig at the P6.2 test bench

The test installations at the P6.2 bench offer 64 low frequency (1 kHz) measurement channels and 16 high frequency (25 kHz) channels. The signals are then filtered respectively to 160 Hz and 8 kHz. The technical characteristics of the test bench are summarized in table 3.1.

The equipment allows temperature and pressure measurements with these channels, observations of the flow using schlieren optics, thermal imaging and side load measurements. The instrumentation used for dual bell testing are described in section 3.1.3.

Gas	pressure provided mass flow	max. 55 bar up to 4 kg/s
Regulation	pressure provided mass flow	max. 45 bar up to 3 kg/s
High Altitude Chamber	inner diameter inner height pressure in the chamber min. inner pressure	800 mm 1000 mm <100 mbar 8 mbar
Measurements	LF up to 1 kHz HF up to 50 kHz capacity	64 channels 16 channels (with anti-aliasing filters) 50 GB

Table 3.1: Characteristics of the test bench P6.2

All the tests are taped with a surveillance camera placed to image the exit flow from the nozzle. Thus it is possible to detect some undesired effects like condensation of the nitrogen in the nozzle flow or apparition of ice on the cold extension wall during the retransition of the flow from the high altitude mode back to the sea level mode. Indeed, both these effects alter, in a significant way, the wall pressure measurements.

### 3.1.2 Nozzle model

For the comprehension and the optimisation of dual bell nozzle models various parameters have to be considered. The use of the horizontal test rig at P6.2 limits the possibilities for some of these parameters: the throat radius should not exceed 10 mm (maximum mass flow limitation) and the transition must occur at a value of the pressure ratio  $P_0/P_a$  lower than 50 (smaller than the installation maximum pressure ratio). The remaining parameters are the base nozzle and extension lengths, the inflection angle  $\alpha$  and the base and extension area ratios,  $\epsilon_b$  and  $\epsilon_e$ .

For this study, the base nozzle was chosen as a TIC nozzle. A TOP would be closer to the conventional nozzles currently in use in rocket nozzles (Vulcain II, SSME). Hence, contrary to the TOP, the ideal contour generates no internal shock waves which would interfere with the shock system at the inflection during the sea level mode. Furthermore, in the worse case, the flow could even reattach in the extension wall under sea level conditions (as seen for TOP nozzle in [62]).

The present study was realised by testing three dual bell nozzle models presenting different geometric parameters: contours DB1, DB2 and DB3. The base nozzle ge-

ometry is uncritical for this study, so all three nozzle model are designed on the same TIC, using an in-house programme based on the method of the characteristics (MOC). The design parameters for the MOC are the throat radius  $R_{th} = 10 \text{ mm}$  and the design Mach number  $M_d = 5.8$ , for the total conditions:  $T_0 = 293 \text{ K}$  and  $P_0 = 50 \text{ bar}$ , under 1 bar ambient pressure. Contours DB1 and DB2 possess a base length  $L_b/R_{th} = 6.2$  and contour DB3 a base length  $L_b/R_{th} = 5.2$ .

As seen in section 2.3.3, the wall pressure gradient in the extension has to be either positive (PP extension) or null (CP extension). In order to more easily compare and generalise the results obtained, without taking the wall pressure gradient into account, a CP extension has been chosen for those test series. However, tests performed at DLR in similar conditions have already shown comparable results between CP and PP extension (also refer to Stark et al. [57] for results on dual bell nozzle testing with a PP extension).

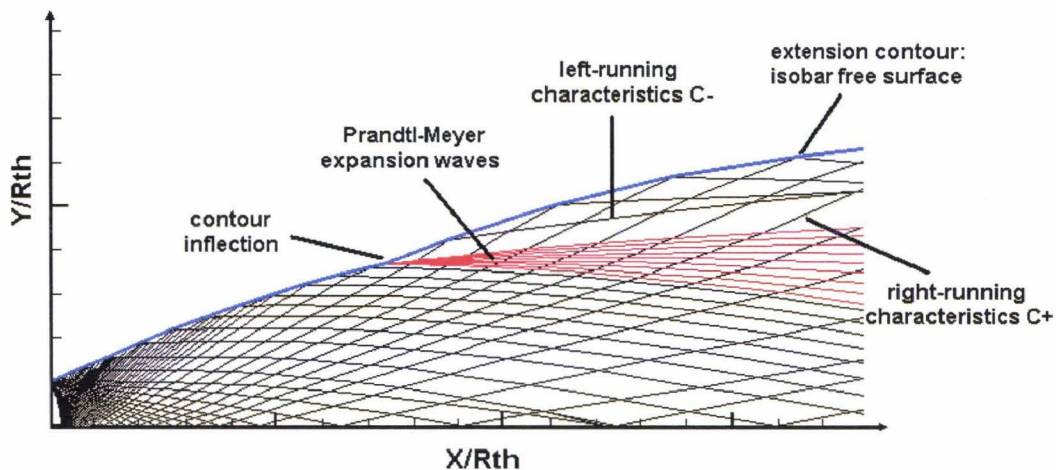


Figure 3.3: Method of characteristics for dual bell design

The method of the characteristics is applied to design the three dual bell nozzle contours. The first module yields an ideal nozzle contour, which can be truncated at the length chosen for the base nozzle. The extension nozzle features a constant pressure (CP) wall profile and is defined with the second programme module. The contour is defined by a free jet isobar leaving the last point of the base nozzle. The isobar can be found by increasing the wall inflection angle inducing a Prandtl-Mayer expansion. As the resulting Mach number and wall pressure cross the chosen separation criterion, the isobar is reached. This procedure assures a flow transition at a given ambient pressure for a given nozzle total pressure, i.e. for a given NPR.

Figure 3.3 schematizes the method of characteristics applied to the design of a dual bell nozzle contour.

The geometric parameters studied here are the base length  $L_b$ , the extension length  $L_{ext}$  and the inflection angle  $\alpha$ . In a first step, only  $\alpha$  and  $L_b$  are investigated; all three contours figure the same value of  $L_{ext}/R_{th} = 8.3$ . Dual bell nozzle contour DB1 possess a base length  $L_b/R_{th} = 6.2$  and an inflection angle  $\alpha_1 = 7.2^\circ$ . Only one parameter is changed at a time to avoid cross influence. Contour DB2 features the same base nozzle length and a smaller inflection angle  $\alpha_2 = 5^\circ$ . The third contour, DB3, figures a shorter base nozzle length:  $L_b/R_{th} = 5.2$  and the same inflection angle as DB1:  $\alpha_3 = 7.2^\circ$ . The geometric parameters of the three tested nozzle contours are summarised in table 3.2 and represented schematically in figure 3.4. All nozzles have a throat radius of  $R_{th} = 10 \text{ mm}$ , they are made of Plexiglas with a wall thickness of 10 mm. Plexiglas has the advantage of being less sensitive to temperature variations than aluminium, usually used for small nozzle testing, because of its low heat conductivity coefficient.

	contour DB1	contour DB2	contour DB3
Throat radius, $R_{th}$	10 mm	10 mm	10 mm
Area ratio, $\epsilon_1$	11.3	11.3	9.4
$\epsilon_2$	27.1	24	25.6
Base length, $L_b/R_{th}$	6.2	6.2	5.2
Extension length, $L_{ext}/R_{th}$	8.3	8.3	8.3
Total nozzle length, $L_{tot}/R_{th}$	14.5	14.5	13.5
Inflection angle, $\alpha$	$7.2^\circ$	$5^\circ$	$7.2^\circ$

Table 3.2: Contour geometry of the three tested nozzles

In the second phase of the experimental analysis (test series B and C described in a next section), the extensions of contours DB2 and DB3 have been successively shortened and tested in the same conditions for each length, in order to observe the flow in the extension before and during the transition and to perform a parametric study of the extension length influence on the flow behaviour.

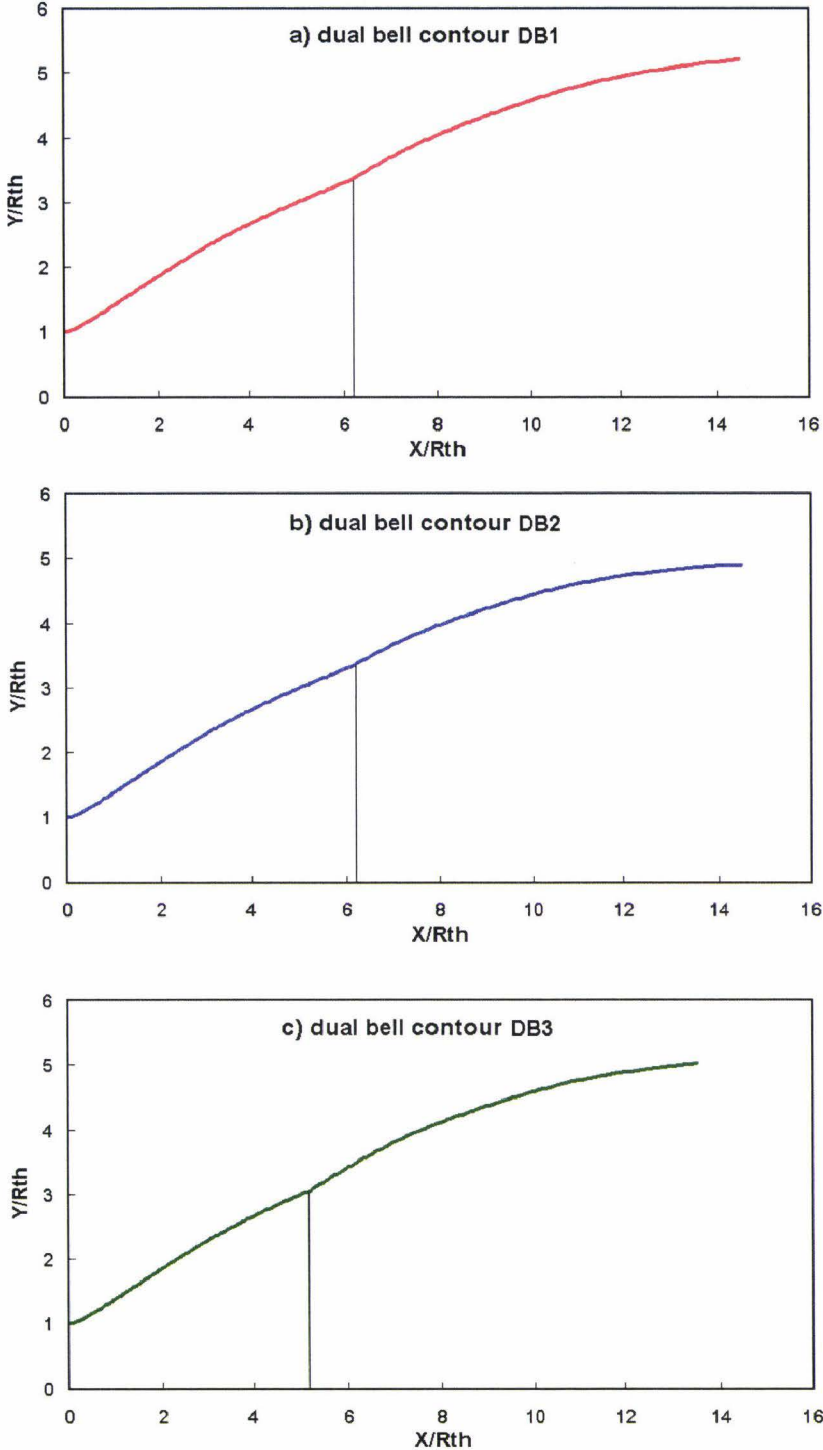


Figure 3.4: Nozzle model contours

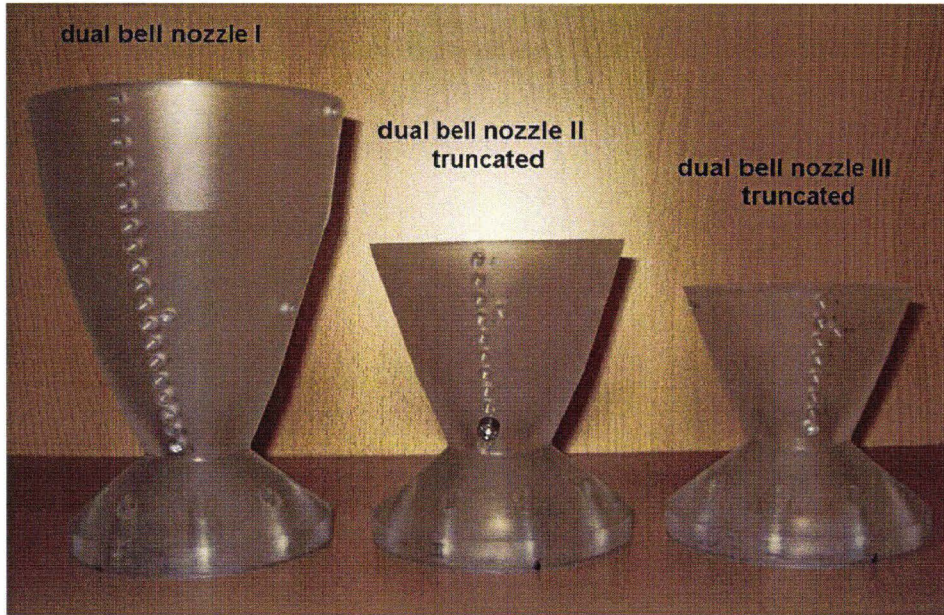


Figure 3.5: Photo of the three tested nozzles

Test configuration	B1	B2	B3	B4	B5	B6
$L_{tot}/R_{th}$	13.5	11.9	10.3	8.9	7.5	6.2
$L' = L_{ext}/L_{tot}$	0.61	0.56	0.49	0.41	0.3	0.16

Table 3.3: Test configurations of dual bell nozzle DB3

Contour DB3 has been shortened in six steps designated as B1 (whole extension length) to B6 (shortest configuration). The relative extension length  $L' = L_{ext}/L_{tot}$  is given for each configuration in table 3.3. Contour DB2 has been shortened in only four steps, designated as C1 to C4 (see table 3.4). Measurements made for DB3 reveal that the results obtained for shorter configuration are not reliable, as presented in the following sections of this work.

Test configuration	C1	C2	C3	C4
$L_{tot}/R_{th}$	14.5	11.9	10.2	8.1
$L' = L_{ext}/L_{tot}$	0.57	0.48	0.39	0.23

Table 3.4: Test configurations of the dual bell nozzle DB2

Figure 3.5 is a photo of the nozzle models tested in this study. Dual bell nozzles DB2 and DB3 feature their shortest configuration, respectively B6 and C4 (see section 3.1.4).

### 3.1.3 Instrumentation

In the following section the measurement systems used for the various tests are described.

#### 3.1.3.1 Wall pressure measurement

In order to study the flow behaviour in the tested nozzles, dynamic wall pressure measurements have been made. The measurement positions are located along a line from the nozzle throat to the extremity. A better resolution in the vicinity of the contour inflection is reached by using further positions in the other quadrants (see fig. 3.6 for the axial repartition, Q1-4 indicates the quadrant of the measurement position:  $0^\circ$ ,  $90^\circ$ ,  $180^\circ$  and  $270^\circ$ ). In addition, the last position in the extension has been measured in each quadrant to detect a potential asymmetry during the transition from one operating mode to the other. The measurement positions are labelled from b1 to b7 in the base nozzle and from 1 to 12 in the extension. They are referred to as  $P_{wb1}$  to  $P_{wb7}$  and  $P_{w1}$  to  $P_{w12}$  respectively in the following sections.

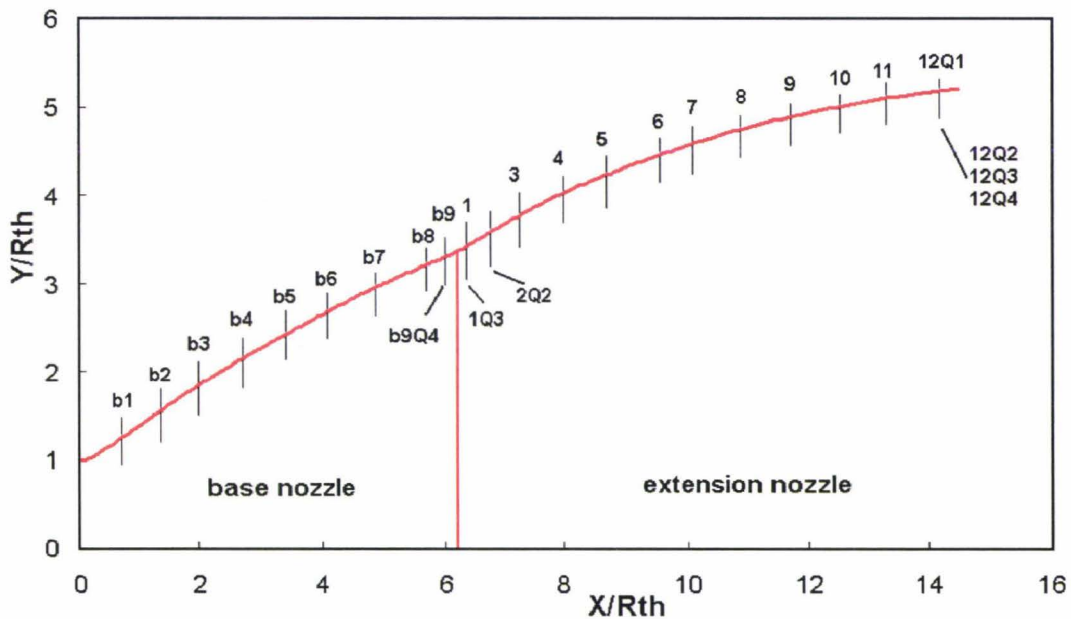


Figure 3.6: Distribution of the wall pressure sensors in the nozzle DB3

The sensors are screwed into the nozzle wall and are in contact with the fluid via 0.5 mm wall orifices. The piezoresistive transducers used are from “Kulite Semi-conductor Inc.”, model XT-154-190M. Positions b1 to b3 are recorded with transducers with an operational pressure range of up to 20 bar. All other positions are recorded using

0 - 1 bar range transducers. The pressure measurement accuracy attained in this operating range is 0.5% and the sensitivity is 0.97 V/MPa. The signals are recorded with a rate of 1 kHz for the LF measurements and 25 kHz for the HF measurements. These are then filtered to 160 Hz and 8 kHz respectively. The natural frequency of the sensors is higher than 150 kHz.

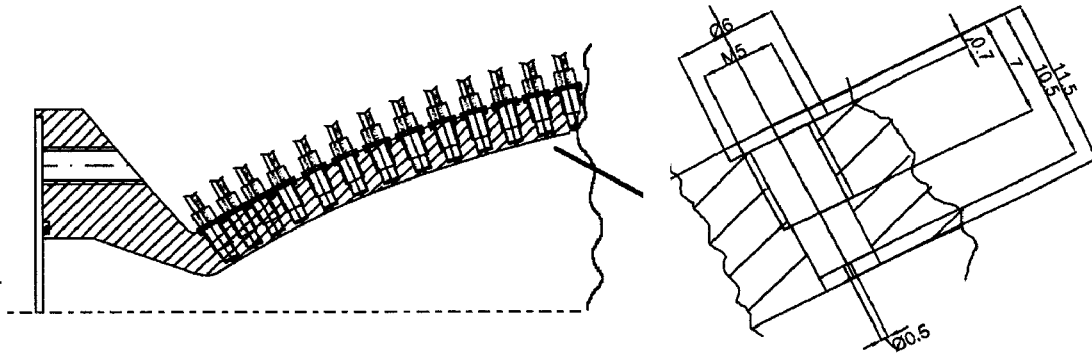


Figure 3.7: Wall pressure measurement

### 3.1.3.2 Optical systems

A schlieren optic installation is used to observe, in detail, the flow evolution during the transition from one mode to the other.

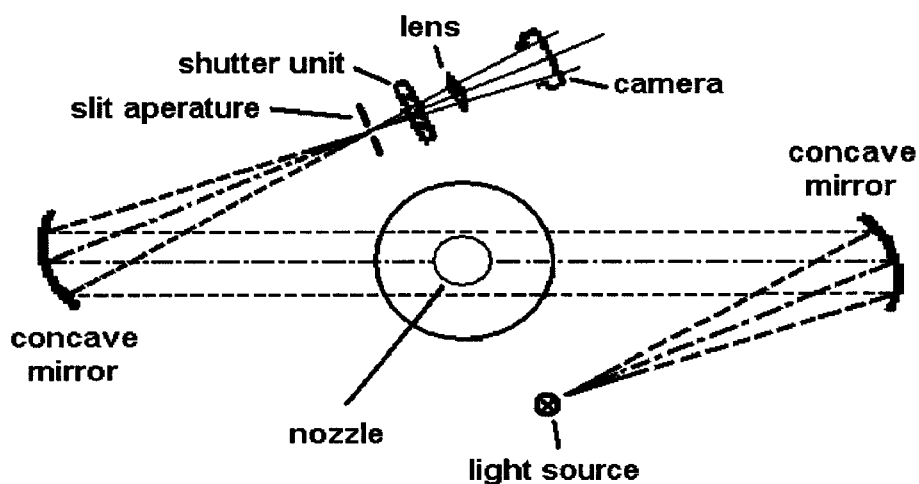


Figure 3.8: Schlieren optic functioning principle

Schema 3.8 illustrates the principle of a schlieren installation: a light source is reflected through the exit flow by two concave mirrors. The variation of density in the flow deviates the light rays. The rays that have not been deviated are filtered using a razor blade, the remaining ones represents the density distribution in the flow. The image can be displayed on a white screen or recorded by a camera placed after a converging lens.

The shock system in the nozzle exhaust flow is recorded during mode transition via black and white schlieren optics. A high speed camera with a maximum frequency of 2 kHz is triggered on the onset of transition by a pressure sensor chosen in the middle of the extension. The camera signal is continuously recorded and a trigger signal corresponding to the pressure drop at a given position in the extension defines the middle of the signal saved (half of the signal recorded before the trigger and half of it after). For series B, a signal of 0.3 s is centered on the instant when the pressure drops in the extension to get the whole transition. For the last two nozzle lengths (configurations B5 and B6), the change of mode is slower, therefore the recording frequency was lowered to 0.5 kHz. The signal recorded is then 6 s centred on the transition. During test series C, all configurations were recorded with the second settings.

### 3.1.3.3 Side loads

The generation of side loads during flow transition is one of the critical issues for the qualification of dual bell nozzles for use in rocket engines. For this reason, side load measurements have been also performed within this work.

To this purpose, a thin-walled bending tube sensitive to lateral forces is placed upstream of the converging part of the nozzle. The thin walls allow bending movements due to vibrations generated by flow instabilities and asymmetries. Tests performed in the past at the test bench P6.2 enabled the optimisation of the measurement system. A rather short bending tube is used for the measurements despite the small momentum generated, such that the signal is associated to a low amplitude. Indeed, the short tube features a higher eigen frequency (about 250 Hz) which is outside of the domain of measurement and can be filtered by the amplifier (at 160 Hz).

Strain gauges are placed on the tube wall with glue and measure the resulting deformation during the tests. Figure 3.9 is a photo of the bending tube used for the tests at the P6.2 test bench. Two pairs of gauges are fixed in each quadrant (vertical and horizontal) and are connected into a full Wheatstone bridge. The signal is directly

proportional to the bending deformation. The other components of the deformation are all compensated by the system.

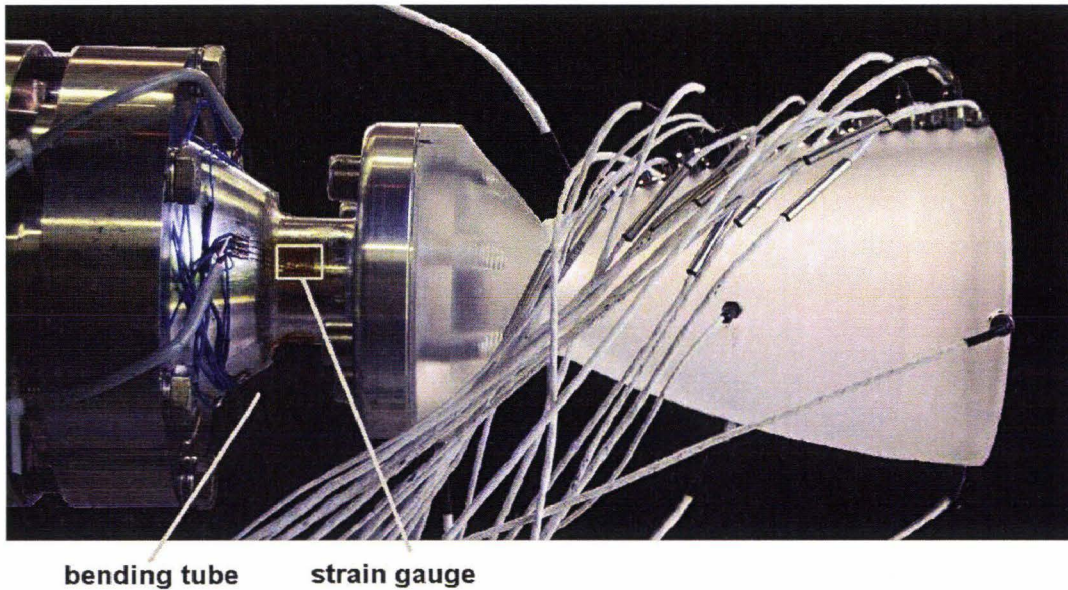


Figure 3.9: Bending tube and dual bell nozzle model

When considering a static problem, the electric signal is directly related to the bending torque. In case of dynamic measurements, the whole system must be taken into account. It can be modelled as a weight mounted on a spring and shows a good agreement for the P6.2 installation. The loads can be calculated with a proper calibration of the system: charges with a well-known mass are suspended at the nozzle and released suddenly (by cutting the suspension). The force generated and its natural oscillation frequency can be related to the electrical signal recorded with an appropriate transfer function (see details in Frey et al. [10]).

However, the side loads measured strongly depends on the installation and the nozzle model (wall thickness, mass, material) and cannot be directly scaled to a real rocket configuration. This can be circumvented by reporting the measured transition loads to an equivalent force acting at the nozzle end.

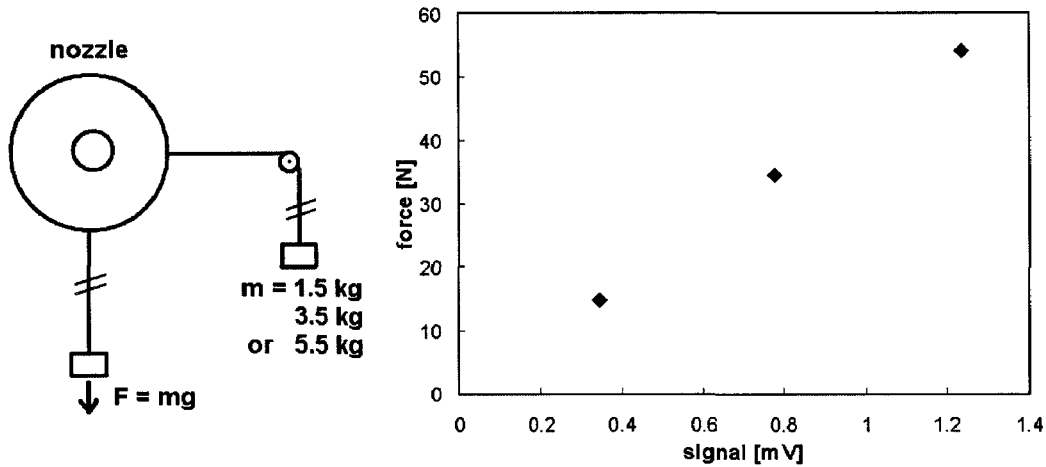


Figure 3.10: Calibration of the side load measurement installation

The calibration process is repeated for three weights and a linear function between the electrical signal and the reference force can be found (see fig. 3.10). The results presented in this work are given in Newtons and correspond to the reference force at the nozzle end in its initial configuration (non truncated).

### 3.1.4 Test configurations

In order to study the transition from the sea level mode to the high altitude mode, and the retransition back to sea level mode, the value of the feeding gas  $P_0$  was regulated up and down with a constant gradient. The value of  $P_a$  is constant during a test, so the variation of the pressure ratio  $P_0/P_a$  is directly proportional to the variation of  $P_0$ . The test bench installations allow gradients of  $P_0$  of up to  $+/- 2.5 \text{ bar/s}$  for values between 1 and 55 bar. The study presented in this thesis can be divided in three test series A, B and C:

- **Series A: parametric study of the influence of  $\alpha$  and  $L_b$  on transition NPR and hysteresis.** All three nozzles contours were tested in similar conditions to perform a parametric study. Test series A1 indicates that the dual bell nozzle DB1 was tested, series A2 was performed on nozzle DB2 and series A3 on nozzle DB3. In order to increase the number of experimental values measured, this test series was composed of two successive transition and retransition, with a constant gradient of  $P_0$  of  $+/- 2 \text{ bar/s}$ . The feed pressure is successively increased and decreased with constant gradient until transition occurs. Figure 3.11 represents the total pressure variation  $P_0$  and

the variation of the wall pressure at position  $P_{w9}$  in the extension (a representative measurement position, far enough from inflection and nozzle lip). The abrupt wall pressure variation indicates transition (presence of the flow at the wall) and retransition (almost ambient pressure measured at the nozzle wall). During series A, only pressure measurements were performed.

In the second part of the investigation, the tests were limited to only one transition and one retransition to shorten the total test duration. When the installation becomes very cold, the nitrogen used as feeding gas may condense inside of the nozzle flow, which leads to higher pressure values at the nozzle wall. The second undesirable effect of longer tests is the occurrence of icing of ambient air humidity at the cold extension wall after the first flow retransition, when the flow separates up to the inflection point. Both effects distort the measurements and are circumvented in the following tests by shortening the test duration. However, between each test of a series, the installation is warmed up using a heat gun and the nozzle wall is dried to avoid icing (condensation of ambient air on the cold wall).

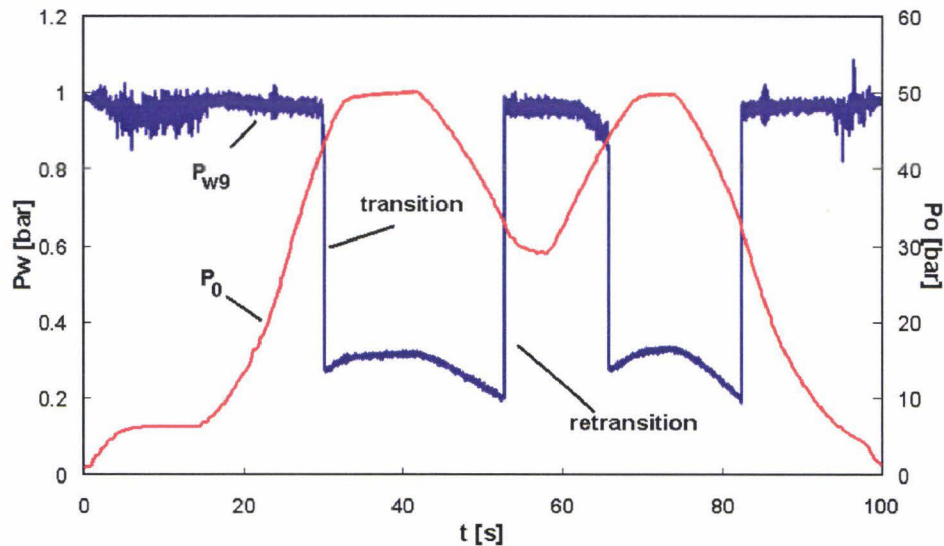


Figure 3.11: Variation of feeding pressure and wall pressure during a typical test process of series A

- **Series B: observation of the flow and study of the influence of  $L'$  on transition NPR, duration and on the hysteresis effect.** Nozzle contour DB3 was successively shortened and each length was tested with the same

conditions (B1 to B6): variations of  $P_0$  with a gradient of  $+/- 2 \text{ bar/s}$ . To each length corresponds a test series name: B1 designates the tests performed on the nozzle with full extension length ( $L_{tot}/R_{th} = 13.5$ ), B2 the tests performed on the nozzle after the first truncation ( $L_{tot}/R_{th} = 11.9$ ), up to B6 for the shortest configuration ( $L_{tot}/R_{th} = 6.2$ ). Schlieren observations and side load measurements have been made for each test in addition to pressure measurements. The objectives of this series were to observe the flow during the transition and to collect information on the extension length's influence on the flow behaviour. Figure 3.12 illustrates a typical process for series B and C: the increase in the total pressure  $P_0$  leads to the pressure jump in the extension (measurement position  $P_{w9}$ ) and its decrease to flow retransition. A first test allows, for each test series, to define a range for the transition NPR. For the subsequent tests, the feed pressure is first increased with the maximum gradient attainable with the installation up to the lower value of the NPR range; it is then increased with the chosen gradient. This allowed shorter test duration, which in addition to having all the advantages of a shorter test duration discussed above also allows the performing of a higher number of tests.

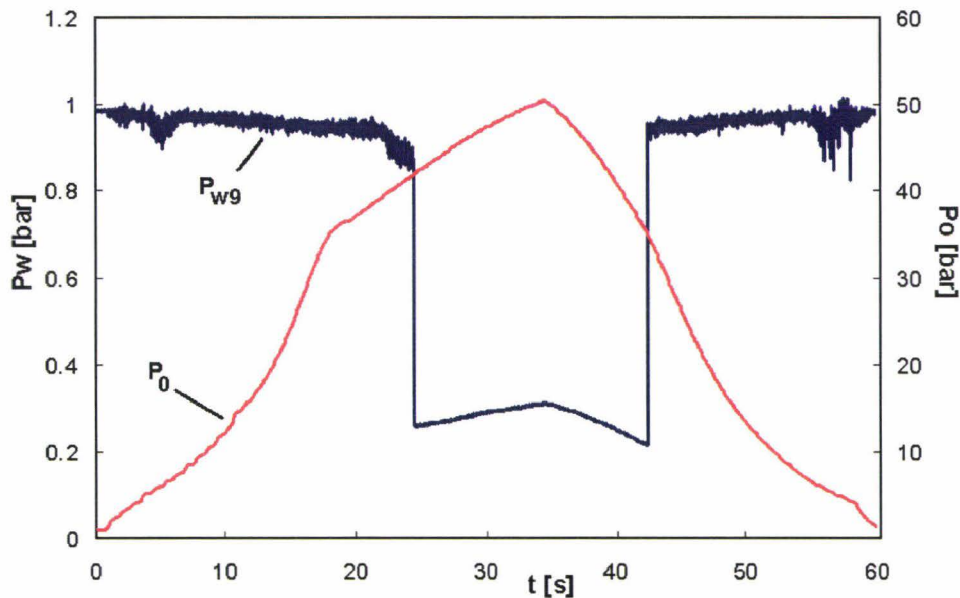


Figure 3.12: Example of variation of feeding pressure and wall pressure during a typical test process of series B and C

- **Series C: study of side load generation and flow transition condition for various NPR variation gradient and extension lengths.** Nozzle

contour DB2 was successively shortened (configurations C1 to C4) and tested for each length under various feeding pressure gradients:  $+/- 2 \text{ bar/s}$ , then  $+1 \text{ bar/s}$  and  $+0.5 \text{ bar/s}$ , in order to study the influence of the pressure variation on the transition behaviour. The retransition duration is less critical than that of the transition because it occurs only as the engine is shut down, with a very high NPR variation gradient. The investigation domain offered by the installation is much lower than the real NPR variation gradient, which is why the decreasing of the feed pressure is chosen to be constant for all tests at  $-2 \text{ bar/s}$ . The test series are designated similar to the B series: C1 corresponds to the test series performed on the dual bell contour DB2 at its full length ( $L_{tot}/R_{th} = 14.5$ ) and C4 corresponds to the shortest configuration ( $L_{tot}/R_{th} = 8.1$ ). The measurements are the same as for series B, but the observation time of the schlieren optics is longer so that the whole transition can be recorded. The aim of this test series is similar to that of series B; the results of schlieren observation were not fully satisfying because of the difficulty to determine the exact transition start.

The various test configurations are summarised in table 3.1.4. The normalised length  $L'$  is the ratio of the extension length  $L_{ext}$  over the actual total nozzle length  $L_{tot}$ . The dual bell nozzle models are designated with their contour name: contour DB1, DB2 and DB3.

Series	Test	Nozzle	$L'$	Instrumentation
Series A	A1	DB1	0.57	- pressure
	A2	DB2	0.57	measurements
	A3	DB3	0.61	
Series B	B1	DB3	0.61	-pressure
	B2	DB3	0.56	measurements
	B3	DB3	0.49	- schlieren optics
	B4	DB3	0.41	- side load
	B5	DB3	0.3	measurements
	B6	DB3	0.16	
Series C	C1	DB2	0.57	- pressure
	C2	DB2	0.48	measurements
	C3	DB2	0.39	- schlieren optics
	C4	DB2	0.23	- side load measurements

Table 3.5: Test configuration for the three dual bell nozzle models

## 3.2 General flow behavior

### 3.2.1 The two operating modes

For each test, the pressure ratio  $P_0/P_a$  is progressively increased and decreased to observe the evolution of the flow in the nozzle model for various values of NPR (in this case directly proportional to the variation of  $P_0$  because  $P_a$  constant). Start up of the nozzle is performed by increasing the feed gas pressure: the flow becomes supersonic. The flow then attaches progressively to the wall and the separation point moves downstream. As the flow reaches the wall inflection, the separation front stops its movement despite a further increase in the total pressure. The flow is then completely attached to the base nozzle wall and separated in the extension: this is the sea level mode.

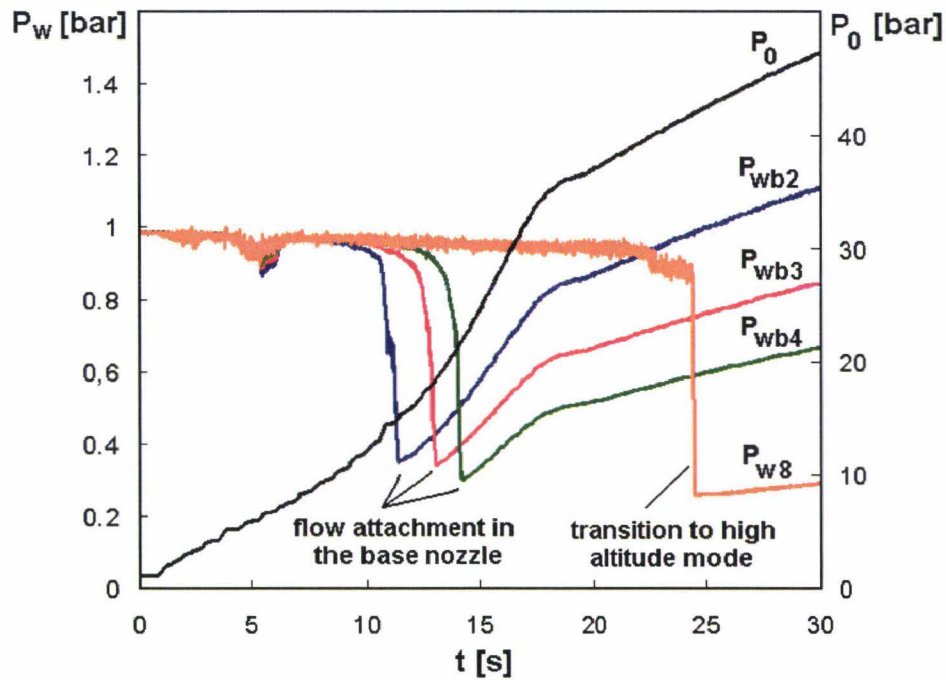


Figure 3.13: Evolution of the wall pressure in the base nozzle and in the extension

When further increasing the pressure ratio value, the flow suddenly jumps into the high altitude mode. The evolution of the wall pressure is represented in figure 3.13 for three positions in the base nozzle ( $P_{wb2}$ ,  $P_{wb3}$  and  $P_{wb4}$ ) and one in the extension ( $P_{w8}$ ). The decrease of the measured pressure at the wall indicates the flow attachment. The pressure at the wall falls from the value of the ambient pressure to the value of the high expanded flow pressure. This effect occurs progressively in the base

nozzle by increasing the NPR, as known for conventional nozzle flow. The pressure variation in the extension is very fast, the value drops instantly upon transition. The separation point moves very quickly in the extension during the transition to the high altitude mode.

Wall pressure measurements along the nozzle wall also yield the axial pressure distribution for various nozzle pressure ratios  $P_0/P_a$ . The values of the wall pressure are presented in figure 3.14 (the wall pressure is normalized by  $P_0$  for easier comparison).

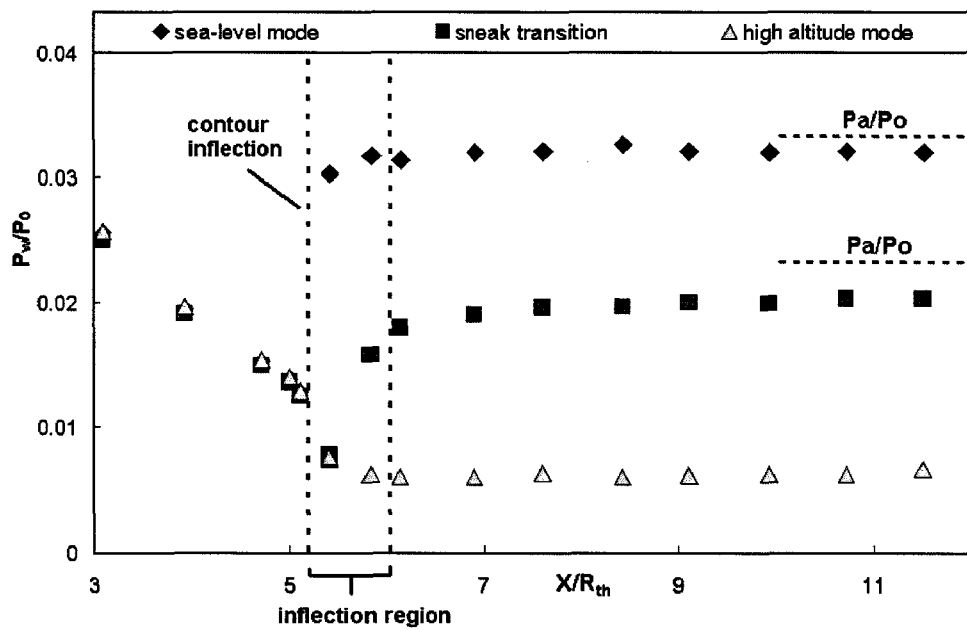


Figure 3.14: Wall pressure distribution for the sea level mode, during sneak transition and at high altitude mode

During the sea level mode, the wall pressure distribution in the base nozzle (for  $x/R_{th} < 6.2$ ) corresponds to the classical distribution in conventional nozzles. In the extension, the flow recirculation is characterised by a higher pressure measured at the nozzle wall, slightly lower than the ambient pressure  $P_a$ . When the high altitude mode is reached, under high NPR values, the pressure measurements in the base nozzle are similar to those made during the sea level mode. The wall pressure in the extension is very low and indicates the presence of a highly expanded flow at the nozzle wall.

By decreasing the pressure  $P_0$ , flow retransition occurs: the flow separation point jumps back to the wall inflection. The operating mode changes from high altitude

to sea level mode. During the tests performed under ambient pressure at the DLR test bench P6.2, an additional effect was observed when decreasing the value of the pressure ratio. The wall pressure in the vicinity of the extension end increases slightly before the retransition conditions are reached. This effect is probably due to the boundary layer thickness near the nozzle lip. This unsymmetrical distribution could lead to increased side loads. However, in flight, the retransition would only take place during the shut down of the nozzle, under vacuum conditions. The very low ambient pressure would not lead to flow separation (the dual bell flow is then underexpanded). This effect can be neglected as a test condition induced effect.

Initial observations indicate the presence of two distinct flow modes. It is also interesting to notice the hysteresis between the transition and retransition NPR values; this effect will be further developed in the next sections.

### 3.2.2 Sneak transition

The tests conducted with a low total pressure variation gradient shown a third state between sea level and high altitude modes. As the pressure ratio  $P_0/P_a$  increases, the pressure at the extension wall first drops at the measurement positions  $P_{w1}$  and  $P_{w2}$ , near the inflection. Due to viscosity effects, the pressure gradient has a finite value at the inflection: the wall pressure gradient is negative in the inflection region (area in the extension, in the vicinity of the inflection).

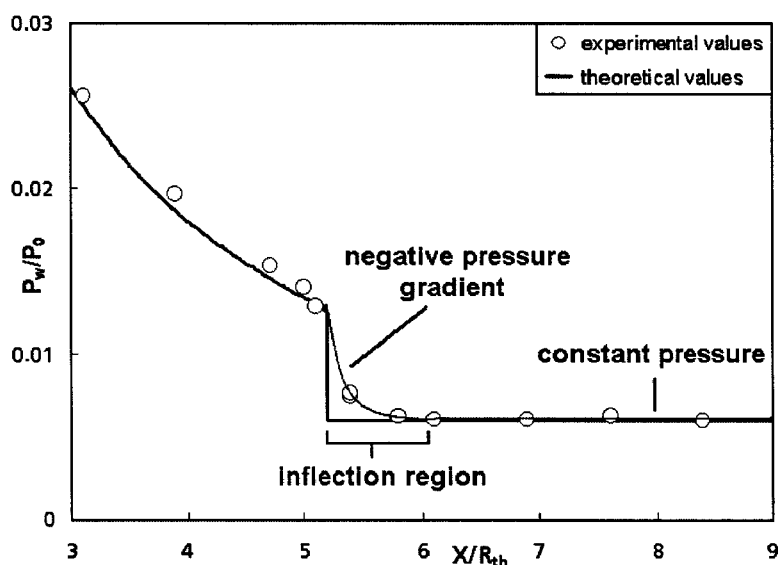


Figure 3.15: Wall pressure distribution in the vicinity of the inflection

Figure 3.15 illustrates the theoretical and experimental wall pressure distributions in the vicinity of the inflection during high altitude mode. This effect was already observed by Martelli et al. [31] [32] [34] in a numerical study.

The extension nozzle can be in fact divided in two parts: the inflection region, e.g. between  $x/R_{th} = 5.2$  and  $x/R_{th} \approx 6$  for the dual bell contour DB3 (see fig. 3.14), where the wall pressure gradient is negative and the residual part of the extension, for  $x/R_{th} > 6$ , where the wall pressure is constant. For a certain interval of the nozzle pressure ratio, the separation can find a stable position in the inflection region. With a further increase of the pressure ratio, the transition NPR is reached. The separation position jumps then to the nozzle end and the transition from the sea level to the high altitude mode takes place as the residual nozzle part displays a constant wall pressure profile. This flow evolution preceding the actual transition is further on addressed as "sneak transition".

Figure 3.16 represents the evolution of the wall pressure measured at the extension wall at position  $P_{w1}$  (in the inflection region) and at a position in the constant pressure region (sensor position  $P_{w5}$ ). The first pressure jump corresponds to the flow attachment in the inflection region: the sneak transition and the second one corresponds to the actual flow transition in the complete nozzle.

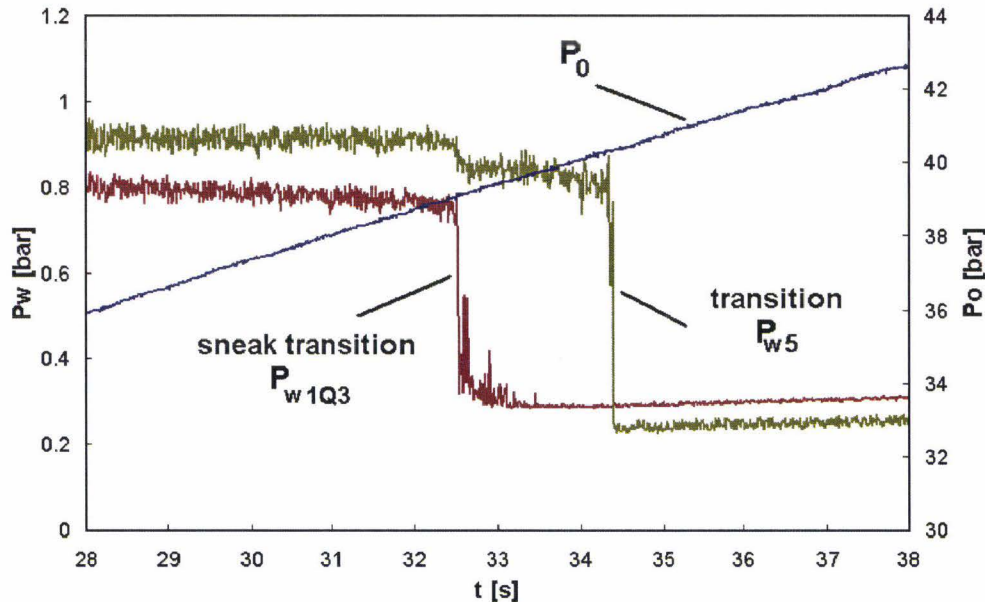


Figure 3.16: Pressure evolution in the inflection region and in the extension during sneak transition and transition

Tests performed with a low variation gradient of the ratio  $P_0/P_a$  have shown a good repeatability of this effect. Pressure measurements made during test series B, for various values of the extension length of the nozzle model DB3, are presented in figure 3.17. The NPR value is reported for the sneak transition: when the flow first moves in the inflection region (measurement position  $P_{w1}$ ) and for the transition: when the flow jumps to the end of the nozzle (measurement position  $P_{w5}$ ). The transition NPR is a function of the geometry and increases by shortening the nozzle extension. The sneak transition features a constant value of the NPR: the phenomenon is independent of transition.

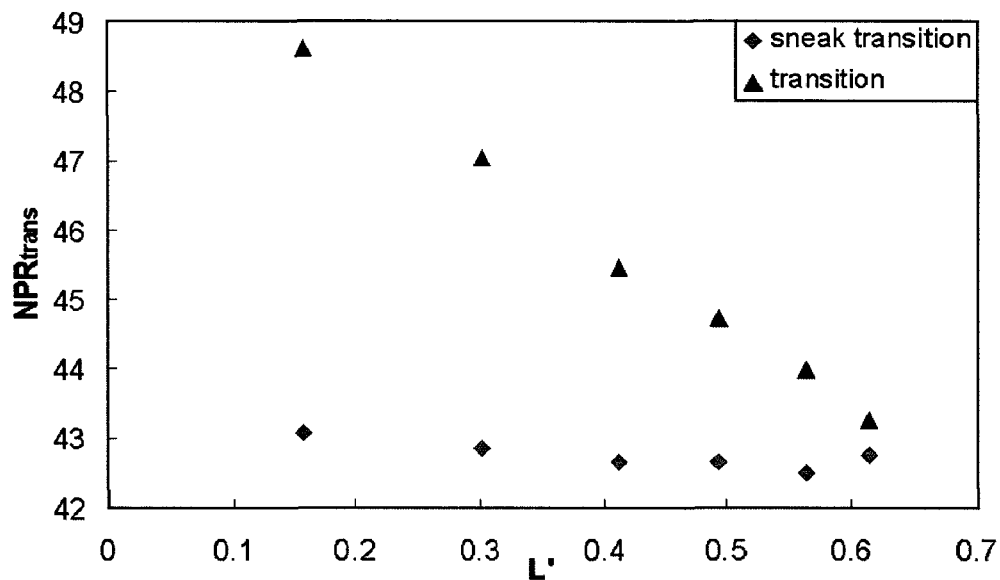


Figure 3.17: Values of the NPR at the sneak transition and at the transition

In the real case, the total pressure stays constant during flight. The variation of the pressure ratio  $P_0/P_a$  is only due to the variation of the ambient pressure due to the change in altitude. This variation is very slow, such that the sneak transition will be a critical effect for rocket nozzle main engine applications.

In the following sections, the transition nozzle pressure ratio  $NPR_{trans}$  always refers to the transition from the inflection region up to the end of the nozzle.

### 3.2.3 Flow model during transition

Schlieren pictures have been recorded during test campaigns B and C for various settings in order to observe the flow evolution in dual bell nozzles. During test campaign B, the pictures were recorded with a high resolution and a high frame rate (2000 frames per second). The hardware limitation of 2000 images for each sequence led to short recording times. After the sneak transition was identified, the aim of test campaign C was to obtain the flow evolution between sea level mode and the beginning of the transition. Therefore, the rate was decreased to 500 frames per second, even 125 fps for some configurations. The signal was triggered on the pressure measurement at the extension wall. All the results presented in the following section were obtained for dual bell contour DB2 during test campaign C.

Figure 3.18 is a series of schlieren photographs taken during the transition for configuration C2 ( $L_{tot}/R_{th} = 11.9$ ). The camera was set at 500 frames per second. It is possible to observe the evolution of the transition by observing the shock system generated by the wall separation.

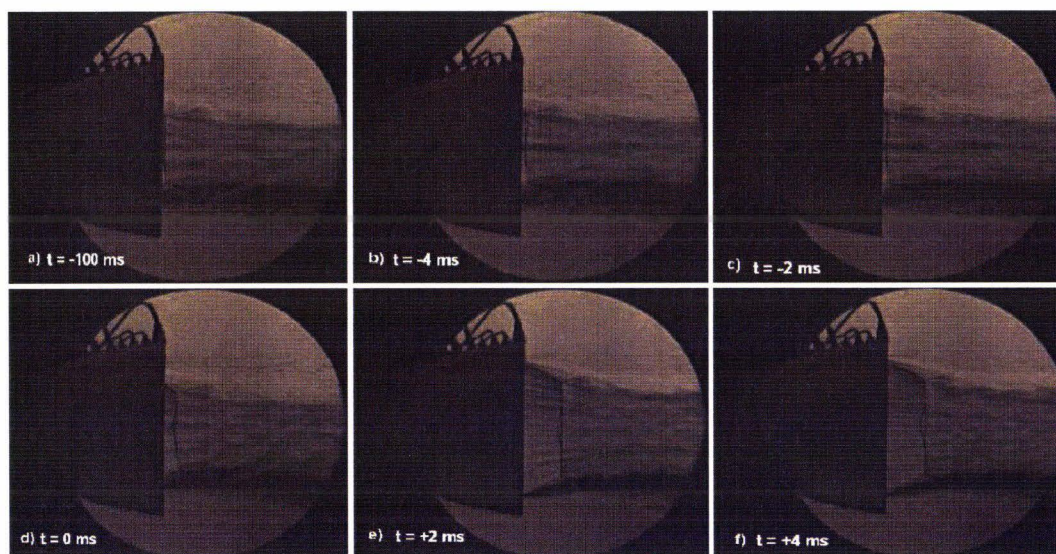


Figure 3.18: Schlieren pictures of the flow before and during the transition

- image a): the shock system is inside the nozzle extension. The Mach disk is visible in the vicinity of the nozzle end section. The flow separation point is located at the contour inflection: sea level mode. (picture taken 100 ms before transition start, following pictures taken with an interval of 2 ms)

- images b) and c): the flow separation point sneaks slowly into the inflection region. The Mach disk moves forward out of the nozzle extension. Sneak transition takes place.
- image d): the point of lowest wall pressure is reached. It marks the end of the sneak transition and the begin of the transition.
- image e): the separation point moves quickly along the nozzle extension wall
- image f): the flow attaches to the wall in a large part of the extension. The transition front slows down to the extension end. No picture has been made of the high altitude mode (transition end reached) because of the limited signal duration.

The schlieren pictures are then superimposed with the nozzle contour grid in the corresponding configuration and the position of the shock system and Mach disk are measured (as seen fig. 3.19). Using the coordinates of the points plotted, it is possible to extrapolate the flow separation point as the intersection of the contour and the oblique shock. The angle  $\beta$  between the jet and the nozzle axis is also calculated.

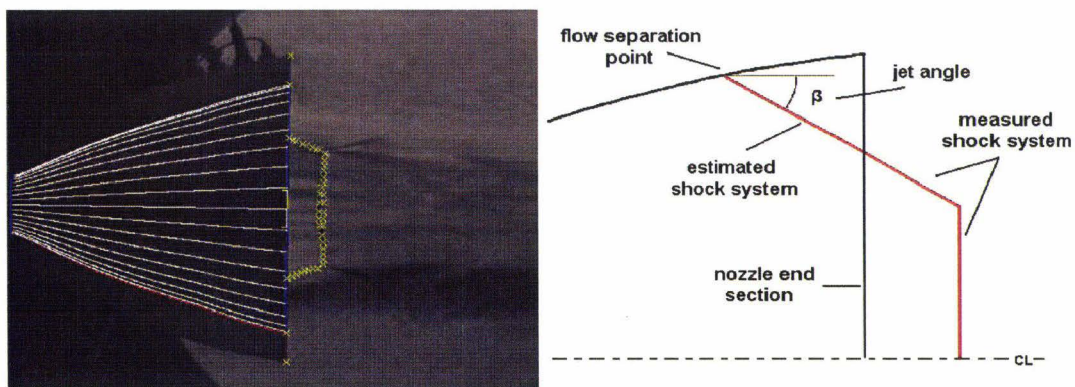


Figure 3.19: Measured points on the shock system

The most significant measurements are those made with the shortest nozzle configuration (configuration C4,  $L_{tot}/R_{th} = 8.1$ ). However, as seen in the previous section, the nozzle extension length influences the flow transition (variation of the transition NPR). The flow behaviour for the configuration C4 has to be compared to the other

configurations to verify that the nozzle contour truncation has no disturbing influence on the global flow behaviour. Therefore, the jet angle  $\beta$  has been calculated and related to the wall flow separation position in the extension for the various configurations (fig. 3.20). The values are taken only during the sneak transition or the beginning of the transition for significant flow configurations. As the transition starts, significant asymmetries may appear, inducing high variations in the calculated jet angle. For the longest configurations, the Mach disk and the shock system are hard to discern, which is why some points positions are only represented for the upper or the lower part of the flow in graph 3.20.

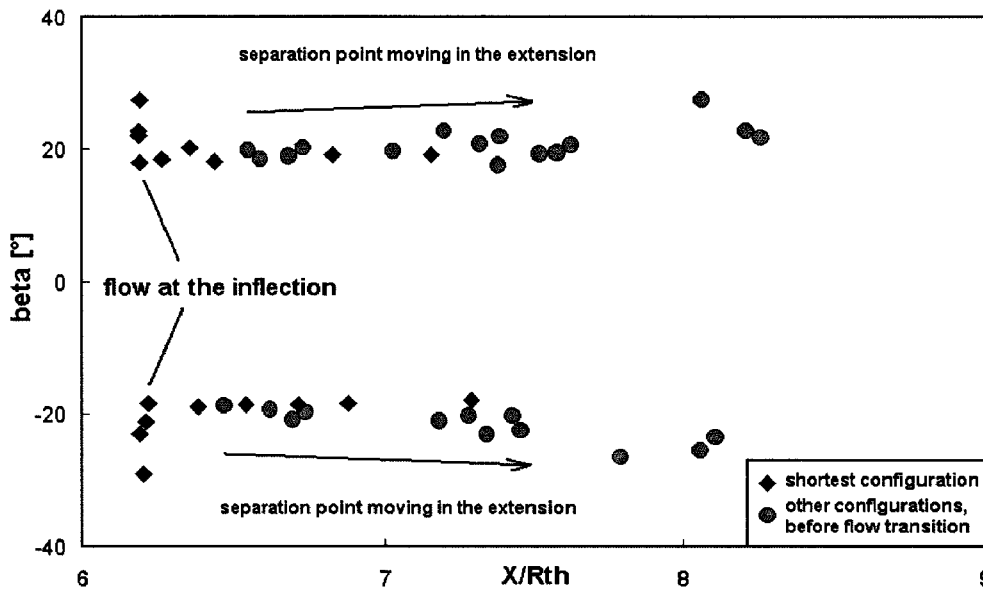


Figure 3.20: Flow jet angle over the separation point position for the various nozzle DB2 configurations

The various nozzle configurations show a good accordance with the shortest configuration. Under sea level mode, when the flow separation is located at the contour inflection, the jet angle varies from about  $30^\circ$  to  $18^\circ$ . After the start of the sneak transition,  $\beta$  varies almost linearly with the separation position in the extension. Thus the flow behaviour observed for the shortest nozzle can be assumed to be representative for that in a full length nozzle.

The evolution of the shock system at different times before and during the transition is shown in figure 3.21 for configuration C4. Two steps can be discerned during the flow evolution:

- First step: sea level mode is reached. The flow separation point is located exactly at the inflection. When the NPR increases, the jet opens (angle  $\beta$  decreases). The flow accelerates around the inflection point.
- Second step: the flow has reached transition conditions in the inflection region and the separation points starts moving into the extension. Sneak transition takes place.

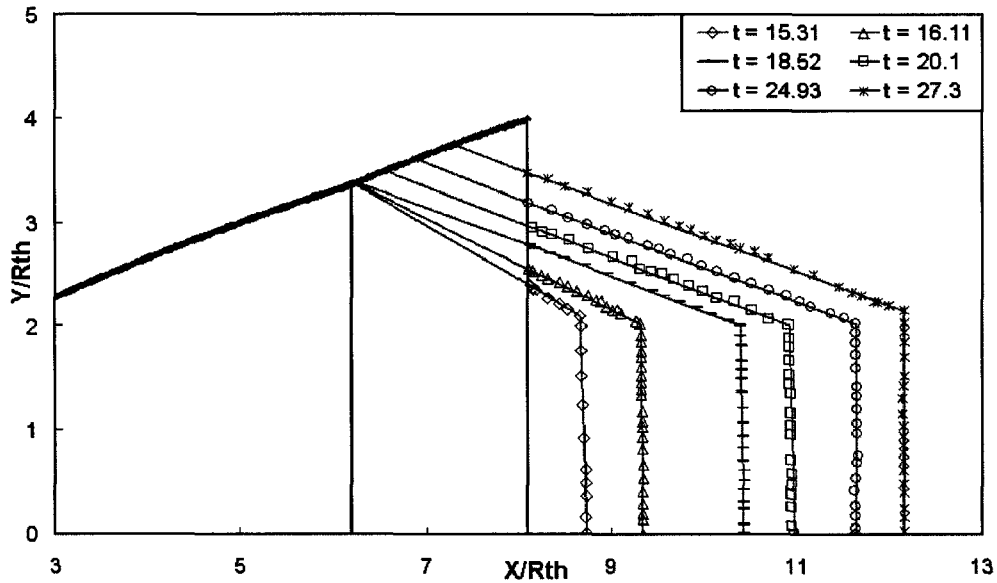


Figure 3.21: Evolution of the shock system in the vicinity of the contour inflection at sea level mode and during the transition to high altitude mode

A critical point for the dual bell concept validation is the generation of side loads during the change from one mode to the next. The asymmetric movement of the flow separation point in the extension may lead to significant structural loads. During sneak transition, the separation point stays in the short inflection region, so that no significant side load peak is expected. The region of constant pressure offers a wide range of positions for the separation point (as supposed by Hagemann et al. in [13]). Nozzle configuration C4 yields information on sneak transition and on transition, but the nozzle is too short to lead to a fast flow transition as recorded for the other nozzle configurations. In order to observe the flow behaviour during the actual transition, configuration C2 ( $L_{tot}/R_{th} = 11.9$ ) was chosen.

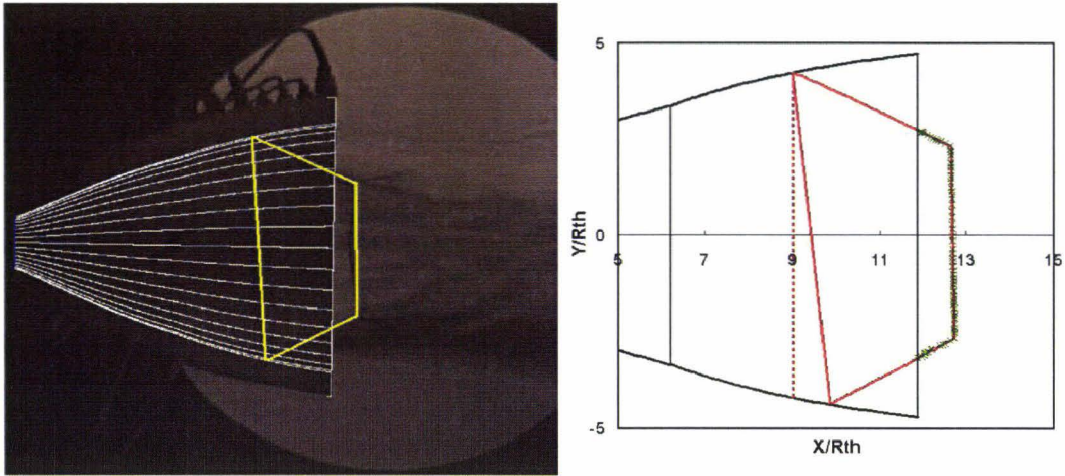


Figure 3.22: Tilted separation plane during flow transition

Figure 3.22 represents a picture taken during the flow transition and its corresponding shock system measurement. The location of the separation point shows a significant asymmetry, with an order of magnitude of  $\Delta x/R_{th} \approx 1$ . A small asymmetry of the Mach disk leads to a significant asymmetry of the separation point position at the extension wall. The duration of this effect is very short ( $t \leq 1ms$ ) but may lead to high peaks in side loads, as shown in section 3.4.

### 3.3 Geometrical study

#### 3.3.1 The different parameters of influence

For each test performed during the three test series, wall pressure measurements were made along the nozzle. The transition and retransition are defined as the instant when the pressure jumps abruptly at the measurement positions along the extension wall. With every change of mode, the value of the ratio  $P_0/P_a$  was recorded and averaged for each nozzle configuration in  $NPR_{trans}$  and  $NPR_{retrans}$ . Figure 3.23 summarises the transition conditions for all the measured configurations as a function of the relative extension length  $L'$ . Nozzle configuration DB1 appears in one configuration, nozzle DB2 is depicted in three length configurations (test series C1 to C3) and nozzle DB3 appears in five configurations (tests series B1 to B5). The results for series B and C do not include the last configuration (B6 and C4); indeed, in their shortest configuration, the nozzles present no clearly defined transition.

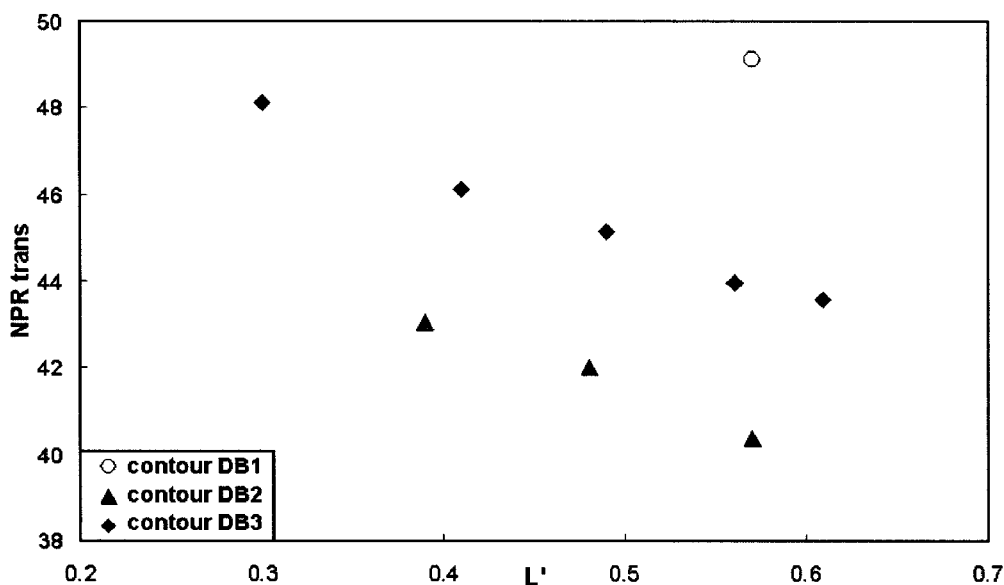


Figure 3.23: NPR at the transition for the various nozzle geometries

The results show a very good repeatability with a statistical error of less than 1% on the calculated average values.

### 3.3.1.1 Influence of extension geometry on transition

Test series B and C (on nozzle models DB3 and DB2) yield information on the influence of the extension length on the transition conditions (see figure 3.23). For both cases, the relationship between the  $NPR_{trans}$  and  $L'$  seems to be linear. The transition takes place at a higher value of the NPR in a dual bell nozzle using a shorter extension contour.

The pressure values have been recorded along the nozzle wall for each length configuration B1 to B5 of nozzle DB3. During the sea level mode, the pressure measured at the nozzle extension wall corresponds to the pressure of the recirculating ambient flow. The velocity of this flow,  $v_{recirc}$ , depends on the geometry of the recirculation area (see figure 3.24) that is located between separated flow and extension flow. The velocity increases with decreasing inflection angle  $\alpha$  and jet angle  $\beta$ ; it decreases with decreasing extension length.

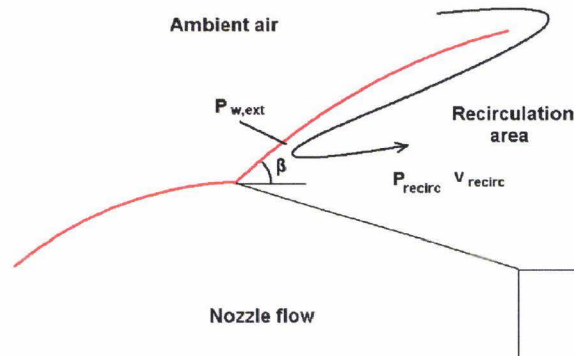


Figure 3.24: Geometry of the recirculation area in the extension nozzle for the sea level mode

The local ambient pressure is then a function of the relative extension length  $L'$ . For the length configurations B1 to B5 of nozzle DB3, the pressure of the recirculating flow  $P_{w,ext}$  is taken at each measurement position in the extension for the instant preceding the transition (local pressure drop). Under sea level mode, the value of  $P_{w,ext}$  corresponds to the pressure of the recirculating flow measured at the extension wall. The ratio of  $P_0$  through  $P_{w,ext}$  is depicted in figure 3.25 for each position at the instant previous to the local pressure drop. This value is the actual pressure ratio seen by the flow at transition: total pressure divided by the local ambient pressure.

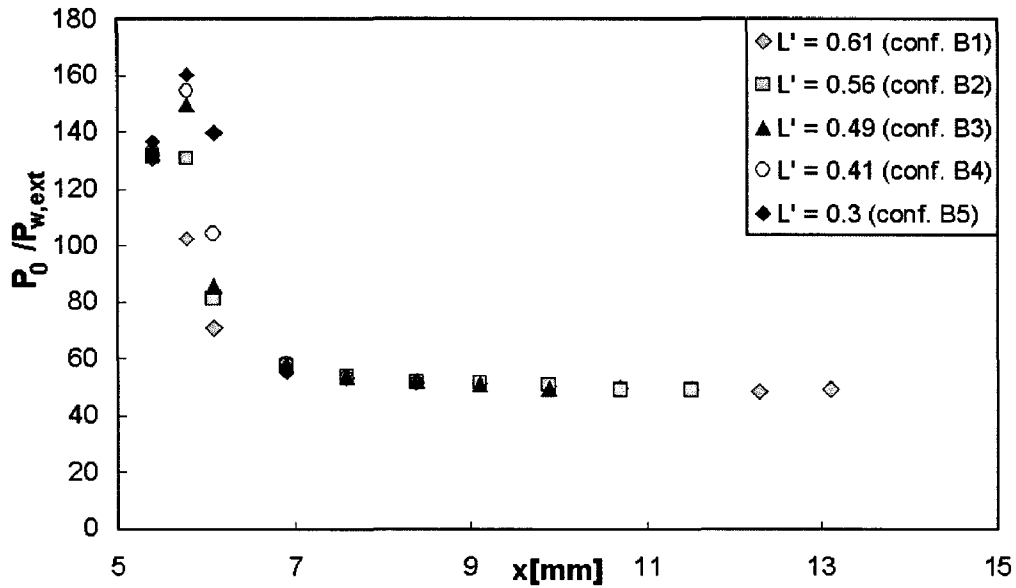


Figure 3.25: NPR at the pressure jump in each measurement point

The pressure ratio values show a very good accordance for the different configurations in the constant pressure region of the extension. The dependency between the extension length and the transition NPR is actually a dependency between the extension length and the local ambient pressure in the extension. As the nozzle extension becomes shorter, the recirculation zone in the extension at sea level mode becomes shorter and smaller. The thus resulting higher pressure inside the separated extension causes a slower recirculating flow. With decreasing  $L'$  the pressure inside the separated extension increases, but as the pressure ratio needed for transition of the flow remains constant, the total pressure needed to change mode also must increase.

In the inflection region, the pressure ratio values measured present significant variations as a function of the geometry. The differences noticed for the various configurations may arise from the difficulty to measure the exact pressure jump which is not as abrupt as during the actual transition.

### 3.3.1.2 Influence of the inflection angle

Contours DB1 and DB2 feature the same base nozzle geometry, but different values of the contour inflection angle. The comparison of the transition properties of these nozzles contours yields information on the influence of  $\alpha$  on dual bell flow behaviour.

The angle of the wall inflection  $\alpha$  determines the expansion of the flow when changing from the sea level to the high altitude mode. Base nozzle geometry defines the values of wall pressure ratio  $P_b/P_0$  and the Mach number of the flow  $M_b$ . To each value of  $\alpha$  corresponds a Mach number in the extension  $M_e$  and a wall pressure ratio  $P_e/P_0$ , as illustrated in figure 3.26.

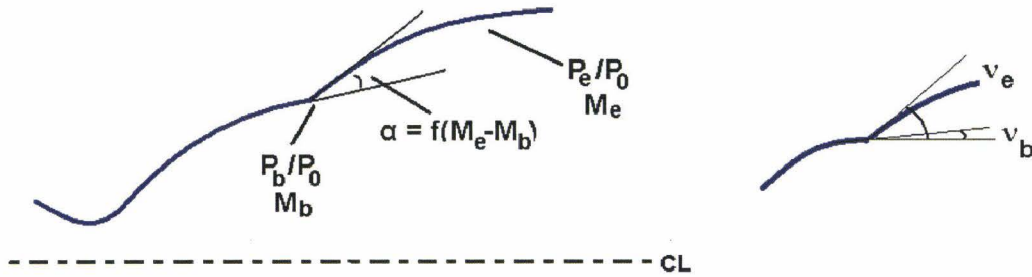


Figure 3.26: Parameters of the inflection angle

The inflection angle  $\alpha$  is related to the flow conditions with the relation:

$$\alpha = \nu_e - \nu_b \quad (3.3)$$

Where the angle  $\nu_b$  can be calculated using the Prandtl-Meyer relation as a function of  $M_b$ , the Mach number reached by the flow at the base nozzle end and  $\nu_e$  as a function of  $M_e$ , the Mach number reached by the flow in the extension during high altitude operation (which is constant in the whole extension for a CP contour). The Prandtl-Meyer relation is given for the general case as:

$$\nu = \sqrt{\frac{\gamma+1}{\gamma-1}} \arctan \sqrt{\frac{\gamma-1}{\gamma+1} (M^2 - 1)} - \arctan \sqrt{M^2 - 1} \quad (3.4)$$

For a given value of  $\alpha$  and a given base nozzle geometry, there exists a unique value of the Mach number  $M_e$  in the extension. The value of  $M_e$  is represented in figure 3.27 as a function of  $\alpha$ , for various values of the base Mach number  $M_b$ .

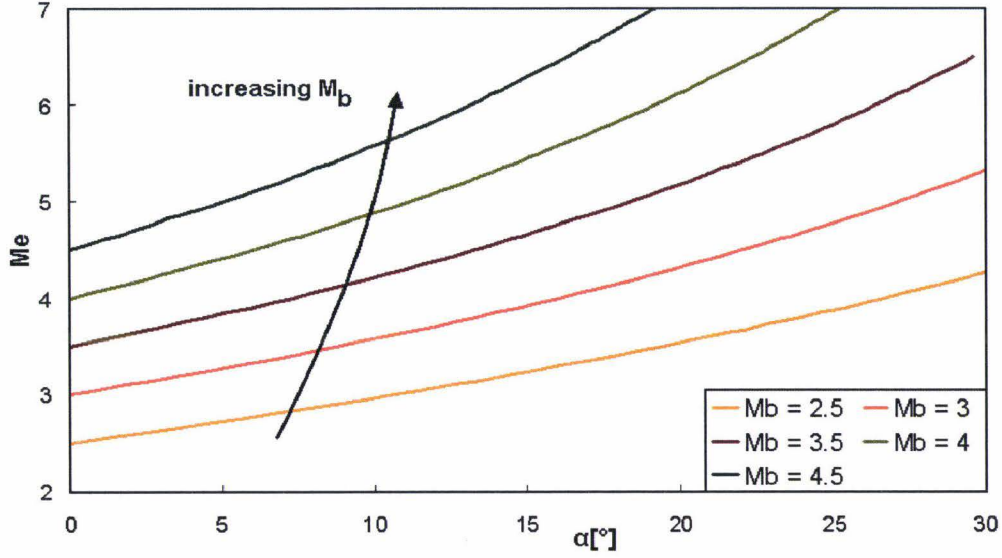


Figure 3.27: Mach number in the extension as a function of the inflection angle

The remaining thermodynamical properties can be calculated in the extension using the isentropic relations. The ratio of the wall pressure at the extension  $P_e$  to total pressure  $P_0$  can be obtained using the following relation:

$$\frac{P_0}{P_e} = \left(1 + \frac{\gamma - 1}{2} M_e^2\right)^{\frac{\gamma}{\gamma - 1}} \quad (3.5)$$

The theoretical value of the transition nozzle pressure ratio ( $NPR_{trans}$ ) is determined using one of the separation criteria presented in section 2.2.3. The Stark criterion was applied to calculate the theoretical NPR values shown in fig. 3.28.

$$NPR_{trans} = P_0/P_{a,trans} = \frac{P_0}{P_e} \frac{P_{e,sep}}{P_a} = \frac{P_0}{P_e} \frac{1}{M_e} = \frac{1}{M_e} \left(1 + \frac{\gamma - 1}{2} M_e^2\right)^{\frac{\gamma}{\gamma - 1}} \quad (3.6)$$

The corresponding values of the transition NPR are calculated for the two base nozzle geometries: contours DB1 and DB2 with the length  $L_b/R_{th} = 6.2$  and contour DB3 with  $L_b/R_{th} = 5.2$  (which defines  $M_b$ ). Contours DB1 and DB3 feature the same value of the inflection angle  $\alpha_1 = 7.2^\circ$  and contour DB2 features a value of  $\alpha_2 = 5^\circ$  (which defines  $M_e$ ). Both theoretical and experimental values are depicted in fig. 3.28. Experimental values measured and averaged from test series A show a very good agreement with the theoretical calculated values.

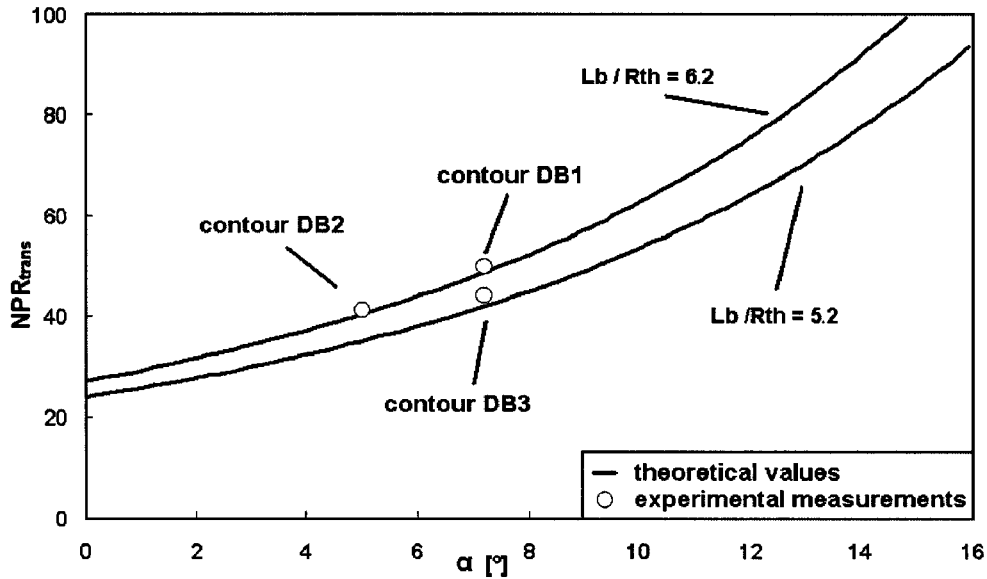


Figure 3.28: Theoretical and experimental values of transition NPR as a function of the inflection angle

The choice of the inflection angle determines the flow expansion between sea level and high altitude mode, and imposes the flow transition conditions: the higher  $\alpha$  is, the higher the altitude at which the dual bell will change mode.

### 3.3.1.3 Influence of the base nozzle length

The dual bell base nozzle is chosen in order to optimise sea level performance. Nozzle extension geometry has little influence on the performance, with about 3% thrust losses during sea level mode operation due to aspiration drag (Manski et al. [29]): the ambient air is aspirated by the high velocity exhaust flow and the recirculation area in the extension leads to thrust losses. The base geometry is also a parameter of influence for the transition conditions.

Contour DB1 and DB3 possess the same inflection angle ( $\alpha_1 = \alpha_3$ ) and a similar relative extension length ( $L'_1 = 0.57$  for contour DB1 and  $L'_3 = 0.56$  for contour DB3 in configuration B2). Only the base nozzle lengths are different:  $L_{base}/R_{th} = 5.2$  for dual bell contour DB3 and  $L_{base}/R_{th} = 6.2$  for contour DB1. Figure 3.29 displays the theoretical transition NPR value as a function of the base length and the experimental values measured for the three model contours. The theoretical values are calculated with the same method as presented in the previous section.

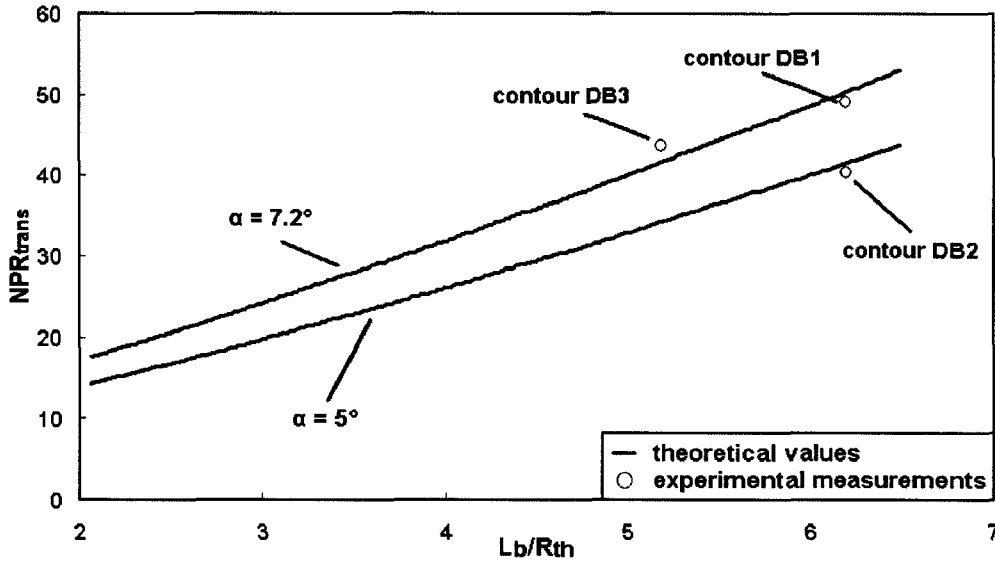


Figure 3.29: Transition NPR as a function of base length  $L_b$

The calculated transition NPR is in good accordance with the measurements performed in this work. A shorter base nozzle leads to a flow transition from sea level to high altitude mode for a lower value of the NPR, which corresponds to a lower altitude. The inflection angle has a more significant influence on the transition NPR than the base nozzle length.

#### 3.3.1.4 Influence parameters on retransition

The same operation has been made for the retransition characteristics. The  $NPR_{retrans}$  is depicted in figure 3.30 for the various configurations as a function of the relative length  $L'$ . As already presented for the transition, nozzle configuration DB1 appears in one configuration (A1), nozzle DB2 in three configurations (test series C1 to C3) and nozzle DB3 in five configurations (test series B1 to B6). The short configurations B6 and C4 do not lead to a clear retransition.

The variations of the various geometric parameters show similar trends to those found by studying the transition conditions: influence of the relative extension length and the inflection angle on  $NPR_{retrans}$ . The difference between transition and retransition NPR indicates an hysteresis effect in the dual bell mode change. This hysteresis effect, that should ensure the flow stability in each mode, is presented in detail in the next section.

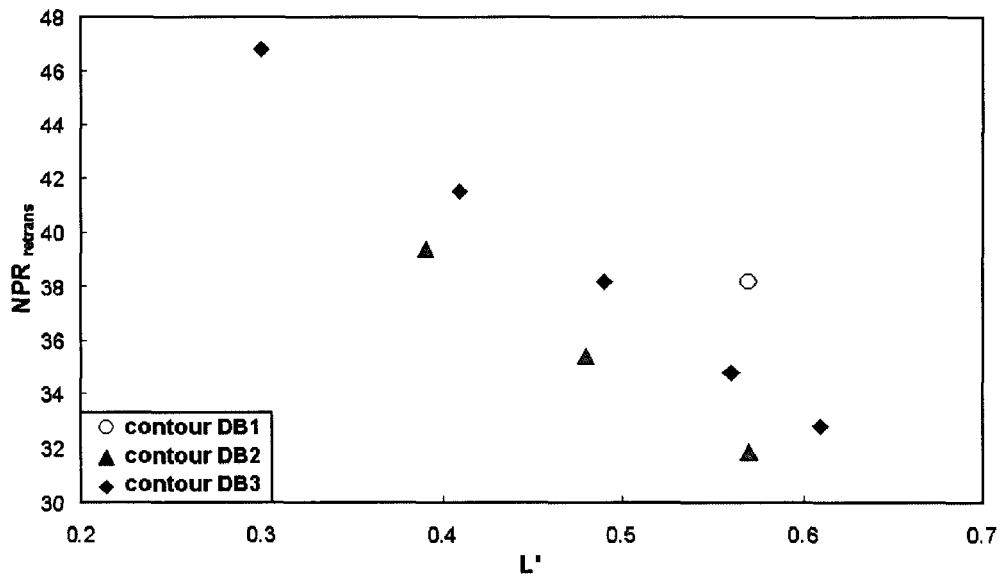


Figure 3.30: NPR at retransition for the various nozzle geometries

No explanation has been yet found for the lower value of NPR necessary for the retransition of the flow. An element of the answer is given in figure 3.31.

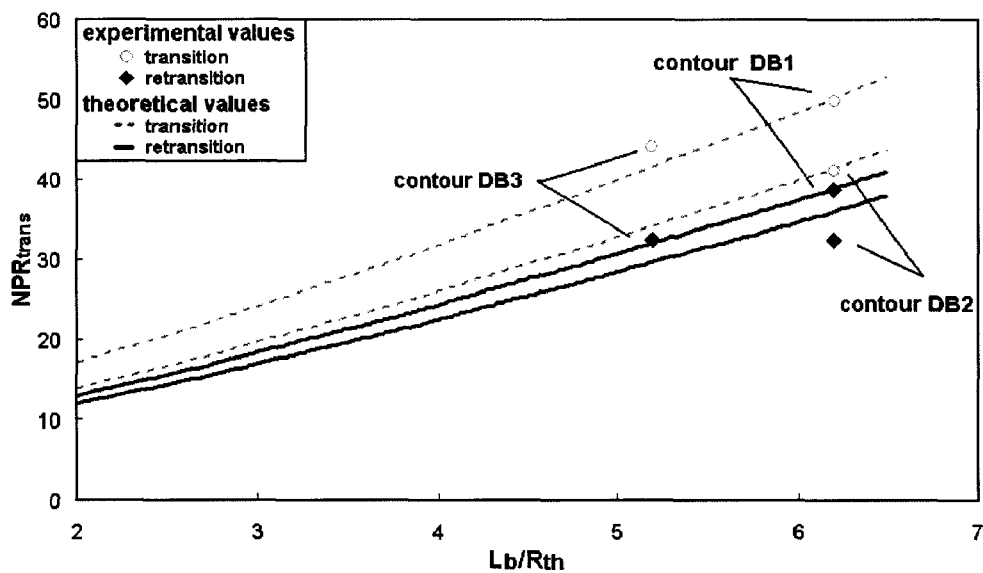


Figure 3.31: Retransition NPR as a function of the base length  $L_b$

The method used for the graph of figure 3.29 is applied for the retransition. The theoretical value of the retransition NPR is calculated with the pressure and Mach

number of the first measurement point in the extension (start of the inflection region). The experimental and theoretical values of the  $NPR_{trans}$  are plotted in addition to the  $NPR_{retrans}$  values for comparison purposes. The experimental values of the retransition NPR show a good accordance with the theoretical for nozzle models DB1 and DB3. However, the experimental values for nozzle model DB2 are still overestimated by the theory. The transition has been shown to be triggered by the separation conditions in the constant pressure part of the extension. The retransition may be triggered by the separation conditions in the vicinity of the inflection.

### 3.3.2 Hysteresis effect by the change of operating mode

The previous section has shown the influence of the various geometrical parameters on the transition and retransition conditions. All the parameters studied influence both transition and retransition in a similar way. The relative gap between the transition and retransition NPR is crucial for the stability of the flow mode. A significant hysteresis should avoid that a small variation of the NPR, due for example to  $P_0$  variation caused by combustion fluctuations or to  $P_a$  variation due to buffeting effect around the rocket engine during the flight, leads to an oscillation from one flow mode to the other. In order to evaluate the stability of a dual bell flow, the value of the hysteresis is calculated as the ratio of the difference between transition and retransition NPR over the transition NPR:

$$hysteresis = \frac{NPR_{trans} - NPR_{retrans}}{NPR_{trans}} * 100 \quad (3.7)$$

In the same way as in the previous study, the values of the transition and retransition NPR are recorded for each nozzle configuration and the hysteresis percentage is then calculated. The first parametric parameter is the length of the extension: the transition and retransition NPR have shown a linear relation to  $L'$ . Figure 3.32 summarises the data obtained from testing of dual bell nozzle contour DB3 for various extension lengths, during test series B (which presents the most different configurations).

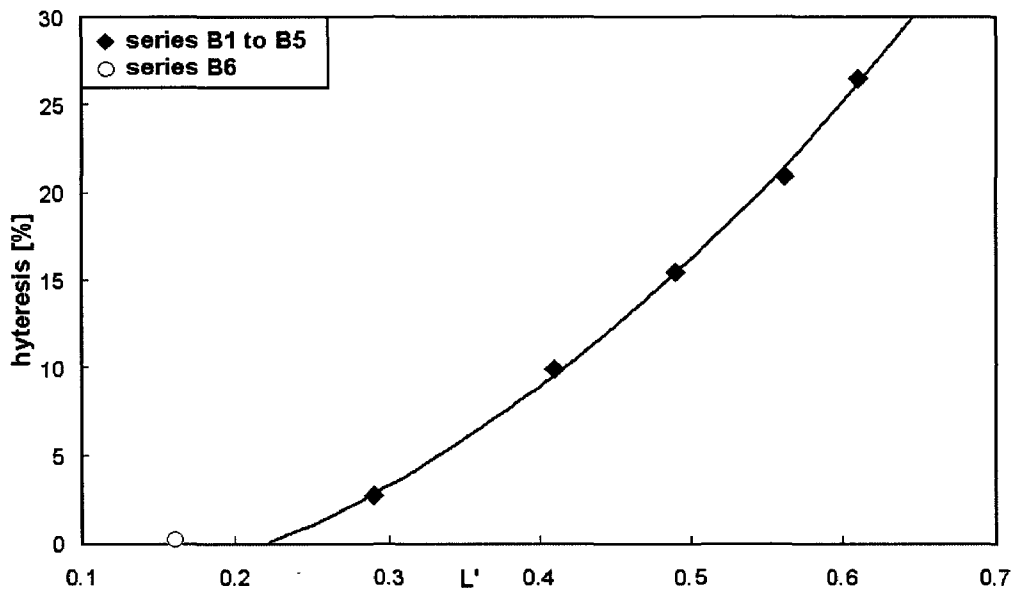


Figure 3.32: Hysteresis effect as a function of the relative extension length

Configuration B6 corresponds to a value of hysteresis equal to zero; indeed, no pressure jump was recorded. The dual bell extension was shortened up to the inflection region. The flow attaches progressively to the wall with increasing value of NPR. The extension behaves like a conventional nozzle wall, with a negative wall pressure gradient.

The values measured for configurations B1 to B5 can be very accurately approximate by a polynomial function of second degree, as presented in figure 3.32. This polynome crosses the abscissa at a relative length of about  $L' = 0.2$ . The relative extension length of contour DB3 in configuration B6 lies below this minimum value, so no hysteresis is possible as only sneak transition takes place. The graph shows that the stability of the system can be improved by choosing an appropriate extension length.

A second non-dimensional variable is introduced to define the extension length:  $L'' = L_{ext}/L_{init}$ , where the value  $L_{init}$  represents the total length of the nozzle in its initial configuration, before shortening. The measured hysteresis values are displayed in fig. 3.33 for every nozzle configuration as a function of  $L''$ . The variation of the hysteresis value varies linearly with the variation of  $L''$ , for every nozzle configuration tested [44]. The reference value for  $L''$  is taken for this study as the initial total nozzle length, which corresponds to a very small extension wall exit angle (less than  $4^\circ$ ). For nozzle design applications, the reference initial nozzle length  $L_{init}$

should be taken as the contour with an extension exit wall angle equal to zero.

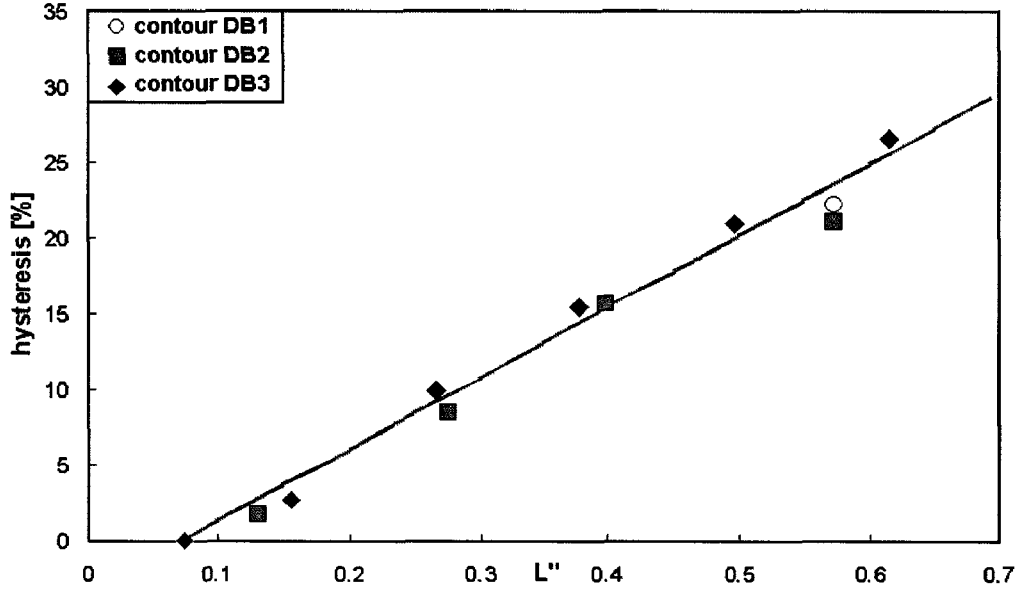


Figure 3.33: Hysteresis as a function of  $L''$  for the different test configurations

The value of the retransition NPR could be calculated using this linear variation of the hysteresis value with  $L''$ . The transition NPR is a function of the extension Mach number with:

$$NPR_{trans} = \frac{1}{M_e} \left( 1 + \frac{\gamma - 1}{2} M_e^2 \right)^{\frac{\gamma}{\gamma - 1}} \quad (3.8)$$

The hysteresis varies linearly with  $L''$  and can be written as  $hysteresis = a.L'' + b$ , where  $a$  and  $b$  are independent of the flow properties. By definition, the hysteresis is given as:

$$hysteresis = \frac{NPR_{trans} - NPR_{retrans}}{NPR_{trans}} * 100 \quad (3.9)$$

Which leads to:

$$NPR_{retrans} = NPR_{trans} \left( 1 - \frac{aL'' + b}{100} \right) \quad (3.10)$$

$$NPR_{retrans} = \frac{1}{M_e} \left( 1 + \frac{\gamma - 1}{2} M_e^2 \right)^{\frac{\gamma}{\gamma - 1}} \left( 1 - \frac{aL'' + b}{100} \right) \quad (3.11)$$

This relation should be verified with additional test data for different nozzle geometries and flow properties.

Contours DB1 and DB2 in full length possess the same base geometry and the same extension length. Hysteresis effects show only a small dependency on the inflection angle  $\alpha$ : 22.8% and 22.4% hysteresis for  $\alpha_1 = 7.2^\circ$  and  $\alpha_2 = 5^\circ$ . The results for the other geometric parameters are presented in figure 3.34 as a function of the base length.

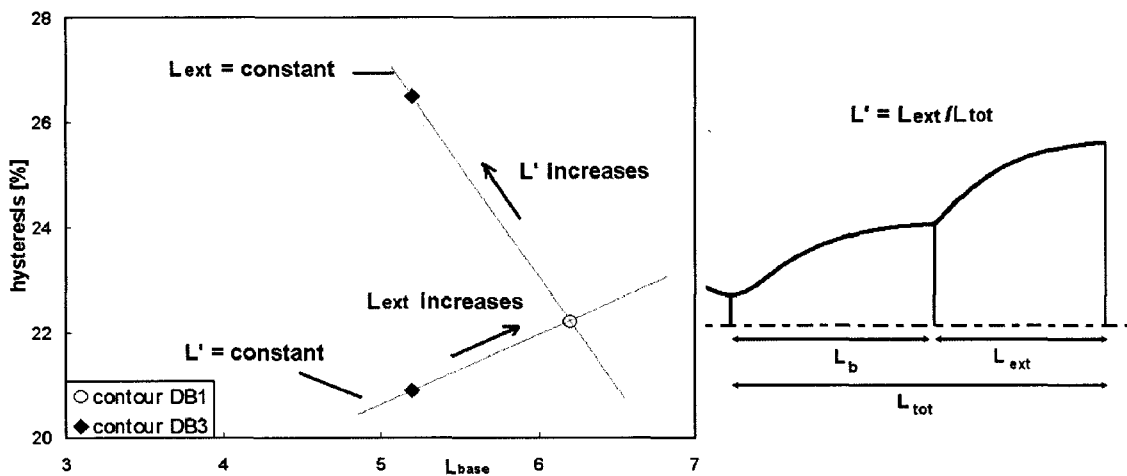


Figure 3.34: Hysteresis as a function of various geometric parameters

The graph illustrates the influence of the base and extension lengths on the hysteresis effect. Values for contour DB1 and DB3 in configurations B1 (same  $L_{ext}$  as contour DB1 and  $L'_1 < L'_3$ ) and B2 (similar  $L'$  and  $L_{ext,1} > L_{ext,3}$ ) are displayed. The hysteresis is depicted as a function of the base length  $L_{base}$ . For a similar value of  $L'$  the hysteresis value increases with the extension and base lengths. For the same value of  $L_{ext}$  the hysteresis increases with the value of the relative extension length (higher value for lower  $L_{base}$ ). This means that the base nozzle geometry has no significant influence on the hysteresis between transition and retransition of a dual bell nozzle.

The relative extension length  $L'$  is the outstanding parameter for the improvement of the dual bell nozzle flow stability. The gap between transition and retransition NPR can be increased by increasing the length of the dual bell extension.

### 3.3.3 Transition duration

This section presents the transition duration evaluations conducted for the investigated nozzle models. The estimation of the transition duration is critical for the prediction of the structure life time. During the transition from one mode to the other, the flow can present significant asymmetries which lead to high side loads. In order to prevent damages to the nozzle structure, the transition duration has to be minimised.

The high frequency wall pressure measurements along the extension allow the observation of the flow separation point displacement at the extension wall and the calculation of the time needed for the flow to attach in the complete nozzle extension. Two duration values can be defined: the total transition duration  $t_{tot}$  and the actual transition duration  $t_{trans}$ .

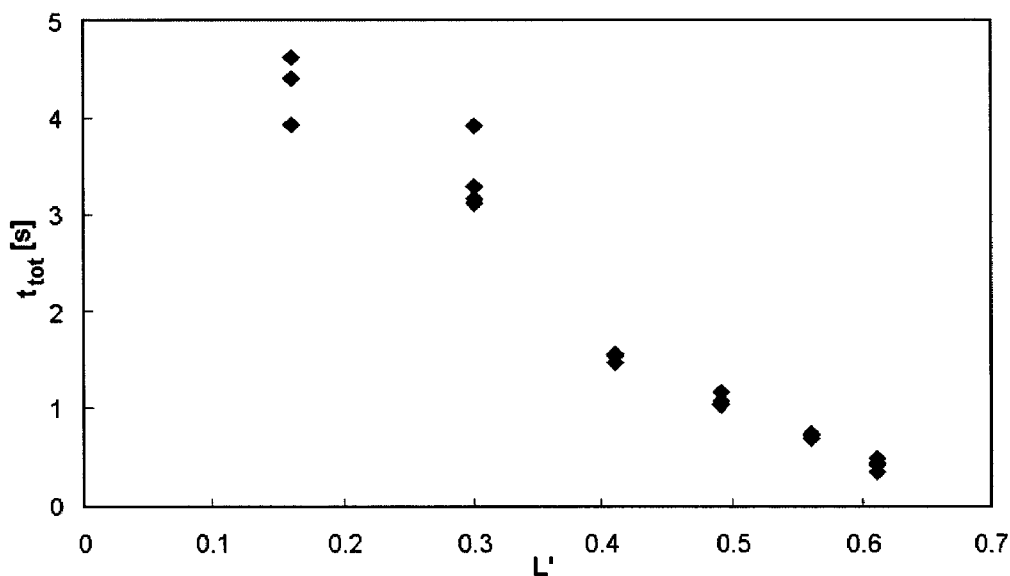


Figure 3.35: Total transition duration in the nozzle DB3 as a function of the relative extension length

The total transition duration,  $t_{tot}$ , corresponds to the time between the instant when the flow separation point first moves in the extension and the instant when it reaches the nozzle end (duration of transition plus sneak transition). The start of the transition is approximated with the pressure drop at the first sensor position in the extension ( $P_1$ ). It corresponds to the time at which the separation point is located in the extension, generating potential side loads. The actual transition duration  $t_{trans}$  is measured between the instant when the flow separation point leaves

the inflection region and the instant when it reaches the nozzle extension end. In this interval, the separation point is located in the constant pressure region of the extension. The maximum separation point asymmetry at the nozzle wall may reach the whole extension length and leads to high side load peak.

Figure 3.35 represents the total transition duration for the nozzle DB3 in configurations B1 to B6 as a function of the relative extension length.

The transition duration increases when decreasing the extension length, which is the contrary of the expected effect. For configurations B1 to B4, the influence of the extension length on the total transition duration,  $t_{tot}$ , appears to be linear. For the shortest configurations, B5 and B6, the values vary more significantly from one test to another. Moreover, the pressure drop at the sensors is smeared and it is difficult to detect the exact instant of transition.

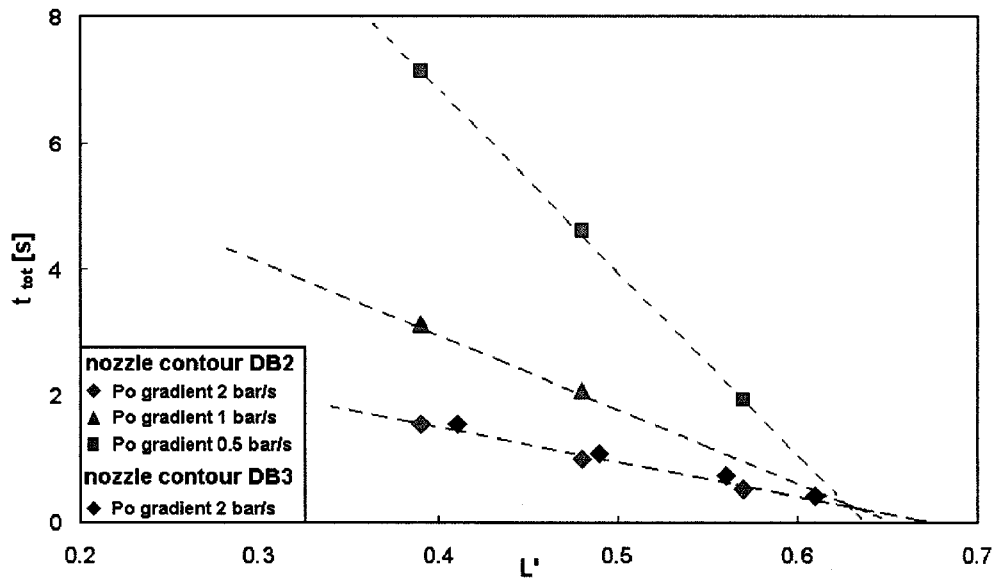


Figure 3.36: Total transition duration as a function of the relative extension length with various  $P_0$  variation gradients for the nozzle contours DB2 and DB3

Figure 3.36 represents the averaged total transition duration for the various configurations of the test series B and C (nozzle models DB3 and DB2). The results are given for configurations B1 to B4 and C1 to C3, for lengths with a clear flow transition. The duration measured for the nozzle contour DB2 is presented for three feed pressure gradients: +2 bar/s, +1 bar/s and +0.5 bar/s. The tests on nozzle DB3 were conducted with a feed pressure variation gradient of +2 bar/s. The to-

tal duration increases with decreasing gradient. This effect has to be taken into account for flight conditions because the NPR variation, due only to the ambient pressure variation, is very low. The total transition duration decreases linearly with increasing extension length. A minimum value seems to be common for all NPR variation gradients, which indicates the existence of an unique optimal transition time corresponding to an extension relative length of about 0.63.

The product of the total duration and the feed pressure gradient is plotted over the relative extension length in figure 3.37. The value varies linearly with  $L'$  for the two nozzle geometries. The transition duration appears to be only a function of the extension length and the variation gradient of the NPR.

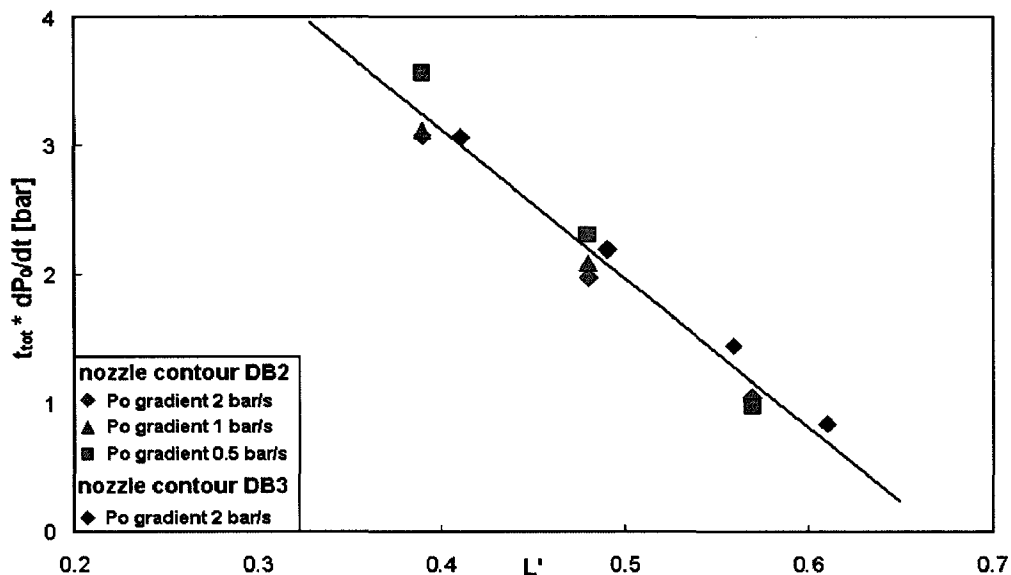


Figure 3.37: Transition duration relative to NPR gradient

For the same pressure gradient, nozzles DB2 and DB3 show a similar behaviour. The base nozzle length and the inflection angle have no significant influence on the total transition duration. In the following paragraphs, only the results obtained for nozzle contour DB3 are presented, as this contour was tested under a higher number of extension length configurations.

Both values of the averaged  $t_{tot}$  and  $t_{trans}$  are presented figure 3.38 as a function of the relative extension length (configurations B1 to B6). Only  $t_{tot}$  is given for configuration B6 as no fast transition takes place for this extension length.

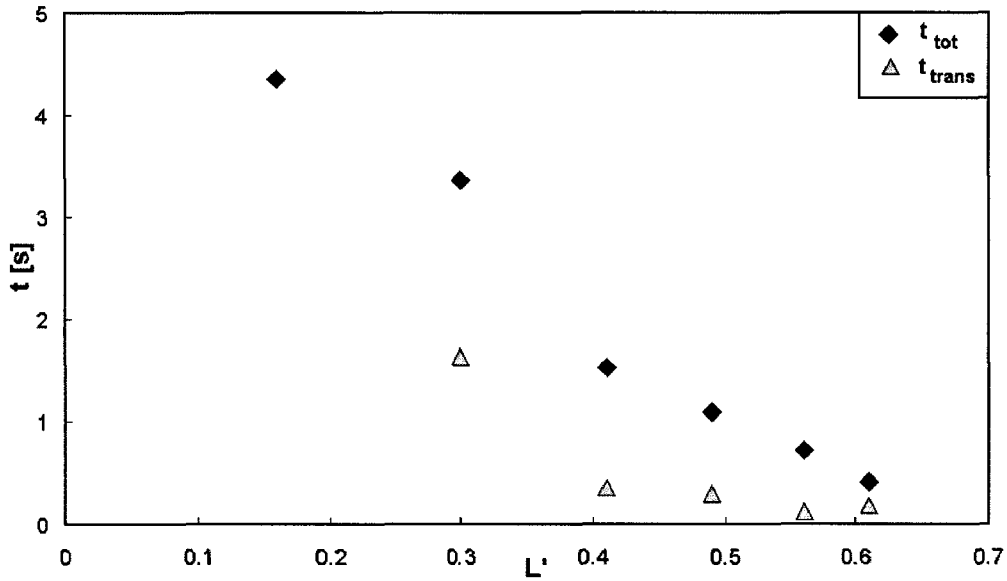


Figure 3.38: Transition and total duration with the relative extension length

Looking at the transition duration  $t_{trans}$  (see fig. 3.38), the values are much lower, but show a similar trend. With a shorter nozzle configuration, the flow stays longer in the inflection region and also needs more time to go through the rest of the extension, to the end of the nozzle.

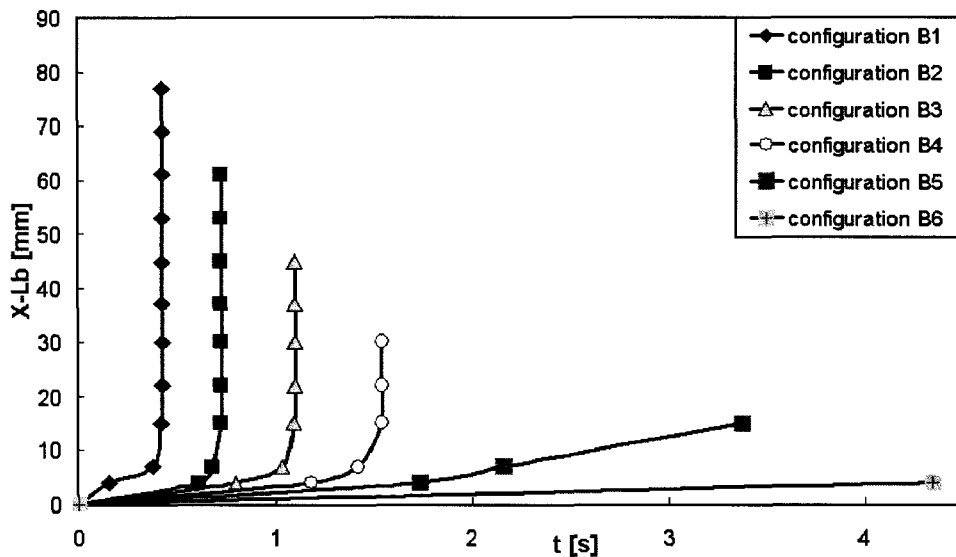


Figure 3.39: Position of the separation point in the extension for the various configurations of nozzle contour DB3

The time required for the sneak transition is about 0.3 s for the nozzle at its full length, double for the second series, reaches over 1 s for the fourth length and reaches 4 s for the shortest configuration. The relative extension length has a higher influence on the total duration (from inflection to nozzle end) than on the transition duration (from inflection region to nozzle end). This effect is mostly due to the NPR difference between the two steps of the transition: the time spent in the inflection region depends for some part on the low NPR gradient ( $P_0$  variation gradient of 2 bar/s).

The instant at which the wall pressure dropped at the extension wall was measured and averaged for the various configurations of test series B. The graph in figure 3.39 represents the position in the extension over the time needed for the flow to reach that position once it starts moving along the extension wall. The displacement in the inflection region is slow. The flow transition front then accelerates in the constant pressure region of the extension. The shortest configurations, B4 and B5, show a different behaviour: no fast displacement of the transition takes place between the measurement points. This effect was predictable for configuration B6 because no transition takes place. In case of configuration B5, a fast transition is not visible because only one measurement point is available in the constant pressure region.

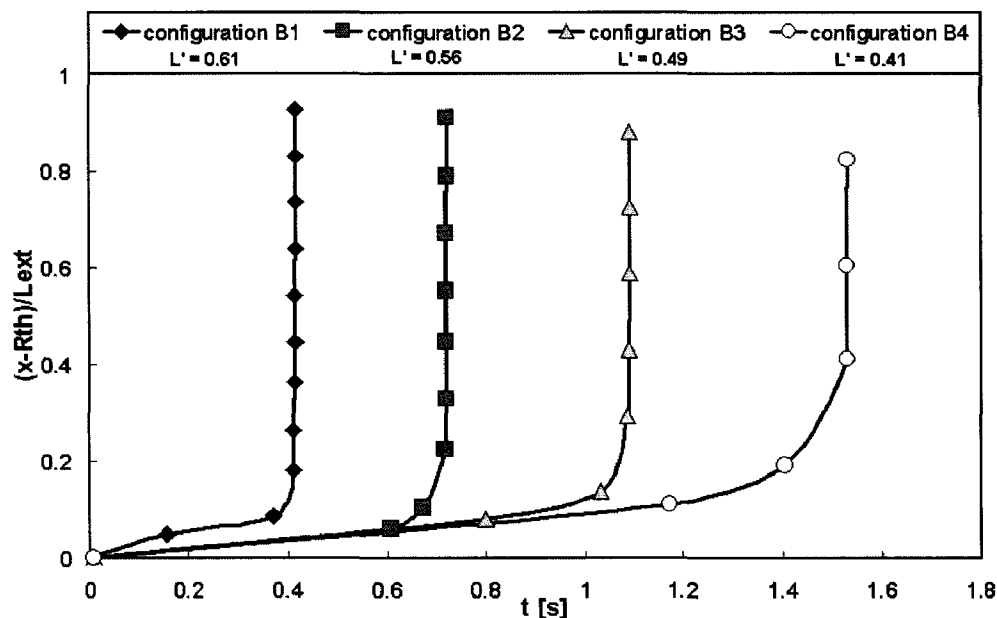


Figure 3.40: Evolution of the separation point toward the relative position in the extension for the nozzle configurations B1 to B4

In figure 3.40 the displacement of the transition point is presented for configurations B1 to B4 over the relative position in the extension  $((x - L_b)/L_{ext})$ . The two steps of the transition can be clearly identified: at first the flow moves slowly into the inflection region, this is the sneak transition and once the transition NPR is reached, the flow moves very quickly up to the end of the nozzle. The duration of the sneak transition increases with decreasing extension length. The evolution of the transition front is then comparable for all four nozzle lengths.

The maximum velocity attained by the transition front has been calculated as the time between the instant of the pressure drop between two successive measurement points. The values of the velocity are depicted in figure 3.41 for various  $L'$  of contour DB3. Not only is the transition time shorter for the longer extensions, but the transition front also moves faster. The theoretical maximum velocity of the transition front would be the velocity of the flow itself.

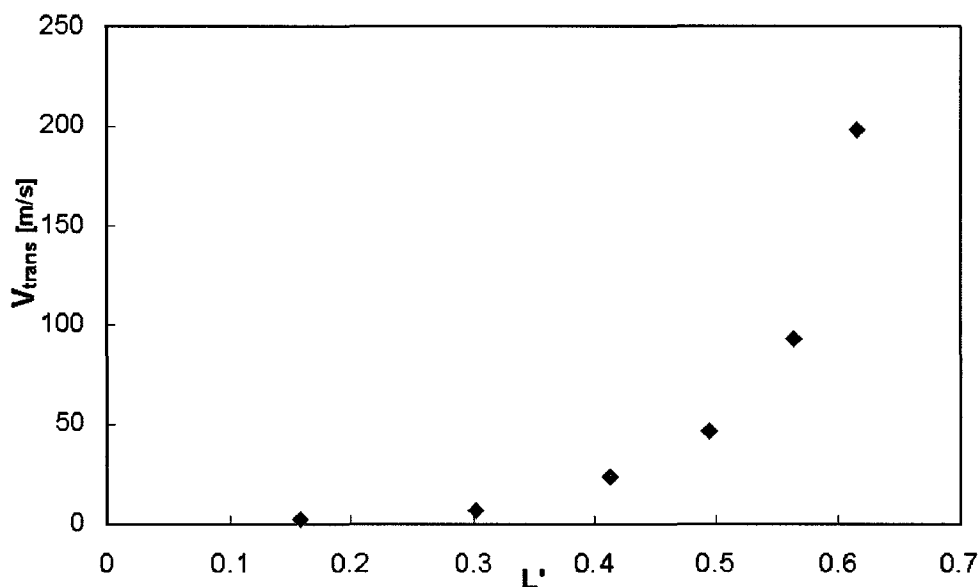


Figure 3.41: Maximum transition front velocity as a function of the extension length

The position of the separation point in the extension has also been recorded and averaged for the retransition. Figure 3.42 represents the evolution of the separation point for various nozzle configurations. The origin is placed at the inflection, so that the value of  $t$  at the last point corresponds directly to the retransition duration. The last point has not been taken into account because of the nozzle end effect that induces a pressure raise before the start of the retransition. The longest configurations (B1, B2 and C1) present a faster evolution, but a longer duration. Configurations

B3 and C2 for nozzle DB3 and DB2 possess a similar relative extension length and show the same evolution of the retransition front.

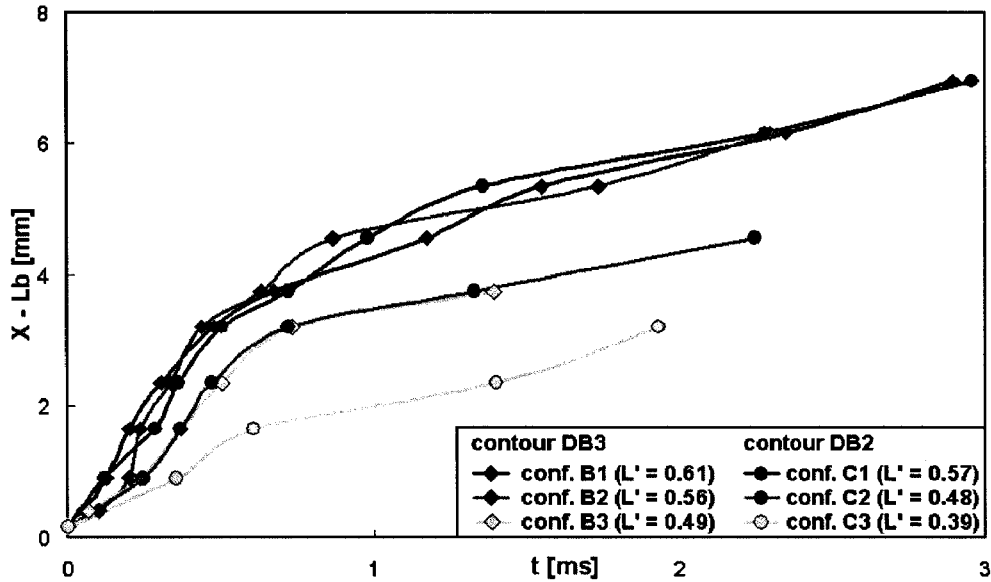


Figure 3.42: Evolution of the separation point during retransition for various nozzle configurations

Configuration	$L'$	Duration
A1	0.57	22 ms
B1	0.61	25 ms
B2	0.56	23 ms
B3	0.49	14 ms
B4	0.41	0.2 s
B5	0.3	3.5 s
B6	0.16	4.2 s
C1	0.57	29 ms
C2	0.48	24 ms
C3	0.39	19 ms
C4	0.23	2 s

Table 3.6: Duration of the flow retransition for various nozzle configurations

Table 3.6 summarises the retransition durations for all the dual bell nozzle investigated in this study. The retransition is very fast (less than 30 ms) for the longest configurations. By shortening the extension nozzle, the retransition duration at first

decreases: the distance to overcome for the separation point becomes shorter (see configurations B1 to B3 or C1 to C3). When the extension length further decreases, the nozzle end comes closer to the inflection region. The constant pressure region becomes smaller and the nozzle loses progressively its dual bell characteristics. The retransition time increases by shortening the extension and reaches values of up to 4 s for the shortest configuration ( $L' = 0.16$ , configuration B6).

Two of the most important parameters for the optimisation of the dual bell concept show a good correlation: transition stability and duration can be improved by increasing the length of the extension nozzle. However, the variation gradient of the NPR has to be high enough to reduce the transition duration. The retransition is very fast for relative extension lengths over 0.4.

### 3.4 Side loads

Flow separation and side load generation are critical points in nozzle investigation. In the case of a dual bell nozzle, the flow is fixed at the wall inflection in the sea level mode, avoiding any asymmetric flow separation. However, during the transition to the high altitude mode, the flow separation moves downwards in the extension to the nozzle end. This movement potentially generates very high side loads, which can damage the whole structure: nozzle, launcher and payload.

For all of the three nozzles tested for this study, the strain gauges have been calibrated for the nozzle at its initial full length. The values presented are given in Newton and corresponds to the equivalent static force acting at the nozzle end, perpendicular to the symmetry axis. The shortened configurations are related to the full length configuration for easier comparison of the measured forces.

The side loads generated by nozzle DB2 under its various configurations of test series C are presented in figure 3.43. The measurements are given as a function of the NPR, for a gradient  $dP_0/dt > 0$  (left) and  $dP_0/dt < 0$  (right).

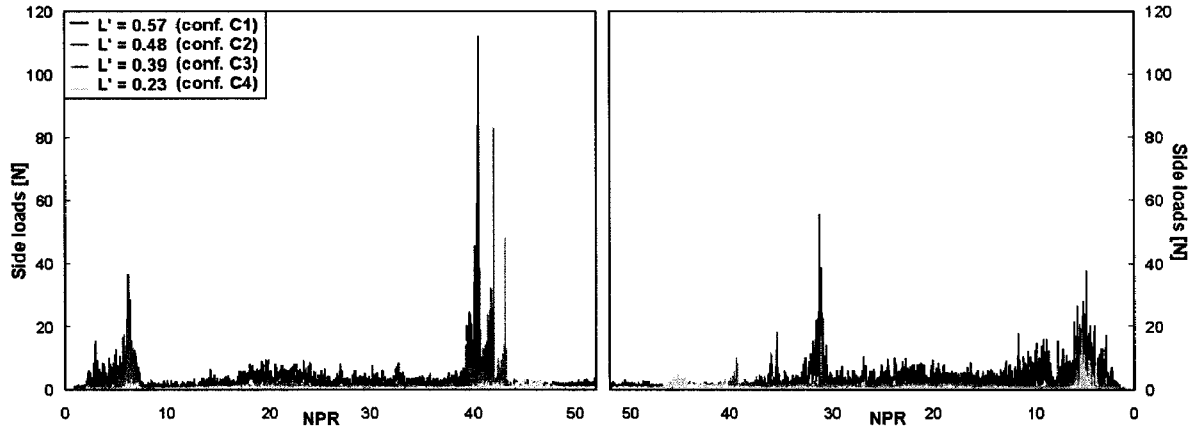


Figure 3.43: Side load measurements for various nozzle lengths for increasing (left) and decreasing (right) NPR

Engine start up generates relatively high side loads: for all configurations the averaged value is 10 N and peak values reach 30 N for NPR values between 2.5 to 7. Such high loads are due to the transition of the boundary layer from laminar to turbulent in the throat region, which leads to a partial flow reattachment, as described by Stark [58]. By increasing the NPR (from 8 to about 30), the flow progressively attaches to the base nozzle wall. The sea level mode is reached for a

NPR value of 30: the flow is attached in the whole base nozzle and separates at the inflection. The side loads are moderate, about 4 N, during the sea level mode. When further increasing the NPR value, the transition NPR is reached and the flow separation point jumps to the end of the extension nozzle. The nozzle is then full flowing. The transition leads to a very high peak of side loads, over 100 N for the longest configuration. The peak amplitude decreases with the extension length: the maximum separation position asymmetry is between the inflection and the nozzle end. In configuration C4, no actual transition takes place, so no peak in side loads was measured. Once the high altitude mode is reached, the flow is fixed at the nozzle end and the side loads are very low, with an amplitude of about 2 N.

The second curve in figure 3.43 depicts the side load evolution with decreasing NPR values. The high altitude mode still generates very low side loads. Retransition is reached for the shorter configurations first ( $NPR_{retrans} = 46$  for configuration C4, 40 for configuration C3). A side load peak marks the flow retransition to the sea level mode. However, its amplitude is much lower than the transition peak: half its value for configuration C1, one fourth for configuration C2 and as little as one fifth for configuration C3. The calm sea level mode is characterised by moderate side loads. For configuration C1, the NPR values of retransition and separation at the base nozzle end are close ( $NPR_{retrans} = 32.5$  and NPR separation at the base nozzle end is about 30), so the sea level mode is difficult to define. The flow separation moves upstream to the throat when the NPR value is further decreased. Between NPR values of 8 and 2, the shut down of the nozzle generates higher side loads with an amplitude of up to 40 N in configuration C1 and up to 20 N in configurations C2 and C3.

The generation of side loads depends on the dual bell geometry: the longer the extension, the higher the peak in the side loads during both transition and retransition because of the longer lever arm. The extension length therefore has to be a compromise between flow transition stability and side load peak generation.

The influence of the other geometric parameters can be seen in figure 3.44 for representative measurements for each configuration. The side load measurements are presented as a function of the NPR for  $dP_0/dt > 0$  for the three nozzle contours in their initial configuration ( $L_{tot}/R_{th} = 8.3$ ). Contours DB1 and DB2 possess the same base nozzle length  $L_{b1}/R_{th} = L_{b2}/R_{th} = 6.2$  and different inflection angles ( $\alpha_1 = 7.2^\circ$  and  $\alpha_2 = 5^\circ$ ). Contours DB1 and DB3 present the same inflection angle, but a different base geometry ( $L_{b3}/R_{th} = 5.2$ ).

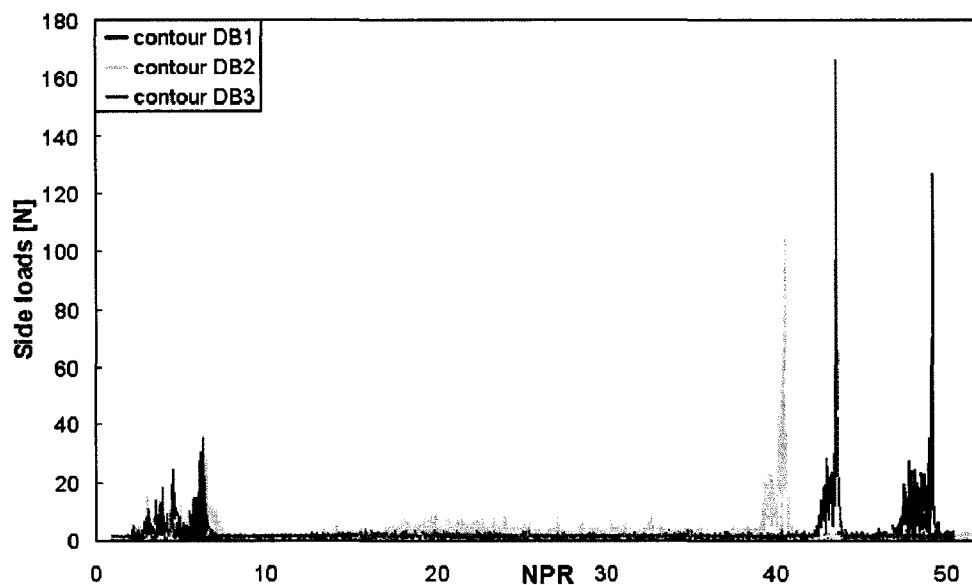


Figure 3.44: Side load measurements during flow transition for various nozzle configurations

The side load amplitudes during start up (NPR values between 2.5 and 7) are comparable for all three nozzle contours: they all present the same geometry in the throat region. For NPR values between 8 and 30, the flow attaches in the base nozzle generating side loads with low amplitude: about 3 N for contours DB1 and DB3, about 7 N for contour DB2. Sneak transition is then characterised by higher side loads, around 30 N for every configuration. The peak amplitude is higher for nozzle DB3, with a maximum of 170 N. Contours DB1 and DB2 lead to a side load peak of respectively 120 N and 110 N. The inflection angle has no significant influence on the amplitude of the maximum side load peak during transition. The base nozzle, however, has a significant influence on the peak: the shorter base nozzle of contour DB3 leads to a side load peak 30% to 45% higher than that obtained with the other contours.

Figure 3.45 depicts the transition in the side load peak for nozzle DB2 and nozzle DB3 in configurations B1 and B2, and allows the investigation into the base nozzle length influence on the side load peak amplitude. The relative extension lengths are  $L' = 0.61$  for nozzle DB3 in configuration B1,  $L' = 0.56$  for configuration B2 and  $L' = 0.57$  for nozzle DB2. The side load peak is much higher for configuration B1 than for the other two nozzles (170 N to 110 N and 90 N). The base nozzle length only influences the peak amplitude through the relative extension length  $L' = L_{ext}/L_{tot}$ .

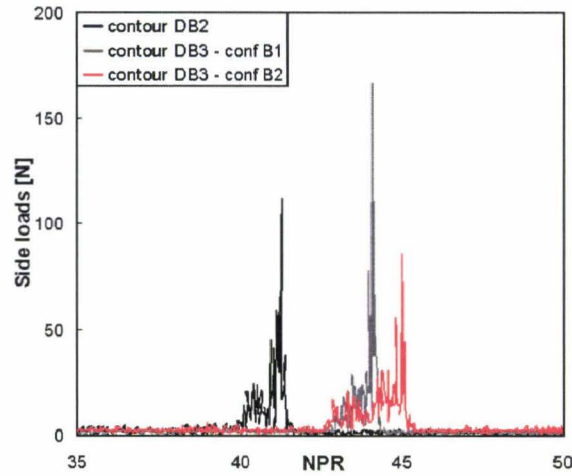


Figure 3.45: Side load generation for  $L_b$  and  $L_{ext}$

Figure 3.46 depicts the side load generation for decreasing NPR values. The same remarks can be made as for transition: the retransition peak is higher for the contour with a higher value of  $L'$ : contour DB3. The amplitude of the generated peak is similar for contours DB1 and DB2. As the flow separation point moves along the base nozzle wall (NPR between 30 and 8), the side loads are higher, particularly for contour DB2. The shut down side loads are comparable in amplitude with those at start up and show no dependency on the dual bell nozzle geometry.

The lower inflection angle of contour DB2 leads to higher side loads for low NPR values, when the flow separates at the base nozzle wall. The transition peak is similar for contours DB1 and DB2, which have the same relative extension length  $L'$ . The higher values of  $L'$  of contour DB3 lead to a higher maximal peak amplitude. The side load amplitude can be limited by choosing the appropriate nozzle geometry: a large inflection angle and a limited relative extension length.

Sneak transition is a critical phenomenon for the qualification of a dual bell nozzle concept. The movement of the separation point along the nozzle extension can be the source of higher side loads of the same amplitude as those encountered during start up. Figure 3.47 represents the evolution of the wall pressure in the inflection region (sensor position  $P_{w1}$ ) and in the extension (sensor position  $P_{w11}$ ) and the side load amplitude in dual bell DB1. Prior to  $t = 26.5$  s, the nozzle operates in sea level mode; the side loads are smaller than 5 N. Sneak transition starts as the pressure drops at the first position in the inflection region. The separation point has left the inflection and is no longer symmetrical. The side load amplitude increases with peaks over 30 N. The transition peak corresponds to the pressure drop in the

extension.

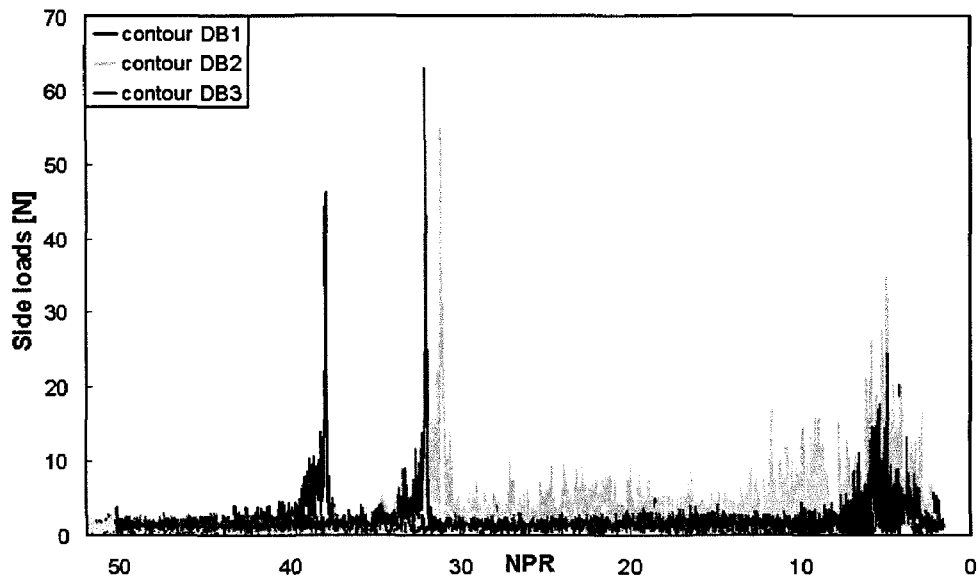


Figure 3.46: Side load measurements during the retransition for various nozzle configurations

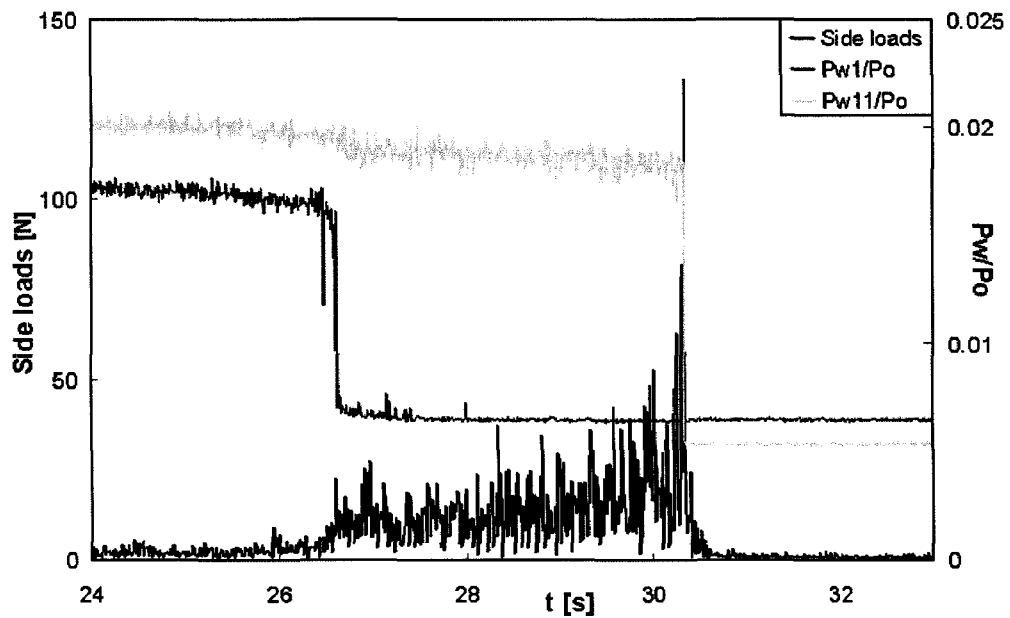


Figure 3.47: Side loads and wall pressure measurements during transition and sneak transition

Sneak transition duration has to be reduced as much as possible to limit the generation of structural loads. The geometry of the dual bell extension model should be optimised in order to limit the inflection region. The difference between the sneak transition NPR and the transition NPR can also be reduced when increasing the extension length. Another possibility to reduce the duration of the high side load generation is to suddenly increase the NPR. Therefore, the combustion chamber pressure would first have to be reduced and then abruptly brought back to its initial value when the ambient pressure is low enough to ensure a fast sneak transition.

Side load measurements have been made with the same installations on truncated ideal nozzles by Stark and Wagner [58]. The geometrical parameters are presented in table 3.4 together with the parameters of dual bell nozzle contour DB2. The nozzle geometries are close and the side loads generated from these nozzles are comparable.

	TIC nozzle	Nozzle DB2
Throat radius $R_{th}$	10 mm	10 mm
Area ratio $\epsilon_e$	20	24
Total length $L_{tot}/R_{th}$	14.24	14.5

Table 3.7: Nozzle geometry comparison

Figure 3.48 illustrates the side load measurements as a function of the NPR for the TIC and the dual bell nozzles. The start up side loads present a similar amplitude for the two nozzle types: 30 to 40 N for NPR values up to 7. When increasing the NPR, the flow separation point moves downstream along the nozzle wall. The flow is fully attached in the TIC for a NPR of about 50 and it is attached in the base nozzle of the dual bell for a NPR of 30. The side loads generated during the flow attachment at the wall is three time higher in the TIC as in the dual bell. However, the transition into the high altitude mode leads to a peak in the side load in the dual bell which is twice as high as the maximum side load in the TIC. Sneak transition leads to side loads of the same amplitude as for separated flow in the TIC. Once the high altitude mode is reached, the side loads in the dual bell are lower (two to three times lower amplitude) than the side loads in the full flowing TIC.

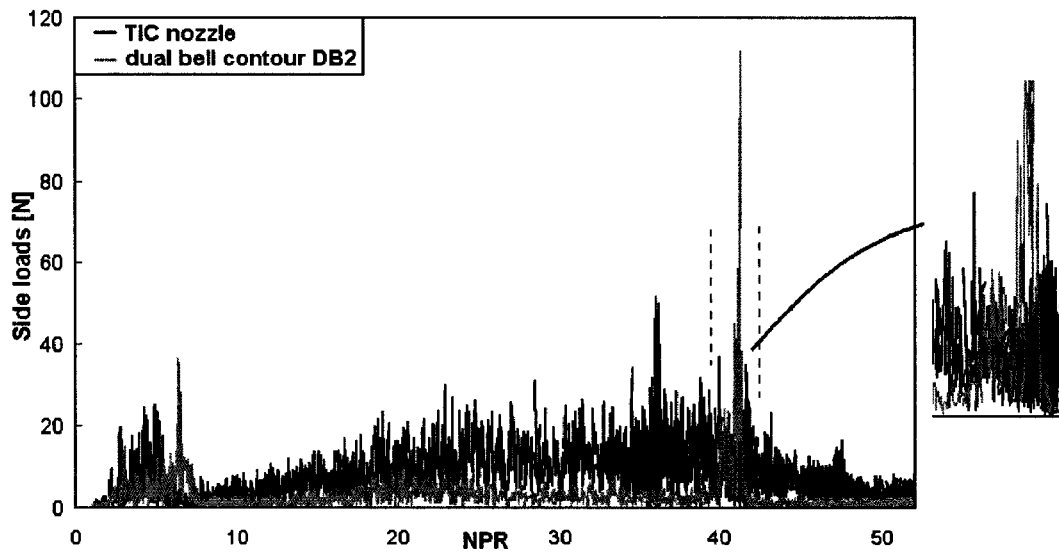


Figure 3.48: Comparison of the side load generation for a TIC and a dual bell nozzles

In its operating modes, a dual bell nozzle produces less side loads than a conventional TIC nozzle. However, the amplitude of the experimented peak during the transition is very short but also very high and can seriously harm the engine structure.

### 3.5 Conclusion

The cold flow study on dual bell nozzle models has confirmed the theoretical flow behaviour. The sneak transition, intermediate flow state between sea level and high altitude modes, has been pointed out. This effect is due to flow viscosity and is independent of the nozzle geometry. The higher side loads generated during the sneak transition make this effect a critical issue for future studies on dual bell nozzles.

The influence of the various geometrical parameters on dual bell flow behaviour can be summarised as follow:

- The transition NPR increases with the inflection angle  $\alpha$ .
- The sea level performance decreases and the transition NPR increases when the base nozzle length  $L_b$  increases.
- Inflection angle and base length have no significant influence on the hysteresis effect or on the transition duration.
- The extension length has a crucial influence on the flow transition. When increasing the relative extension length  $L'$ , the hysteresis increases (better stability of the flow modes against pressure variations) and the transition duration decreases. However, the peak in side loads measured during the transition increases with the value of  $L'$ . The extension length has to be a trade off between the side loads duration and amplitude during the transition.
- The NPR gradient influences the transition duration:  $t_{trans}$  can be reduced using a higher NPR gradient.

# Chapter 4

## Thermal study

The first part of the experimental work presented in this study was the investigation of cold flow behaviour in sub scale dual bell nozzles. The results define the conditions of utilisation and optimisation of those nozzles. In order to qualify the dual bell nozzle concept for main engine application, an investigation of the thermal loads is necessary to adapt the cooling system to the needs of this concept.

The second part of this work presents the test campaign conducted for hot flow conditions at the DLR test bench M11.4. Temperature and pressure measurements were made to determine the thermal loads under both flow operating modes.

### 4.1 Test conditions

#### 4.1.1 Test bench M11.4

The test bench M11.4 at the DLR Lampoldshausen was designed for the investigation of ramjets, scramjets and small supersonic nozzles. An air heater produces hot air at pressures of up to 30 bar using four hydrogen-oxygen burners. The air temperature can reach 1500 K (see details by Scheel [54] and Ciezki [2]). Flow temperature and pressure are adjusted by varying the hydrogen, oxygen and air mass flows. The hot flow is composed of air with about 10% water vapour for the test conditions presented in this study. The nozzle model is mounted on a horizontal rig, comparable to the installation of test bench P6.2. The tests are conducted under ambient conditions ( $P_a = 1 \text{ bar}$  and  $T_a = 290 \text{ K}$ ). The installation is schematized in figure 4.1

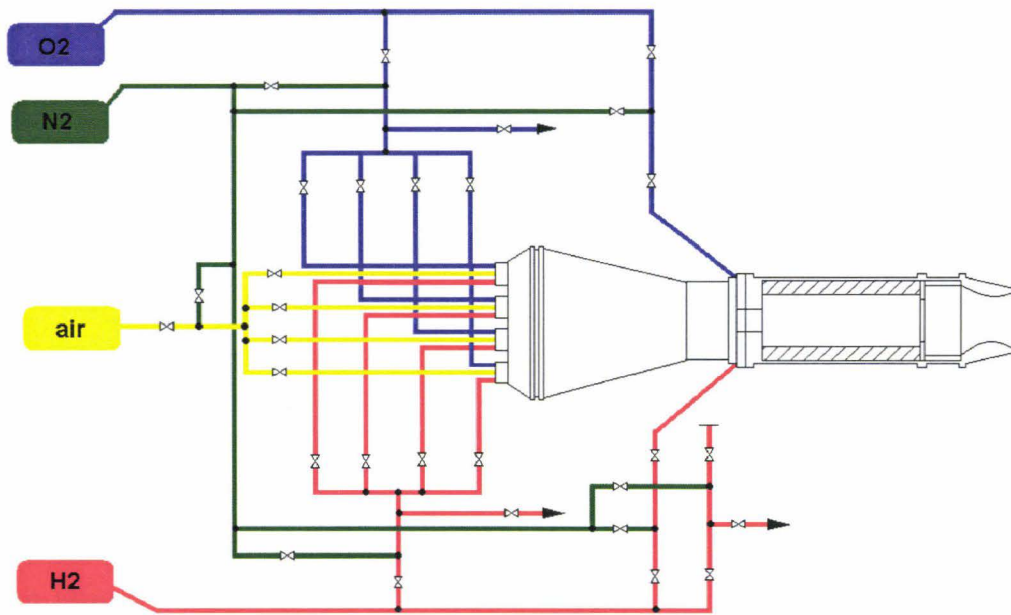


Figure 4.1: Principle scheme of test bench M11.4

The number of channels available for pressure and temperature measurement is limited. The measured data are recorded in series with a time shift of at least 0.01 s between two channels. The sampling rate is then proportional to the number of channels.

The conditions reached on the test bench M11.4 ( $P_0 = 30 \text{ bar}$  and  $T_0 = 1500 \text{ K}$ , sub scale nozzle) are still far from real flight conditions. The main advantage however is the possibility of testing a small nozzle model without a cooling system. A film cooling for example would produce a secondary flow which significantly influences the flow separation condition (as seen during the test campaign CALO at DLR Lampoldshausen [9], [16]), and hence the dual bell flow mode. A cooling system would also disturb the investigation of thermal loads at the nozzle wall by increasing the number of influence parameters.

Figure 4.2 is a picture of the dual bell nozzle model mounted and instrumented on the installation of test bench M11.4.

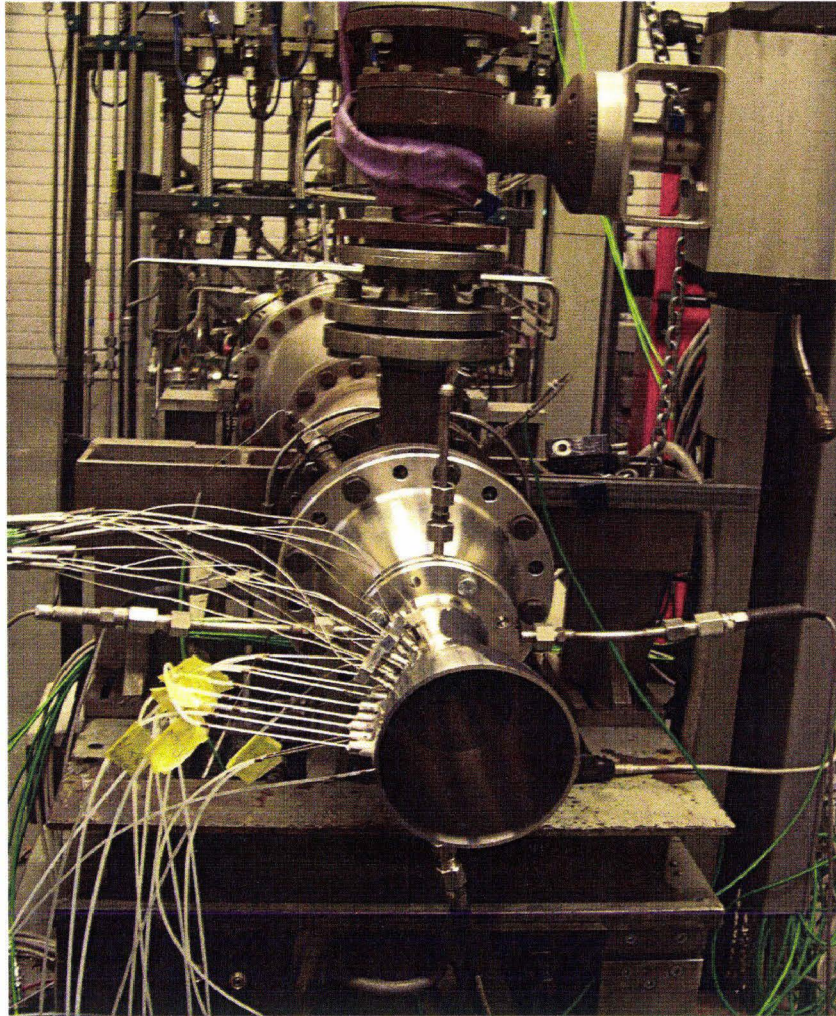


Figure 4.2: Dual bell nozzle model mounted on test rig M11.4

### 4.1.2 Nozzle model

The limitation in the maximum available NPR imposes to modify the geometry of the nozzle model used for cold flow investigation. The nozzle model tested on the M11 test bench is a dual bell with a TIC base nozzle and a CP extension. The nozzle is designed with the same method as presented in the previous chapter, which is based on the method of characteristics. The geometrical parameters are given in table 4.1. The throat section,  $R_{th} = 15 \text{ mm}$ , is set by the maximum mass flow delivered by the installation.

Throat radius	$R_{th}$	15 mm
Area ratio	$\epsilon_1$	6.2
	$\epsilon_2$	14.3
Base length	$L_b/R_{th}$	4.7
Total nozzle length	$L_{tot}/R_{th}$	10.7
Relative extension length	$L'$	0.56
Inflection angle	$\alpha$	$11^\circ$

Table 4.1: Contour geometry of the nozzle tested at M11.4 test bench

The inflection angle defines the transition conditions ( $NPR_{trans}$ ). Its value is limited by the maximum pressure supplied by the test bench ( $P_0 = 30 \text{ bar}$ ). The theoretical transition NPR is 25.8 for an inflection angle  $\alpha = 11^\circ$  using the same calculation method as presented in the previous section. This geometry enables both dual bell flow modes in the operational testing domain of the test bench.

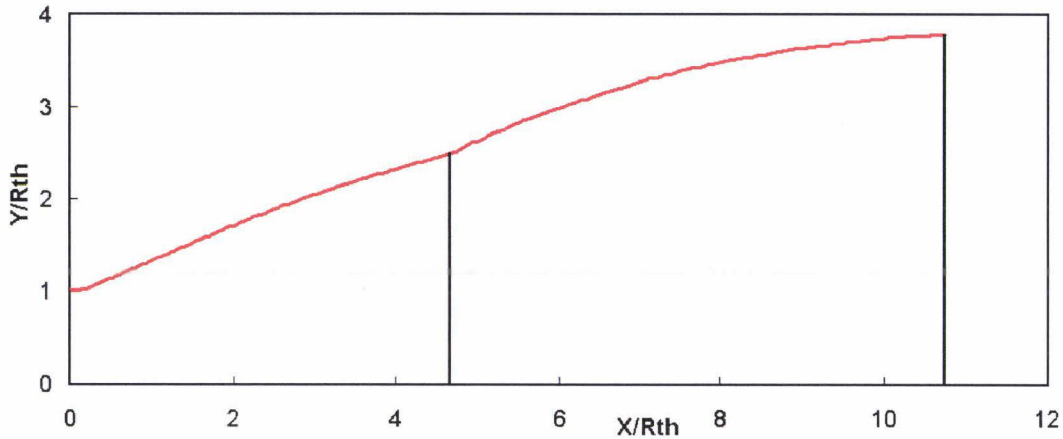


Figure 4.3: Nozzle contour geometry

The test campaign on dual bell nozzle model was the first campaign made on the bench M11.4 with an axisymmetric nozzle of such dimensions. It was also necessary to design a contraction section upstream to the convergent nozzle part. The geometry was chosen so as to generate an uniform axial flow. The method presented by Börger in [1] was therefore applied in a design program. The contraction ratio is given as input and the length and geometry of the contraction are computed by the program. The contraction ratio is here 2.66 and leads to a length of 106 mm. The contraction and the nozzle are depicted in figure 4.4.

Thermal imaging was used to complete the wall temperature measurement using thermocouples. It is impossible to observe the intern nozzle wall without using a bulky and expensive protection of the installation. To circumvent this problem, the observation of the wall is made from the outside. In order to improve the measurements, the wall thickness was reduced to its minimum value: 3 mm in the extension and in second half of the base nozzle (see fig. 4.4) and 10 mm in the throat region to resist the higher flow pressure and temperature. The thermal flux in the throat region is of secondary interest for this study because it corresponds to the flux in a conventional nozzle.

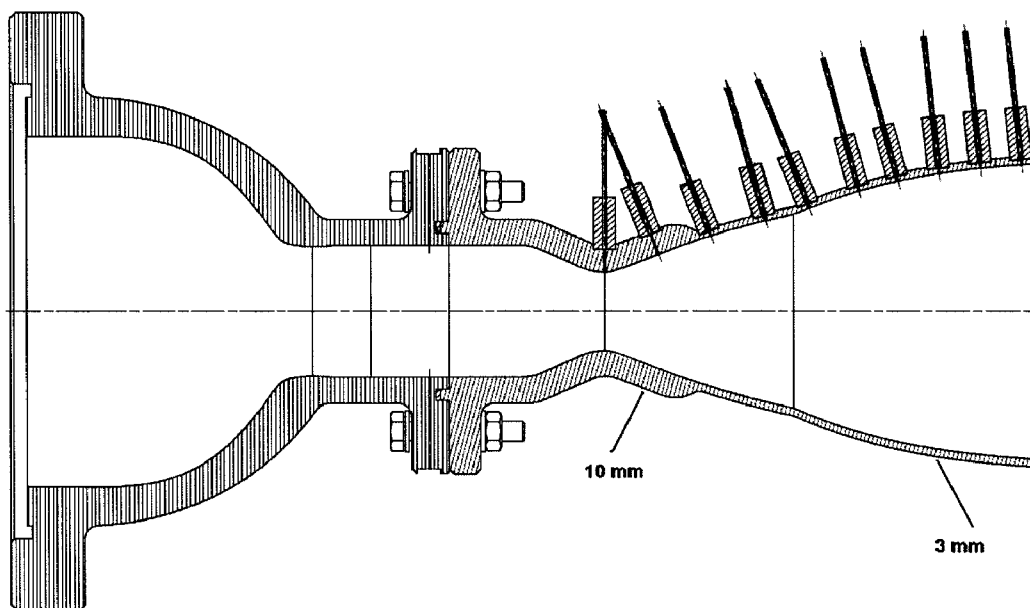


Figure 4.4: Nozzle model and section contraction geometries

The absence of cooling imposes the use of a heat resistant material for the nozzle and the section contraction wall. A heat resistant steel alloy was chosen: “Ferrotherm 4841 X15CrNiSi 25 20”, which has a melting point is over 1650 K. Its thermal conductivity is of  $k = 15 \text{ W/m.K}$  under 300 K and  $k = 19 \text{ W/m.K}$  under 800 K.

### 4.1.3 Instrumentation

#### 4.1.3.1 Pressure measurements

The first aim of the nozzle wall pressure measurements is to confirm the conclusions resulting from the first part of this study for flow under warm gas conditions. The

second purpose is to provide information on the flow operating mode. The thermal loads at the nozzle extension wall are defined by the flow mode: sea level, high altitude, or even sneak transition.

Various positions were chosen for the wall pressure measurements performed in the base nozzle and in the extension. The axial positions of the pressure sensors are indicated in table 4.2 and illustrated in figure 4.7. The sensors used are the same as those already presented in the cold gas flow study (see section 3.1.3.1): “Kulite Semi-conductor Inc.”, model XT-154-190M.

	Designation	Position [mm]
Base nozzle	P1, P1Q4	0
	P2	20
	P3	40
	P4	60
Extension nozzle	P5Q4	72
	P6	75.98
	P7Q4	80
	P8	95
	P9	110
	P10	125
	P11	140
	P12	155

Table 4.2: Position of the wall pressure measurement points

The positions P5Q4 and P7Q4 are shifted toward the axial alignment (with an angle of  $-20^\circ$ ) in order to get a better measurement resolution in the inflection region.

The test conditions at the test bench M11.4 include flow temperature up to 1300 K without cooling system for the nozzle wall. The high wall temperatures impose to protect the pressure sensors from high thermal loads. Small high temperature resistant steel cylinders were mounted at the nozzle wall in which a thin tube was fixed. A Teflon flexible tube which is set on the connecting tube, connects the 0.5 mm wall orifice to the pressure sensor. The fixation system is illustrated in figure 4.5.

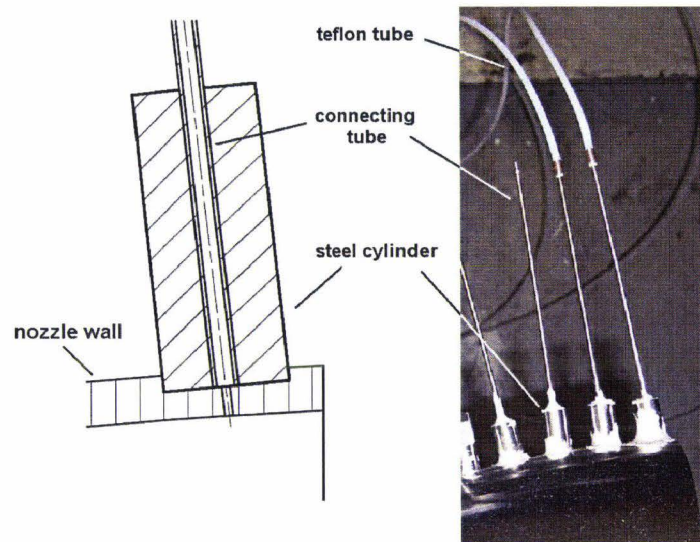


Figure 4.5: Fixation system of the wall pressure sensors on the nozzle

The disadvantage of such a system is that the signal is dephased and slightly damped by the significant distance between flow and sensor. When choosing a constant tube length for each measurement position, the signals are dephased with the same value and then comparable to each other. In steady state, the response time of the system does not need to be low and this measurement chain still leads to reliable signals.

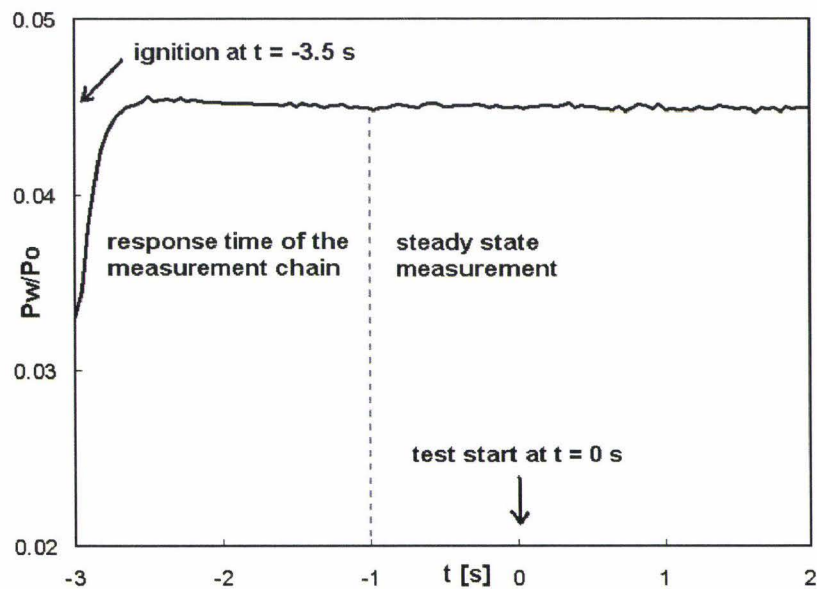


Figure 4.6: Evolution of the measured wall pressure value

The evolution of the measured pressure signal is illustrated in figure 4.6. The

time shift between the pressure variation and the signal measurement is less than the shortest test duration (of 10 s). The pressure measurements are reliable after about 2 s response time. The test starts with ignition at  $t = -3.5$  s, which means that the pressure measurements are reliable for  $t > 0$  s.

The nozzle wall is very thin in the extension and in a part of the base nozzle. The welding of the cylinder at the nozzle wall may have led to wall deformations and variations of the inner contour. In order to avoid the influence of the nozzle geometry, the cylinders were fixed at the wall using two-components ceramic glue, whose characteristics assure a good resistance to very high temperature. However, after the first hot gas tests, the ceramic began to become porous leading to disturbed pressure measurements and the leakage of the nozzle wall. A second solution had to be found in a short time. Two-components steel / epoxy resin based glue was used for the fixation. Once dry, the mixture has similar properties to steel and a temperature resistance up to 600 K. This last characteristic imposes an upper limit on the outer wall temperature which must remain below this maximum allowed temperature. The test duration thus had to be shortened and the total temperature was kept below 900 K.

#### 4.1.3.2 Temperature measurements

The nozzle wall temperature was measured using thermocouples from Electronic Sensor. The sensor type is the standard K-type, which provides a large domain of temperature measurements, between 100 K and 1450 K. The sensor sensitivity is assured up to 1.5 K or 0.4% of the temperature. The outer diameter of the chosen thermocouples is of 1 mm. The wire is made out of a nickel - chrome alloy.

The thermocouples were set at the outer nozzle wall and at various depths inside the wall thickness. Figure 4.7 illustrates the different measurement positions (pressure and temperature) on the nozzle model tested.

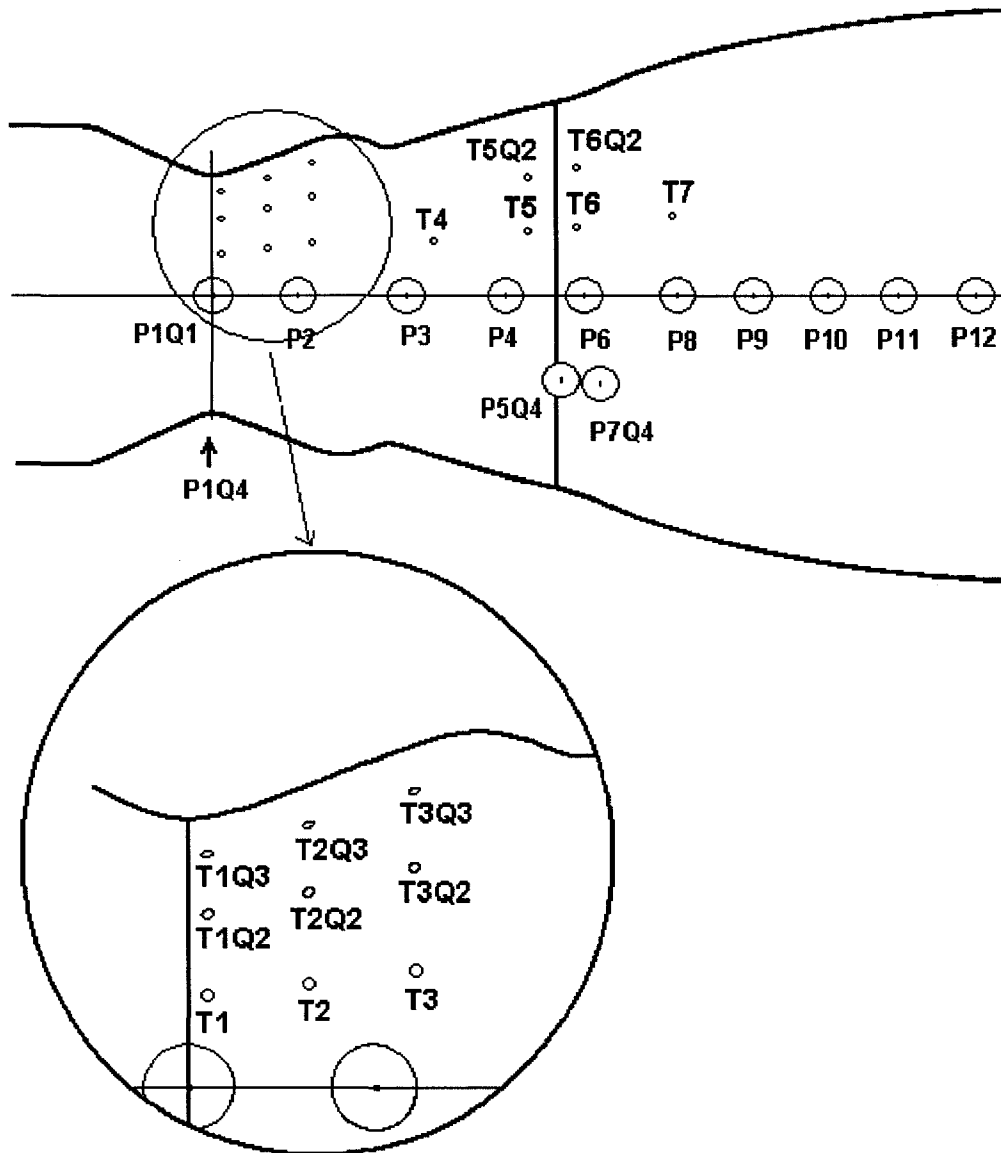


Figure 4.7: Positions of the pressure sensors and thermocouples in the nozzle wall

The position and depth of the temperature sensors were listed in table 4.3. The first number indicates the axial position of the sensor along the nozzle wall. Positions 1 to 3 are located in the thick part of the nozzle wall at three different depths. Positions 5 and 6 are placed before and after the inflection at two different depths:  $d = 3 \text{ mm}$  and  $d = 1 \text{ mm}$ , which correspond to the outer wall and inner hot wall respectively.

Designation	Axial position	Distance to hot flow $\delta$
T1	4.9 mm	1 mm
T1Q2	14.3 mm	1 mm
T1Q3	23.6 mm	1 mm
T2	4.9 mm	3 mm
T2Q2	14.3 mm	3 mm
T2Q3	23.6 mm	3 mm
T3	4.9 mm	5 mm
T3Q2	14.3 mm	5 mm
T3Q3	23.6 mm	5 mm
T4	45.4 mm	3 mm
T5	65.0 mm	3 mm
T5Q2	65.0 mm	1 mm
T6	74.8 mm	3 mm
T6Q2	74.8 mm	1 mm
T7	94.1 mm	3 mm

Table 4.3: Position of the wall temperature measurement points

The thermocouples were placed at various angular positions for a better resolution of the measurements. Sensor positions T1 to T7 are located along an axial line running from the throat down to the nozzle end. This line draws a  $20^\circ$  angle with the first pressure measurement line. Quadrants Q2 and Q3 (with an angular position of  $40^\circ$  and  $60^\circ$  respectively) allow measurements at various distances to the hot flow for a given axial position. No sensor was placed directly at the hot side of the wall because of the difficulty of sealing those positions located in the wall at its smallest thickness without damaging the sensor.

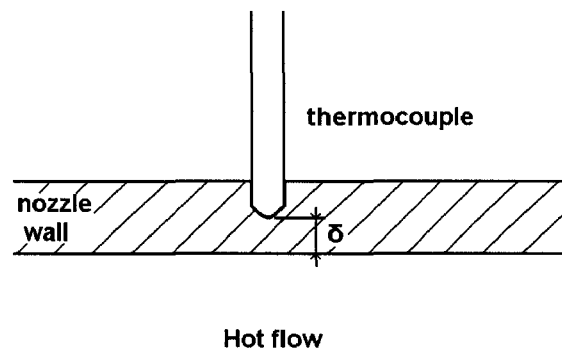


Figure 4.8: Distance  $\delta$  between thermocouple and hot inner wall

Measurements of the temperature at various distances to the hot flow aim at providing information for the calculation of the heat flux in the radial direction. The temperature at the inner wall of the nozzle can be then calculated. The positions at the outer wall can be compared to the thermal imaging and thus be used for calibration purposes. The grid of measurement points in the base nozzle should be used as reference values for a future numerical CFD study of dual bell flow. The small number of measurement channel limits the number of positions for the thermocouples.

The thermocouples were fixed to the wall with the system schematized in figure 4.9. A metal rod is screwed onto the nozzle outer wall at a given distance. The thermocouples are placed through slots in the bar and mounted at the wall with a system of spring and fixation ring. The force generated from the spring on the sensor ensures a good positioning of the sensor at the nozzle wall.

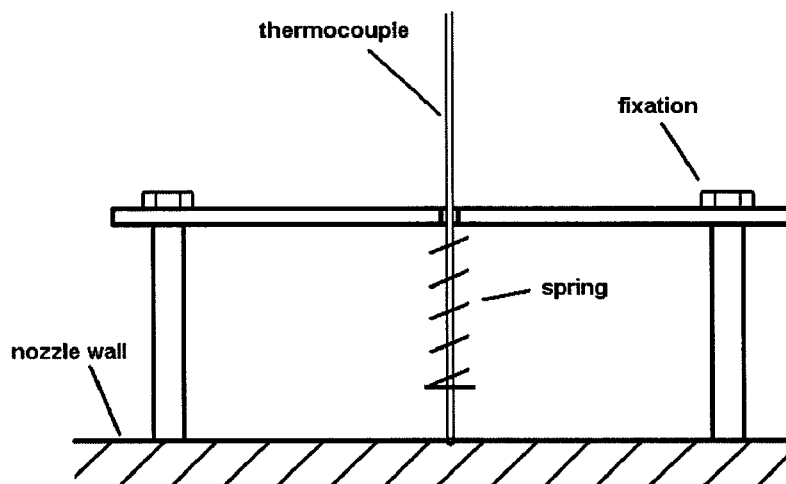


Figure 4.9: Fixation system for the thermocouples

Previous tests made at the test bench M11.4 under similar conditions have pointed out the influence of the ambient air flow on the temperature measurements at the outer nozzle wall. The ambient air is accelerated by the nozzle flow and a secondary flow is created around the nozzle. The displacement of the cold ambient air leads to a forced convection on the outer wall. The temperature measured by the surface thermocouples is then underestimated. To circumvent this effect, the thermocouples at the nozzle outer wall have to be screened from the secondary flow. Aluminium sheets were fixed on the fixation rods around the measurement positions in order to screen the thermocouples.

### 4.1.3.3 Optical system

Thermal imaging was used in addition to thermocouple measurements to investigate the temperature distribution at the nozzle wall. The measured radiation is proportional to the temperature of the object recorded with the infrared camera. Given the emissivity coefficient of the surface, the outer wall temperature can be calculated. The thermal camera in use for this test campaign was the model TI 814 from Land instruments. Its temperature range is between 253 K and 1773 K in a range of spectral domain of 8 - 14  $\mu m$ . This domain corresponds to the gap in absorption spectrum of water, so that the air humidity does not disturb the measurements. The measurement accuracy is  $\pm 2$  K or  $\pm 2\%$ . The limits of the operating conditions for the hardware are between 250 and 335 K, so that it is not possible to place the camera facing the flow. The camera is set perpendicularly to the nozzle axis, pointing at the nozzle outer wall.

The nozzle wall facing the camera is painted with matt black paint to increase the coefficient of emissivity (of about 0.97). This coefficient can be implemented in the camera software to fit the test conditions.

### 4.1.4 Test sequence

The test bench M11.4 chosen for the warm gas investigation of dual bell nozzles features steady flow conditions. The operating pressure and temperature are set through the air, oxygen and hydrogen mass flows. The H<sub>2</sub>/O<sub>2</sub> burners heat up the pressured air. The test sequence is typically as follows:

- $t = -5$  s Start of cold air flow. The pressure increases to about half of its nominal value. The temperature measured in the nozzle drops due to the cold flow.
- $t = -3.5$  s Burners ignition. The burners bring the flow to the operating conditions. The flow temperature increases rapidly up to its maximal value.
- $t = 0$  s Test start. The operating conditions (pressure and temperature) are reached.

- $t = t_{end}$  Test end ( $t_{end} = 20$  s in the example of fig. 4.10). The installation is shut down, flow temperature and pressure drop rapidly.

The installation is purged with nitrogen directly after shut down of hydrogen and oxygen flows. The pressure value features a peak before it drops. The temperature decreases very rapidly.

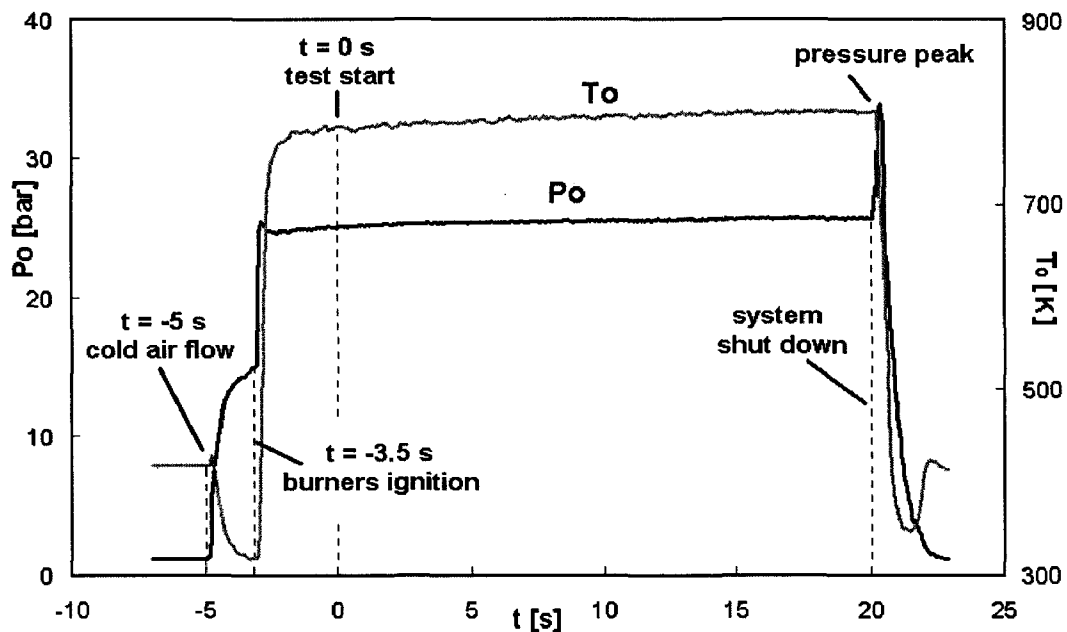


Figure 4.10: Typical test sequence at M11 test bench

The start up and shut down of the installation both lead to a pressure peak, as seen in figure 4.10. The measured amplitude may be underestimated because of the low sampling rate of the measurement system. The start up peak is very low (the order of magnitude of 1 bar or 5% of the nominal total pressure) and should not disturb the flow behaviour. The measured amplitude of the shut down peak is about 35% of the nominal total pressure.

The objective of the study was to test a range of temperature and pressure to investigate the influence of the flow properties on the dual bell flow behaviour. The fixation system for the pressure measurements imposes an outer wall temperature lower than 600 K, which fixes the total temperature maximum to about 900 K for a test duration of under 20 s. The range of temperatures investigated is between 750 and 900 K, for a pressure variation between 15 and 30 bar. The test duration was

chosen between 10 and 20 s. The first tests of a series were limited to 10 s in order to bring the system to a higher start temperature.

## 4.2 Flow behaviour under hot gas conditions

The wall pressure measurements have two objectives: to verify under hot gas conditions the flow behaviour conclusions obtained from the first part of this study and to determine the flow mode corresponding to the temperature measurements. The flow behaviour under various temperature and pressure conditions is presented in this section.

### 4.2.1 Pressure distribution

The pressure measurements were made along the nozzle wall for various test conditions.

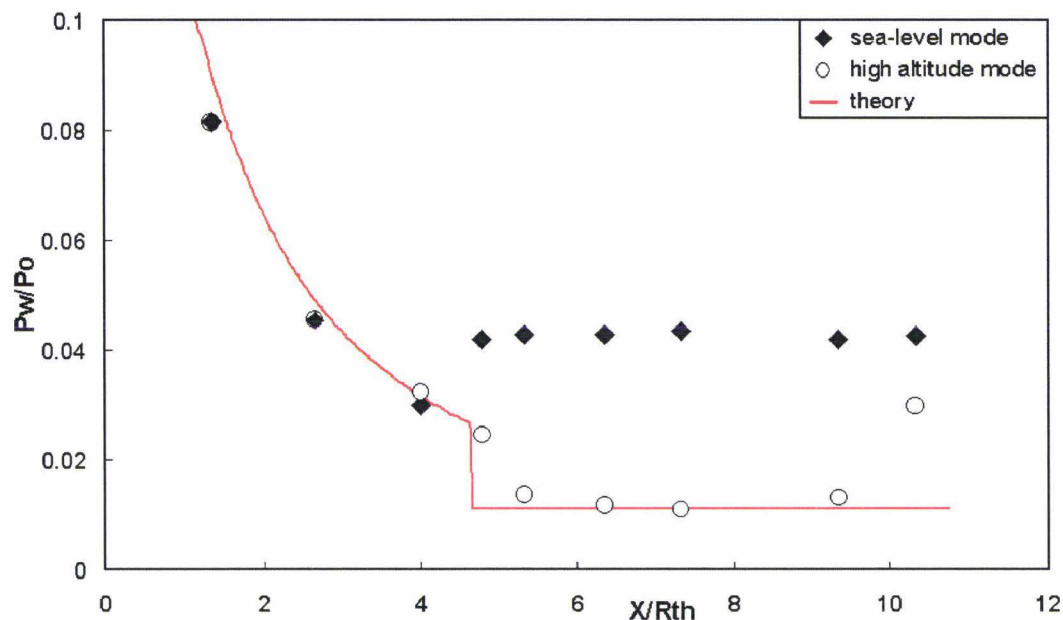


Figure 4.11: Pressure distribution under sea level and high altitude mode

Figure 4.11 illustrates the wall pressure distribution under the sea level and high altitude modes. The theoretical pressure distribution, calculated with the method of characteristics for the flow properties in the test conditions, is presented for comparison purposes.

In the base nozzle, the measured pressure values under the sea level and high altitude modes show a good accordance to each other and to the theory. The experimental pressures are slightly lower than the theoretical values, probably due to the varia-

tions of the nozzle contour geometry under the hot gas conditions.

In sea level mode, the wall pressure distribution in the extension corresponds to the pressure of the recirculating flow ( $\simeq 0.9P_a$ ), as seen for the cold flow tests. The high altitude mode is characterized by lower wall pressure values due to the presence of the high expanded flow at the wall. The pressure decreases from the inflection point down to the end of the inflection region ( $x/R_{th} \simeq 5.5$ ). The pressure distribution in the constant pressure part of the extension matches the theoretical calculated value. The last measurement point indicates a higher pressure at the nozzle end. This is due to the nozzle end effect (incipient separation [58]).

The pressure distribution corresponds to the results obtained for cold flow test conditions. The steady test conditions make the sneak transition difficult to detect, but the negative pressure gradient in the inflection region indicates a high probability of this flow evolution.

## 4.2.2 Transition conditions

The operating flow mode of the dual bell nozzle is identified by the wall pressure measured in the extension. Under steady state test conditions, the exact transition NPR cannot be directly measured: if the flow is under sea level mode,  $NPR_{trans}$  is not yet reached and if the flow is under high altitude mode, the  $NPR_{trans}$  value is already exceeded.

The flow mode (sea level or high altitude) is recorded for the various conditions of total temperature and pressure of all the conducted tests. The transition condition can be approximated by reducing the range of possible  $NPR_{trans}$ . A scatter plot of various test conditions leads to a good estimation of the transition NPR (see figure 4.12).

The start up and the shut down of the installation present a pressure peak that may also lead to flow transition to high altitude mode. The peak amplitude at start up (at  $t = -3.5$  s) is very low and corresponds to the nominal pressure value attained during the test (for  $t \geq 0$  s). The shut down peak is high and generally leads to flow transition even if the steady state NPR does not lead to transition.

Figure 4.12 depicts the flow mode as a function of the NPR and the total temperature. When no transition takes place, the nozzle flow is under sea level mode and the

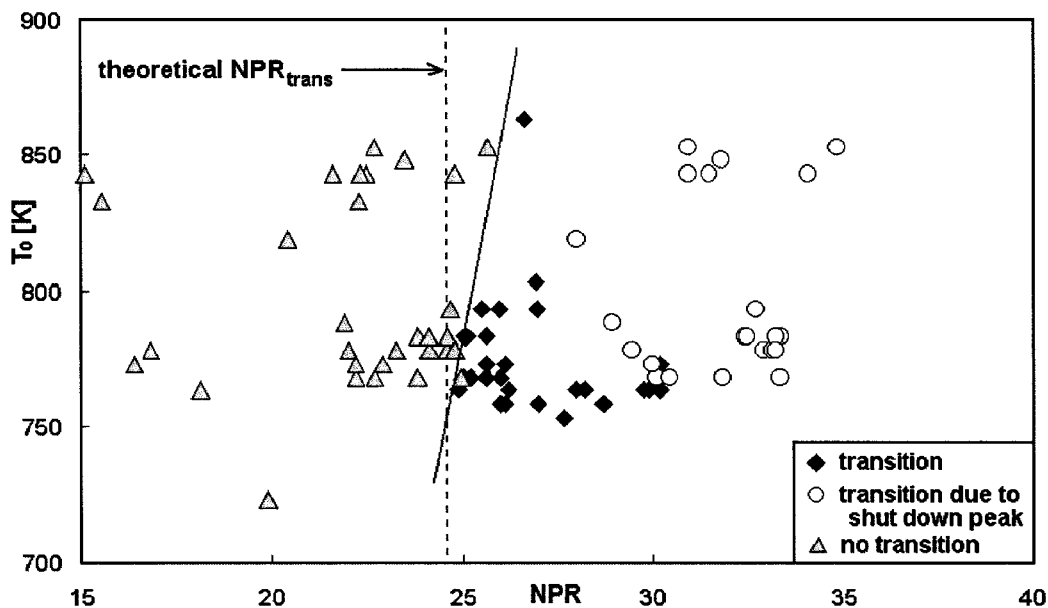


Figure 4.12: Transition conditions as a function of the total temperature

transition NPR is not exceeded. High altitude mode can be reached either at the operating conditions or during the shut down pressure peak. The transition  $NPR_{trans}$  value is in the vicinity of the boundary between the regions of  $NPR_{sea-level}$  and  $NPR_{high-altitude}$ .

The steady state and the shut down peak values of the NPR are presented for every test conducted in this study. The transition NPR value is approximated with a straight line running between the two flow conditions. The theoretical value of  $NPR_{trans}$  is presented for comparison. The transition NPR shows a dependency on the total temperature value. Transition occurs for a higher pressure ratio for increasing flow temperature values.

The variation of the transition conditions may be a consequence of variations in the structure geometry. Flow temperature variations induce deformations of the thin nozzle wall. The hot wall dilates under high temperature flow conditions and the cross section increases. Figure 4.13 schematizes the geometry variation under high temperature. The base nozzle become warmer than the extension, so that the deformations of the base geometry are more significant than the ones of the extension: the base nozzle bulges. The inflection point is cooler and thus more rigid against cross section variation, acting like a bracing ring for the structure. The inflection angle of the dual bell nozzle increases with the hot temperature flow. As presented

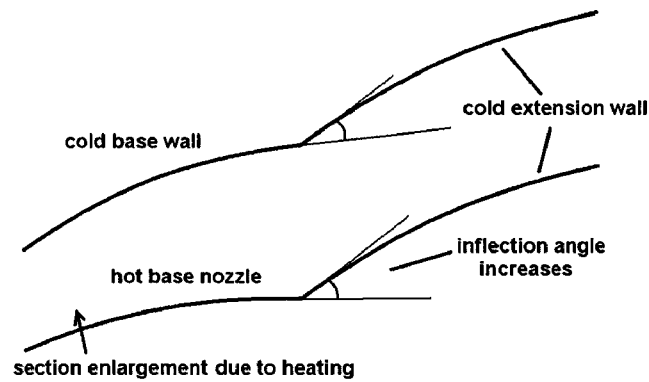


Figure 4.13: Nozzle geometry variation under hot flow conditions

in previous sections, the value of transition NPR increases with the angle  $\alpha$ . As a consequence, the total temperature increase delays the transition points of the dual bell nozzle.

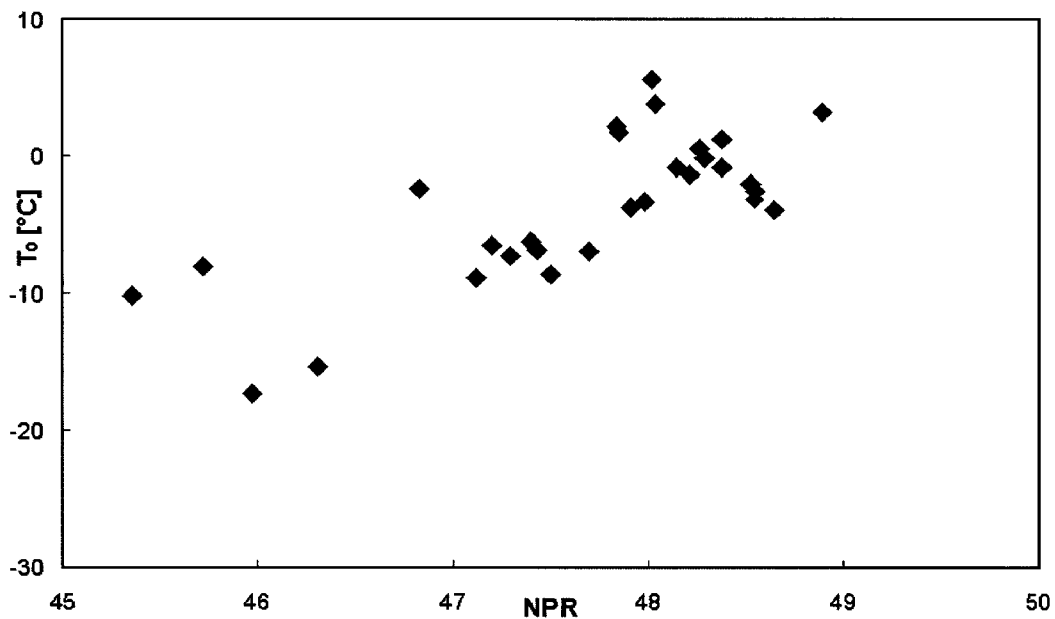


Figure 4.14: Transition NPR as a function of the temperature in cold flow conditions

The influence of the temperature on transition conditions had already been noticed in cold flow tests on dual bell nozzle models. In figure 4.14 the transition NPR is plotted as a function of the total temperature for a series of tests conducted under cold flow condition at test bench P6.2. A small aluminium dual bell nozzle was investigated under conditions comparable to those presented in the first part of this

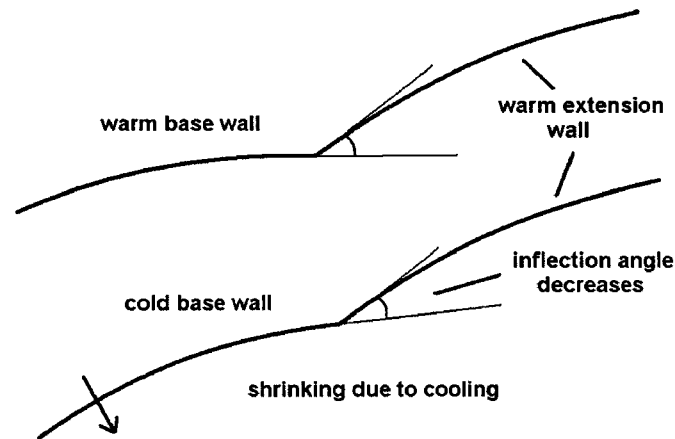


Figure 4.15: Nozzle geometry variation under cold flow conditions

study. The aluminium used for the nozzle contour presents a higher thermal conductivity than acrylic glass. Furthermore, the test duration for the cold flow campaign was much higher than the one for the present study. During sea level mode, the cold flow had enough time to cool down the base nozzle wall. The metal contraction leads to a decrease of the section in the base nozzle (see fig. 4.15). With a temperature decrease, the inflection angle  $\alpha$  decreases and the transition takes place for lower values of the NPR. This effect confirms the trend measured at the test bench M11 under hot gas conditions.

A steady state flow study does not yield any information on the retransition NPR. The system shut down is very fast and the low measurement sampling rate does not enable to record the wall extension pressure drop. The installation is not yet adapted for the investigation of the hysteresis effect between transition and retransition conditions and modifications of the tests bench would have to be made before conducting further tests.

### 4.2.3 Conclusion

The transition conditions observed for cold flow operation are partially verified under hot flow conditions. The temperature of the flow influences the transition conditions:  $NPR_{trans}$  increases with the total temperature of the flow.

This effect should be further investigated because the nozzle wall cooling may lead to a comparable effect. The wall temperature decrease in the vicinity of the wall could induce slight geometry variations and shift the transition NPR, and with it

the transition altitude.

A model of the structural deformations of the wall should allow the improvement of the transition prediction model for higher temperatures.

### 4.3 Thermal behaviour

The nozzle model instrumentation allowed a maximum test duration of about 20 s under a total temperature  $T_0 \simeq 900 \text{ K}$ . This duration ensures that the outer wall temperature does not exceed the limit temperature of 600 K. This test duration was insufficient to reach steady conditions, so that reliable temperature measurements were difficult to conduct for this test campaign. The last test of the campaign was conducted until the structure collapsed, that is for  $t = 40 \text{ s}$ . The measurements made during this test yield information for the analysis of the shorter tests and are used as a reference.

#### 4.3.1 Response time of the system

The response time of a semi-infinite wall to a temperature step on its surface is representative of the response of the actual system as long as the temperature wave does not reach the opposite wall surface. In the hypothesis of a one dimensional problem, the temperature response as a function of time is given by the following equation:

$$\frac{T(x, t) - T_0}{T_1 - T_0} = \operatorname{erf}\left(\frac{x}{2\sqrt{at}}\right) \quad (4.1)$$

The characteristic length  $x$  represents the wall thickness ( $x = 3 \text{ mm}$ ). The thermal diffusivity,  $a$ , is the ratio of thermal conductivity to volumetric heat capacity and corresponds to the velocity of a thermal wave in a given medium.

$$a = \frac{k}{\rho c} \quad (4.2)$$

with  $c$  the thermal capacity of the material ( $c = 510 \text{ J/kg.K}$  for steel),  $\rho$  the density and  $k$  the thermal conductivity. In this case, the value of  $a$  is  $a = 4.2 \cdot 10^{-2} \text{ m}^2/\text{s}$ .

The response time at 80% of the system corresponds to a value of  $\operatorname{erf}(x/2\sqrt{at}) = 0.8$ . This condition is reached when  $x/2\sqrt{at} \simeq 0.9$ . The value of  $t$  for a temperature response at 80% is of about 0.7 s. This means that the nozzle wall responds to a flow temperature variation within  $t \simeq 0.7 \text{ s}$ .

The test conditions do not provide steady state temperature conditions, but the fast response time of the system assures the representativeness of the temperature

measurements made in this test campaign (with a test duration between 10 and 40 s).

### 4.3.2 Temperature distribution

The evolution of the wall temperature measurements is given in figure 4.16 for the last test configuration (test duration is 40 s). The nozzle flow is under high altitude mode: the hot flow attaches to the wall down to the nozzle end. The measurements presented in figure 4.16 correspond to sensors located in the thin part of the nozzle wall. Positions T4 to T7 are located at the surface of the outer wall, at 3 mm from the hot inner wall. Positions T5Q2 and T6Q2 are placed inside the wall, at 1 mm from the hot wall.

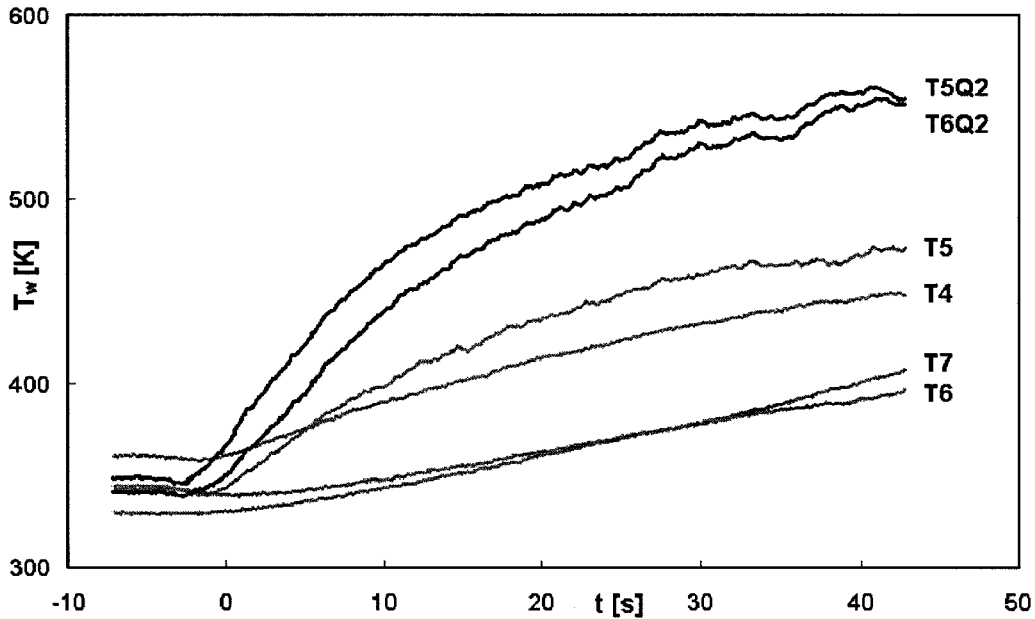


Figure 4.16: Evolution of the temperature at different positions along the nozzle wall measured at 3 mm (T4 to T7) and 1 mm (T5Q2 and T6Q2) from the hot flow

The temperature evolution obtained for the 40 s test was compared to those resulting from the shorter test performed under high altitude mode conditions and was found to be representative of all the shorter tests. The start temperature varies from one test to the other, but the evolution is the same for the various configurations. The measurements obtained with the longer reference test can be generalized to all the other tests conducted under high altitude mode.

The thermocouples at the positions T5, T5Q2 and T6Q2 show a realistic evolution of the temperature value. The evolution starts with the beginning of the test and shows an asymptotic evolution towards the test end. The measurements at positions T4, T6 and T7 indicate a very slow reaction of the temperature variation. The values recorded are also lower than expected. A flow phenomenon may be responsible for this evolution at measurement point T6 and T7 in the extension. In case of a separation bubble at the wall, the response time of the temperature evolution in the wall would be slower. However, the evolution of the temperature measurement at position T4 in the base nozzle cannot be explained with a flow phenomenon. The thermocouple probably moved from its initial position and the measurements do not correspond to the actual wall temperature.

The temperature distribution along the nozzle is given in figure 4.18 for the two operating modes: sea level and high altitude mode. The values recorded were obtained from two comparable tests: which had the same total temperature  $T_0$  value and the same duration (20 s) but a different value of the total pressure  $P_0$ , inducing different flow operating modes. The tests were conducted at the end of a series of short tests (10 s), which brought the start wall temperature to a comparable value and hence led to end wall temperatures near the steady state conditions. The measurements are made at a distance of 3 mm to the hot flow, which means in the wall for sensors T1 to T3 and at the outer wall for the sensors T4 to T7 (see figure 4.17).

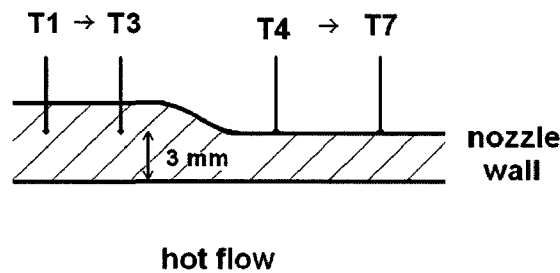


Figure 4.17: Position of the thermocouples T1 to T7 in the nozzle wall

The temperature distribution in the base nozzle is similar for both operating modes. The measured temperature decreases from the throat to the base nozzle end (the measurement point T4, at  $x/R_{th} = 3$  is presented for comparison purposes only) .

At the measurement positions T5, T6 and T7, the temperature difference between sea level and high altitude modes is in range of  $0.1 * T_w/T_0$ . The wall temperature

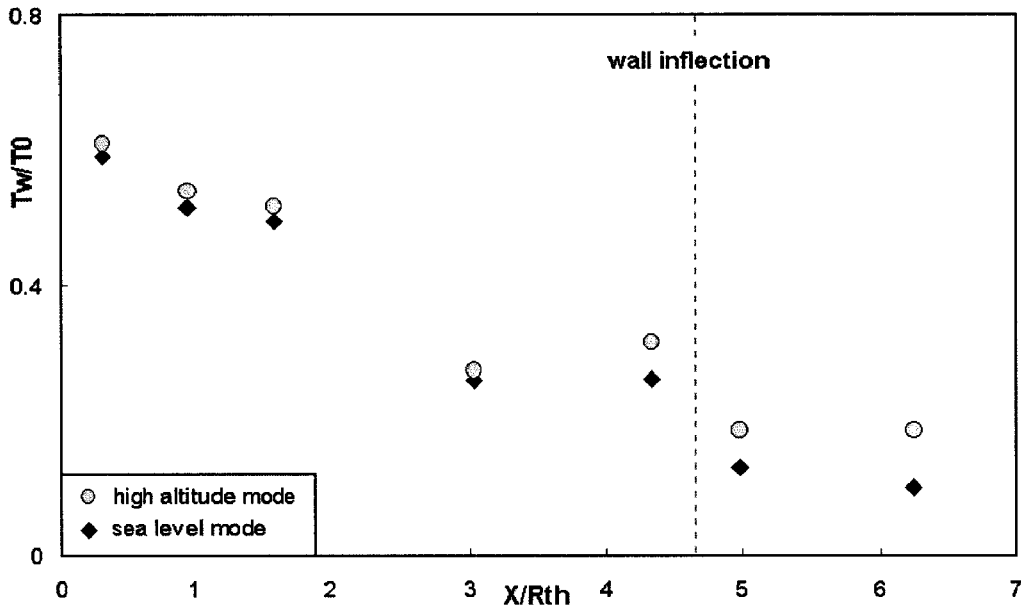


Figure 4.18: Temperature distribution along the nozzle wall measured using thermocouples placed at 3 mm from the hot flow wall side

values recorded in the extension are lower than the temperatures measured at the base wall. Under sea level conditions, the temperature slightly decreases along the extension. The wall is in contact only with the recirculating air, which is heated up by the nozzle flow. Under high altitude mode, the temperature distribution is constant along the extension wall, as expected with a CP extension contour.

The poor resolution of the temperature distribution at the nozzle wall should be increased in future test campaigns with additional measurement positions. In particular, the region up- and downstream of the inflection are of great interest due to the higher temperatures measured in this study.

### 4.3.3 Thermography

Thermography was used to obtain a better resolution of the temperature distribution at the nozzle wall. The region of thin wall thickness, where the thermal imaging was used, corresponds to the second part of the base nozzle and the extension nozzle. The camera was directed on the nozzle wall side painted with matt black colour. The temperature distribution was both recorded as single pictures taken at chosen instants of the test and as thermal films.

#### 4.3.3.1 Thermal images

The thermal imaging camera provides the possibility of recording films or single pictures of the outer nozzle wall. The storage time for a picture is 3 s during which no image is available for the film (black screen during the recording). Single pictures can be processed directly using the camera's software LIPS 814 to obtain the temperature corresponding to each pixel. It was decided to take one picture for each test, at the last instant before the burners shut down.

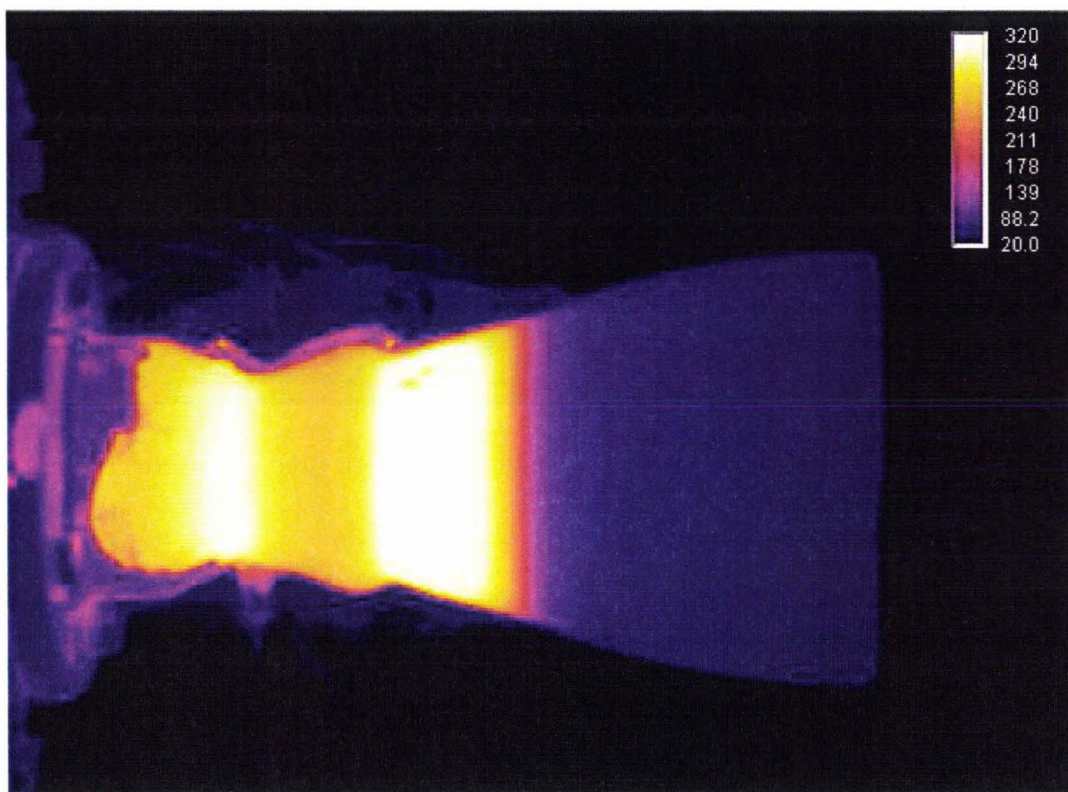


Figure 4.19: Thermal imaging of the nozzle under sea level mode (temperature scale given in °C)

The two thermal pictures in figure 4.19 and 4.20 were taken at the end of two comparable tests under sea level and high altitude conditions. The test duration was in both cases 20 s, which is the longest possible duration available for both operating modes under the conditions obtained in this study. The tests were conducted at the end of a series of tests which were performed in order to warm up the installation

and approach thermal stationary condition.

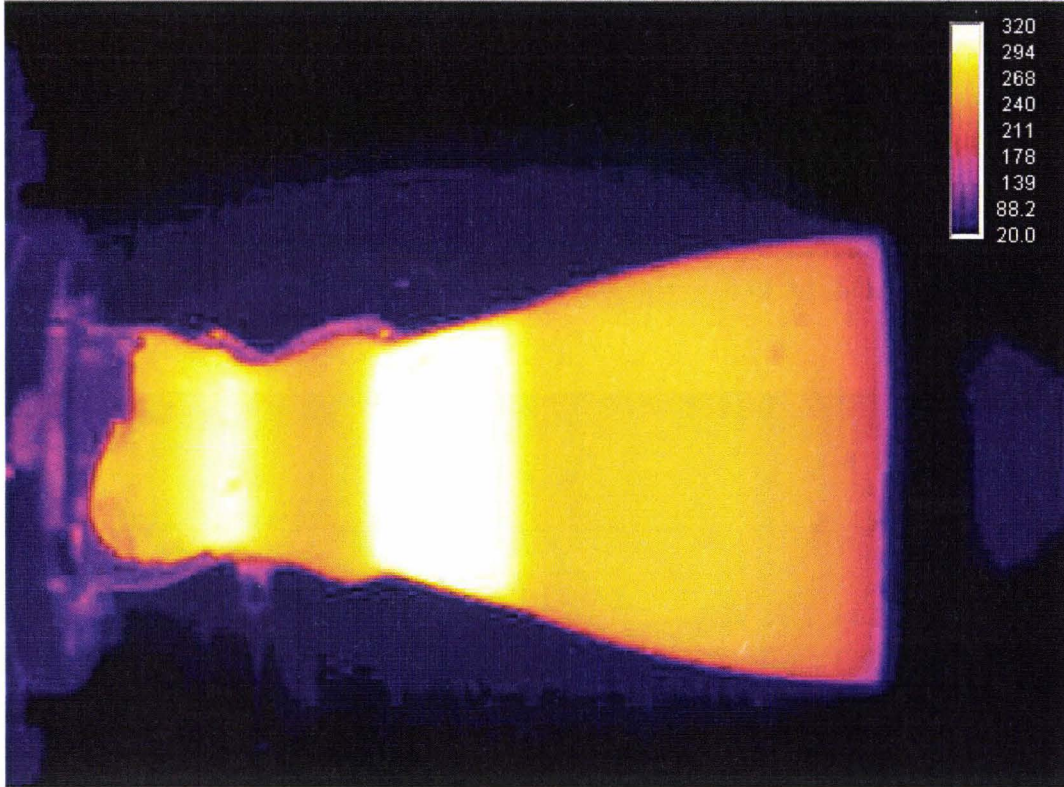


Figure 4.20: Thermal imaging of the nozzle under high altitude mode (temperature scale given in °C)

The nozzle wall is particularly hot in the throat area, where the thermal loads are the highest. The temperature decreases in the base nozzle. The passage from thick wall to the thin part of the wall is characterized by a rapid increase of the outer wall temperature under both operating modes. The extension wall is comparatively cold (about 420 K) under sea level mode.

The camera image processing software LIPS 814 provides the temperature for every pixel of the picture. The emissivity coefficient can also be set for each position (here  $\epsilon = 0.97$ ). The measured points are taken at the nozzle wall along the axis. The temperatures are recorded only in the thin part of the nozzle wall in order to keep a constant distance to the hot flow. Figure 4.21 represents the outer wall temperature at various positions taken along the nozzle wall, under both sea level and high altitude modes.

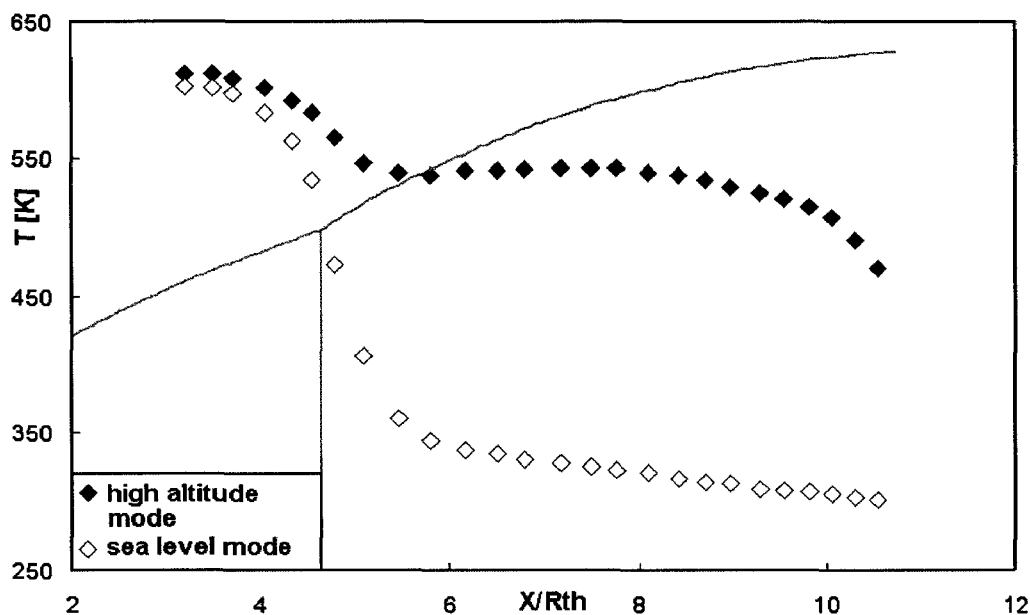


Figure 4.21: Wall temperature distribution under sea level and high altitude mode, measured using thermal imaging

The temperature measurements are extracted from the tests illustrated in the infrared pictures 4.19 and 4.20. The outer wall temperature in the base nozzle is comparable under both flow modes. Under sea level mode, the temperature decreases along the wall. A region around the inflection with a width of about  $2.x/R_{th}$  presents a fast decrease of the temperature. The recirculating ambient air leads to a low temperature at the nozzle wall in the extension. The temperature is higher in the vicinity of the inflection because of the axial thermal flux in the wall. At the nozzle end, the measured temperature almost corresponds to the ambient temperature. The nozzle wall temperature is almost constant in the extension under high altitude mode and decreases at the nozzle end.

The inflection region has to be taken into account for the design of the cooling system for dual bell nozzle. The temperature of the nozzle wall in this region is comparable to the temperature in the base nozzle under both operating modes.

#### 4.3.3.2 Analysis of the thermal movies

The pictures taken with the camera software are precise and easy to analyse but they yield information for only one instant of the test. In order to investigate the

evolution of the temperature at the nozzle wall, the thermal films are also analysed. As no software is available for the data extraction of the film, a program written with MATLAB was used. For each frame of the film, a series of points located on the nozzle axis are recorded. The pixel colour is then compared to the legend bar. This method is not as precise as the picture analysis. An additional error factor of about 5 K must be taken into account, for a global precision of the order of  $\pm 10$  K on the measured temperature.

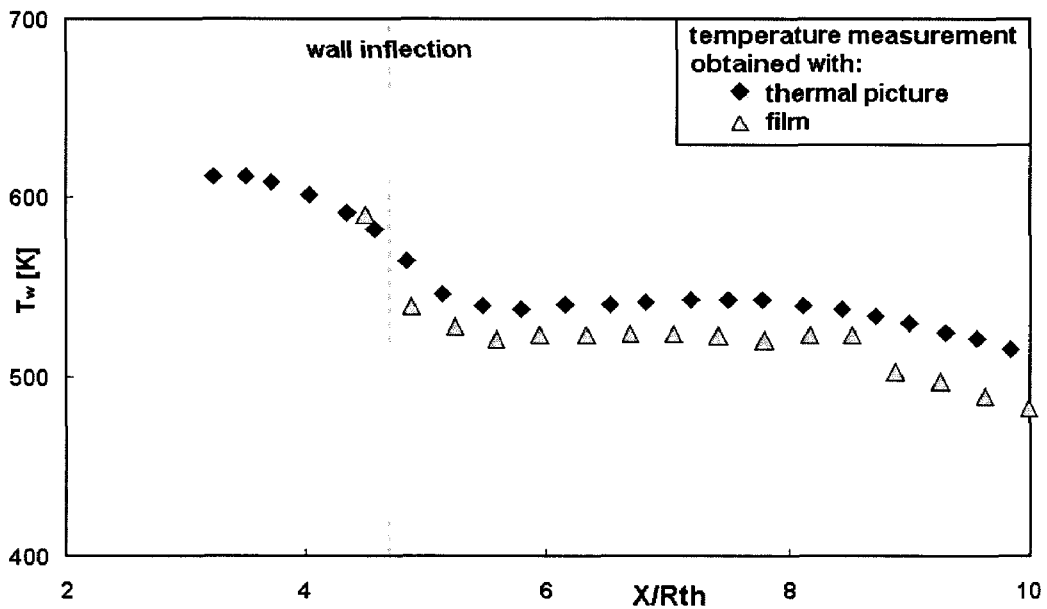


Figure 4.22: Comparison of outer wall temperature under high altitude mode measured with infrared pictures and film under high altitude mode

Figure 4.22 represents the distribution of the outer wall temperature along the nozzle axis obtained from a thermal image and from the thermal film. The temperature is slightly underestimated with the film measurement. However, the two methods show similar results and the values extracted from the film analysis can be considered as reliable.

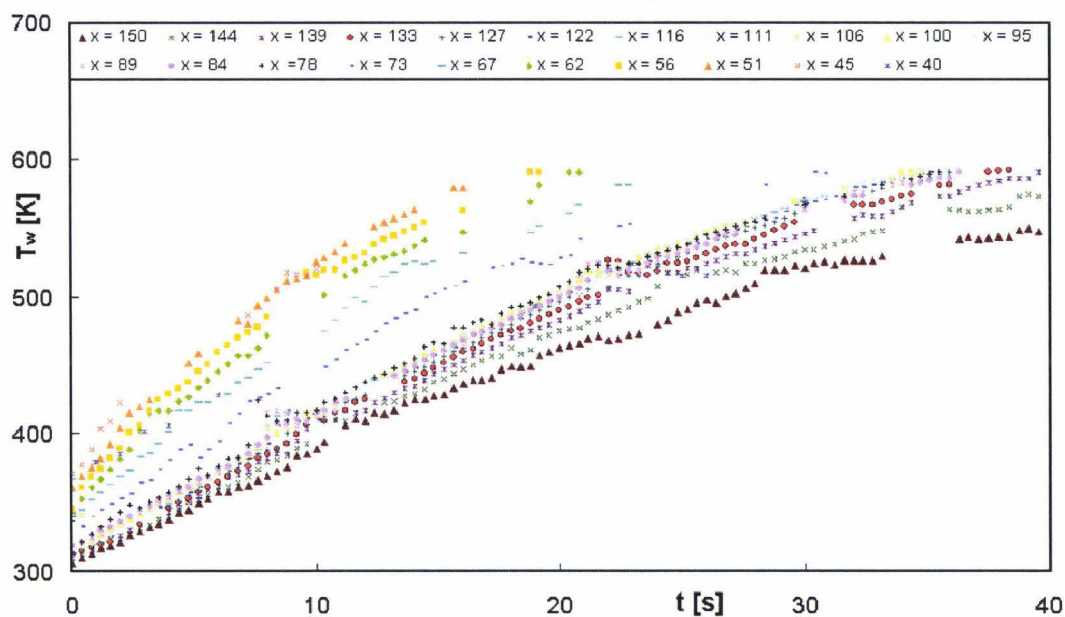


Figure 4.23: Evolution of the outer wall temperature for various positions in the nozzle

The temperature evolution is presented in figure 4.23 for the longest test at various positions along the nozzle outer wall. The scale given in the film provides a poor resolution in the upper temperature range. For this reason, values above 600 K are not presented in this figure. The thermal film yields only reliable information for temperatures below this limit.

Figure 4.24 illustrates the temperature distribution at the nozzle wall for seven instants during the test. For the same reason as mentioned above, no temperatures are given over 600 K. The measurements in the base nozzle are not available for instants after  $t = 10$  s. The nozzle flow is attached in the extension; the nozzle is under high altitude mode. The temperature in the base nozzle decreases along the wall.

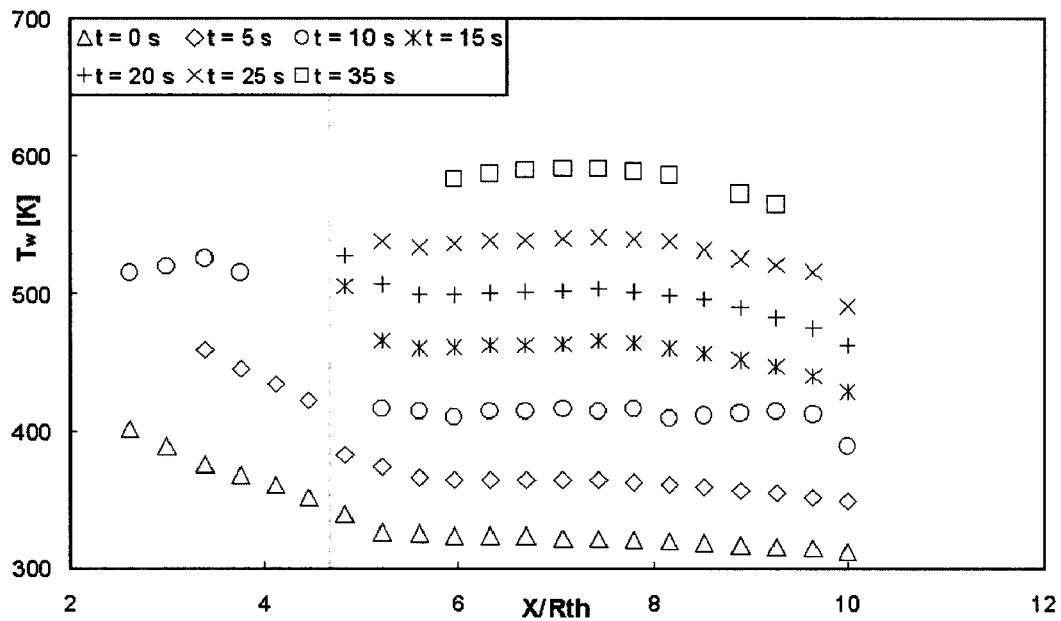


Figure 4.24: Temperature distribution at the nozzle outer wall at various instants of the test under high altitude mode

In the extension, the wall temperature is thus almost constant. At the end of the extension, lower temperatures are measured due to the flow end effect. The circulation of the ambient air around the nozzle induces a cooling of the nozzle extremity.

#### 4.3.3.3 Conclusion

Outer wall temperature values for thermal imaging and thermocouple measurements (sensors T4 to T7 at the outer wall) under high altitude mode are presented in figure 4.25. The temperature values measured with the thermocouples have all shown a significant discrepancy with the thermal imaging. The difference between the measured values is as much as 200 K for the same axial position. The first position (T4) has already been eliminated as non physical. Positions T5 to T7 however present also significant temperature differences with the thermal imaging measurements.

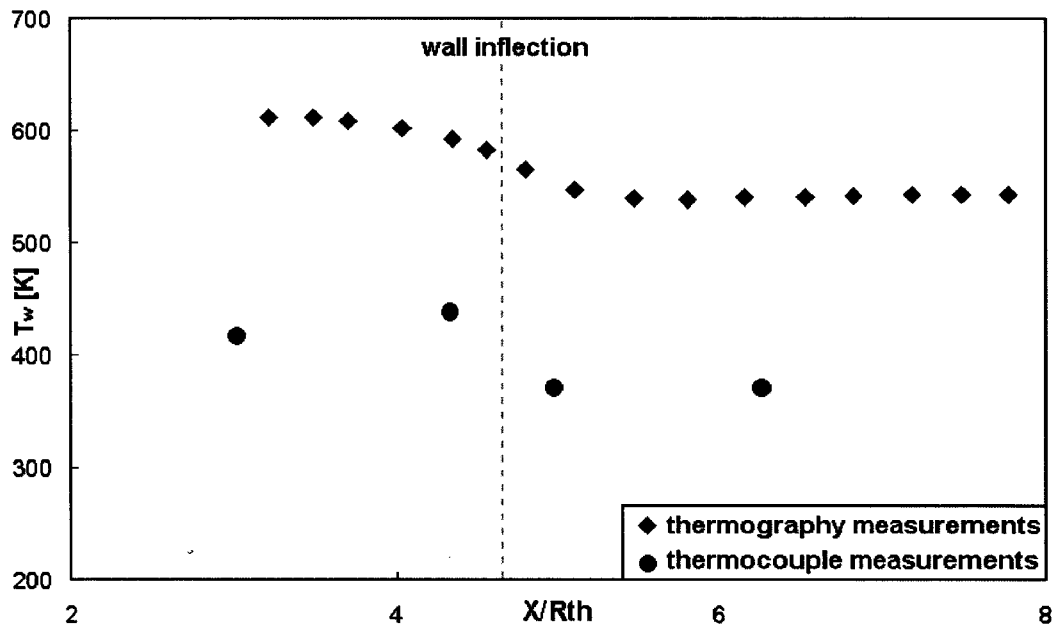


Figure 4.25: Comparison of the outer wall temperature measured with thermal imaging and thermocouples (positions T4 to T7)

The measurements taken at positions T6 and T7 were already discussed in the previous section. The thermal imaging has shown that the evolution recorded in the extension with the thermocouples is not a physical effect, but a measurement error. The thermocouples may have moved from their position at the wall due to vibration of the nozzle.

Although the temperature evolution measured at the position T5 is coherent, the values recorded show a significant discrepancy with the thermal imaging. A coefficient of 2.5 can be found between the thermocouple measurements at T5 and the thermography at the same axial position, as shown in figure 4.26. The signals present then a very good agreement for the two measurement methods. The error in the thermocouple signals may come from a problem in the measurement channel.

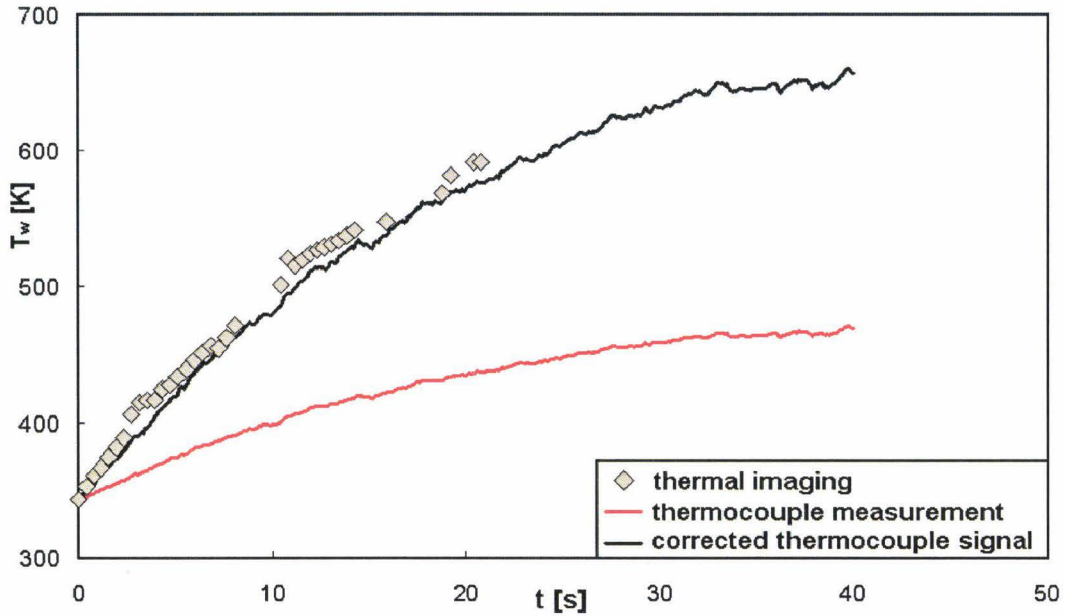


Figure 4.26: Correction coefficient of the thermocouple signal for the position T5

All the measurements made at the outer wall of the nozzle with thermocouple present errors. Only the value obtained for the sensor inside the wall (positions T5Q2 and T6Q2 for the thin part of the nozzle wall) should be used.

### 4.3.4 Inner wall temperature

Temperature measurements yield only information about the temperature at the outer nozzle wall (thermography) or inside the wall (thermocouples). The inner wall temperature can be calculated using various methods.

#### 4.3.4.1 Recovery temperature

The recovery temperature is a first approximation of the temperature along the inner hot wall of the nozzle. The Mach number value of the flow at the wall is calculated from the pressure measurements. The flow temperature ( $T_E$  at the edge of the boundary layer) is calculated using the isentropic relations. The wall temperature  $T_w$  is then:

$$T_w = T_E \cdot \left(1 + \frac{\gamma - 1}{2} M^2 \cdot r\right) \quad (4.3)$$

with the coefficient  $r$  calculated as:

$$r = Pr^{1/3} \quad (4.4)$$

$Pr$  is the Prandtl number and is a function of the flow properties:

$$Pr = \frac{c_p \mu}{k} \quad (4.5)$$

with  $c_p$  specific heat,  $\mu$  viscosity ( $\sim 36.10^{-6} Pa.s$  for air at 800 K) and  $k = 19 W/m.K$  thermal conductivity. For gas, the Prandtl number is approximated with the value  $Pr = 0.7$ .

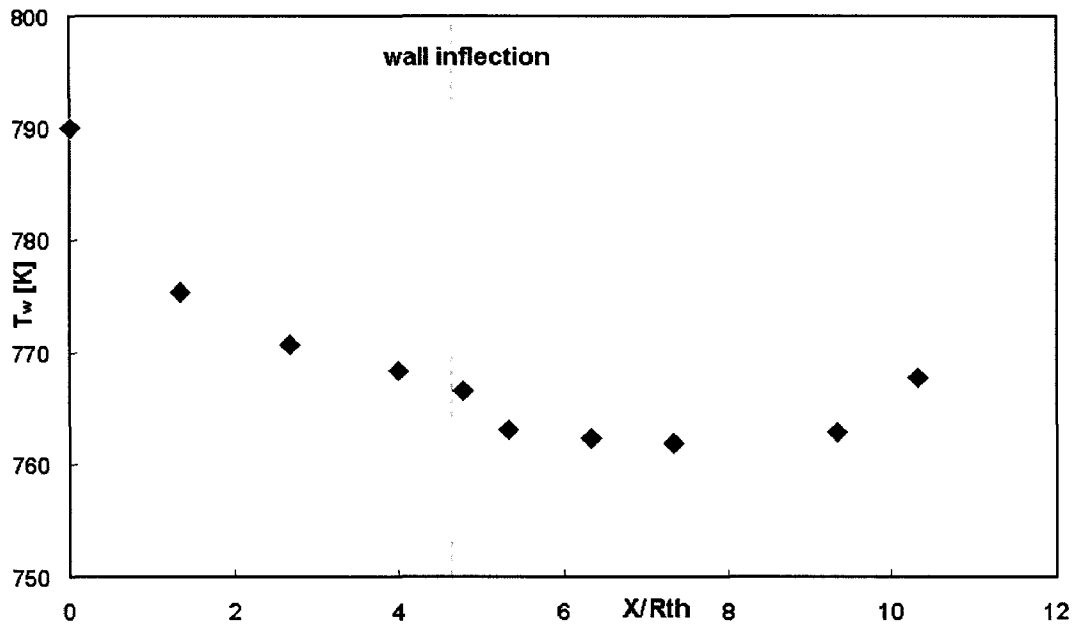


Figure 4.27: Distribution of the recovery temperature

The recovery wall temperature has been calculated along the nozzle wall using the pressure measurement. The distribution of  $T_w$  is presented in figure 4.27. The distribution is comparable to the pressure distribution presented in figure 4.11. The wall temperature decreases along the base nozzle wall, drops over the inflection region and is then constant in the constant pressure region of the extension.

The higher value of the wall temperature indicated at the nozzle end is not physical. The boundary layer thickness increases at the nozzle end, increasing the value of

the wall pressure value. In this region, the recovery temperature equation cannot be applied. In fact, increased thickness of the boundary layer leads to a slight re-compression of the flow and to higher values of the temperature at the nozzle end.

#### 4.3.4.2 Temperature variation in the wall thickness

A wall placed under a temperature variation is said thin if the Biot number is less than 1 (usually  $Bi < 0.1$ ). It represents the ratio of the resistance to heat transfer in the wall through the convection. The nozzle wall has been chosen of 3 mm in the extension and in the second part of the base in order to facilitate the thermography measurements from the outside of the nozzle. The Biot number can be calculated as follows:

$$Bi = \frac{h.L}{k} \quad (4.6)$$

where  $k$  is the thermal diffusivity of the material and  $L$  a characteristic length, here  $L = e = 3 \text{ mm}$ , nozzle wall thickness. The variable  $h$  is the heat transfer coefficient. It can be calculated on the external nozzle face in natural convection out of the Nusselt number with the following relation:

$$Nu = A(Gr.Pr)^m = \frac{h.D}{\lambda} \quad (4.7)$$

The Nusselt number is the ratio of convective to conductive heat transfer across a boundary. To simplify the problem, the nozzle can be approximated with a cylinder with a mean diameter of  $D = 10 \text{ mm}$ . The inner temperature is assumed constant and taken to be 750 K (recovery temperature) and the outer temperature is about 300 K. The variable  $\lambda$  is the thermal conductivity coefficient of the air at the film temperature. The coefficients  $A$  and  $m$  are defined by the flow characteristics: laminar or turbulent. This state is given by the value of the product  $Gr.Pr = Ra$ , Rayleigh number of the system. The Rayleigh number defines the predominance between conduction and convection.

$$Ra = \frac{g\beta\Delta TL^3}{\nu a} \quad (4.8)$$

with  $\beta$  the thermal expansion coefficient,  $\nu$  the kinematic viscosity and  $a$  thermal diffusivity. In the approximation made for this study, the Rayleigh number is in the order of  $Ra \simeq 2.8 * 10^6$ , which indicates a laminar behaviour (convection as

predominant heat). The Nusselt number can be then calculated with the following coefficients:  $A = 0.53$  and  $m = 0.25$ . We obtain then:

$$Nu = 0.53(2.8 * 10^6)^{0.25} = 21.6 = \frac{h \cdot D}{\lambda} \quad (4.9)$$

The value of the heat transfer coefficient results in  $h = 8.7W/m^2K$ . When applying this value to equation (4.6), the Biot number is calculated as:

$$Bi = 8.73 * 10^{-3} = 1.5 * 10^{-3} \quad (4.10)$$

The Biot number value is lower than 0.1, so that the nozzle wall can be considered to be thin in the second part of the base and in the extension. The wall temperature can be approximated as constant over the wall thickness.

Figure 4.28 illustrates the wall temperature measured at the outer wall using thermal imaging and temperature measured with thermocouples inside the wall (at 1 mm from the hot wall). The measurements obtained using these two methods are in very good agreement. The approximation of a constant temperature is confirmed by the experimental values.

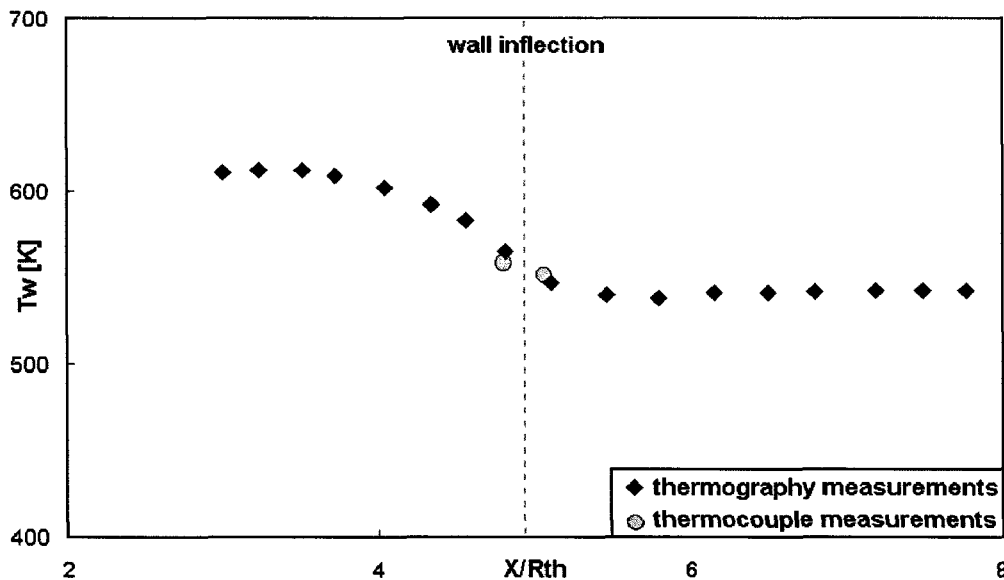


Figure 4.28: Comparison of the outer wall temperature measured with thermal imaging and thermocouples (positions T5Q2 and T6Q2)

The recovery temperature can be compared to the values measured in the wall. Figure 4.29 is a comparison of the recovery temperature and the wall temperature measured with two methods. The recovery temperature is based on adiabatic relations and represents the upper limit of the inner wall temperature in steady state conditions. The wall temperatures are underestimated because of the unsteady measurement conditions.

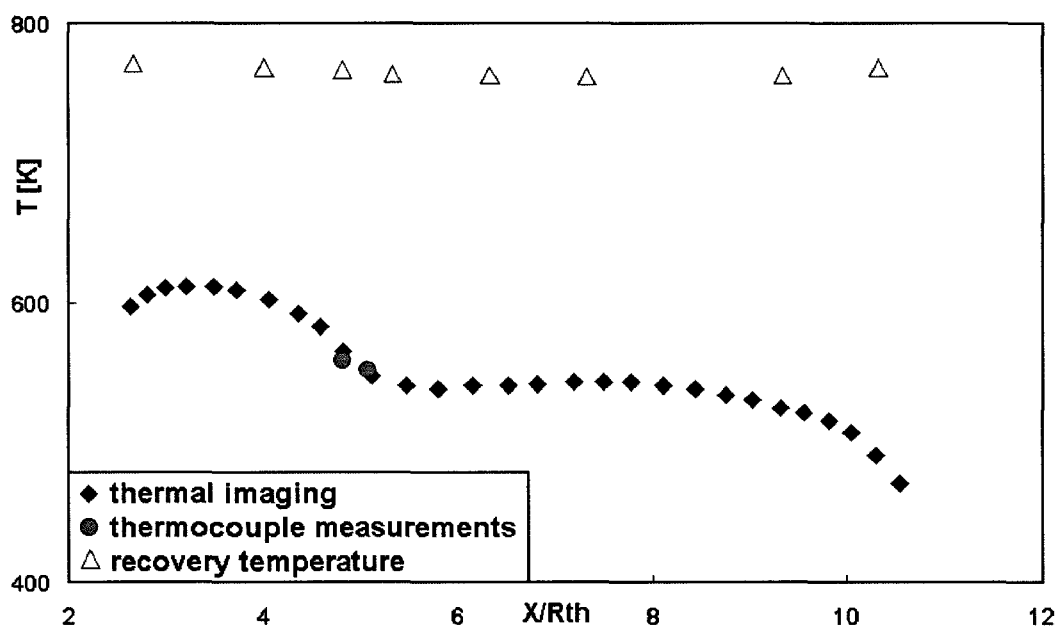


Figure 4.29: Comparison of the inner wall temperature calculated using thermal flux and recovery temperature

### 4.3.5 Conclusion

The temperature measurements made in this study are not sufficient to make any conclusion on the thermal loads acting at the dual bell nozzle wall. A calibration of the thermal loads should be made in a future study.

The difficulties due to the hardware limitation have not permitted to conduct tests under steady state conditions. The duration was too short to reach steady state temperature conditions in the wall.

The thermal imaging measurements give a good distribution and evolution of the outer wall temperature. The region of the inflection (both upstream and downstream) presents a temperature distribution comparable to the temperature in the

base nozzle under both operating modes. Higher thermal loads are then to expect in this area in both sea level and high altitude modes.



# Chapter 5

## Summary and conclusion

Altitude adaptive dual bell nozzles present an interesting alternative for launcher main engine nozzles. The two operating modes allow the flow to adapt to the flight altitude. The transition from sea level to high altitude mode is crucial for the qualification of the nozzle concept.

The dual bell nozzle flow behaviour has been experimentally investigated during cold flow test campaigns. An intermediate state between the two operating modes has been pointed out and defined: the sneak transition, corresponding to the flow attachment in the inflection region during the flow transition from sea level to high altitude mode. Sneak transition takes place independent of the actual transition mode. This flow state is coupled with high side loads and its duration should be reduced.

A transition criterion based on the isentropic relations in the nozzle has been proposed and shows good accordance with the experimental data under cold flow conditions. The theoretical nozzle pressure ratio indicates the flight altitude for the transition from sea level to high altitude mode. The first investigations under warm gas condition has confirmed this criterion. However, the total flow temperature influences the transition point: the transition NPR increases with the temperature.

The parametrical experimental study has pointed out the various parameters of influence and gives information for the optimisation of the dual bell geometry for the needs and limits of a real engine. The sea level performance is defined by the base nozzle geometry, in particular its length. The sea level thrust is higher for a shorter base nozzle. High altitude performance increases with the inflection angle  $\alpha$  and the extension length  $L_{ext}$ .

The altitude of transition is fixed by the geometrical parameters. The transition  $NPR_{trans}$  increases with the inflection angle and the base nozzle length. The recirculation area in the extension under sea level mode depends on the extension length. In a longer extension, the recirculating flow velocity is higher and the pressure decreases. The transition NPR increases for shorter extension geometry. It is now possible to design the transition altitude when optimising the dual bell geometrical parameters.

The critical phenomena for the qualification of dual bell nozzle for main engine applications are the transition duration, the side load generation during the transition and the hysteresis effect between the two operating modes. When increasing the relative extension length  $L' = L_{ext}/L_{tot}$  the hysteresis effect increases. The stability between sea level and high altitude modes is improved: the flow is less sensitive to small pressure variations (combustion chamber or ambient pressure variations). The transition duration can be reduced when increasing the value of the relative extension length. The inflection angle and the base geometry have no significant influence on the transition duration or stability. Two of the most critical effects, transition duration and stability, can be improved by increasing the relative extension length.

The retransition duration slightly increases with the relative extension length increase. However, retransition should only take place during the shut down of the engine in a real case. The chamber pressure would rapidly drop and the retransition duration would be very short.

The flow transition generates a high peak in side loads because of the asymmetrical flow separation in the extension during the transition to high altitude mode. The amplitude of the side loads varies with the nozzle geometry. The amplitude of the peak generated by the transition increases with the relative extension length  $L'$ . The other parameters: inflection angle and base nozzle length have no significant influence on the peak amplitude. The side load generation under sea level mode decreases when increasing the inflection angle. The extension length is the key parameter for the limitation of side load generation in dual bell nozzles.

Furthermore, experimental investigation on side load generation in conventional nozzle [58] has shown an increase in the amplitude of the side loads when the Mach disk is located in the section of the nozzle exit. This effect should also be taken into account for the optimisation of the extension length.

Future investigations planned at the DLR Lampoldshausen are the verification of the

transition criterion under transient hot flow conditions. The influence of the flow temperature on the transition point should be further investigated and quantified in order to precisely predict the influence of cooling on the transition altitude.

A second test campaign on the test bench M11.4 on planar dual bell nozzle will permit the observation of the flow in the inflection region. The evolution of the separation point can be then directly observed and the results of the cold flow test presented in this work can be confirmed. The future objective is the testing of dual bell nozzles under hot flow, with combustion and cooling system, as qualification for flight applications.



# Bibliography

- [1] G. Boerger. *Optimierung von Winkaldüsen für den Unterschallbereich*. PhD thesis, Ruhr-Universität Bochum, 1973.
- [2] H. Ciezki. Determination of concentration and pitot pressure distributions inside a scramjet model combustor with an intrusive probe system. In *2nd European Conference for Aerospace Sciences (EUCASS), 1-6 July 2007, Brussels, Belgium*, 2007.
- [3] D. Dolling. High-Speed Turbulent Separated Flows: Consistency of Mathematical Models and Flow Physics. *AIAA Journal*, 36:pp 725–732, 1998.
- [4] G. Dumnov, G. Nikulin, and N. Ponomarev. Advanced Rocket Engine Nozzles. *AIAA*, (AIAA-96-3221), 1996.
- [5] G. Dumnov, N. Ponomarev, and A. Voinov. Dual Bell Nozzles for Rocket Engines of Launch Vehicle Upper Stages and Orbital Transfer Vehicles. *AIAA*, (AIAA 97-3089), 1997.
- [6] C. Foster and F. Cowles. Experimental Study of Gas-Flow Separation in Overexpanded Exhaust Nozzles for Rocket Motors. *Jet Propulsion Laboratory*, Progress Report 4-103, 1949.
- [7] M. Frey and G. Hagemann. Flow Separation and Side Loads in Rocket Nozzles. *AIAA*, (AIAA 99-2815), 1999.
- [8] M. Frey and G. Hagemann. Restricted Shock Separation in Rocket Nozzles. *Journal of Propulsion and Power*, 16:pp 478–484, 2000.
- [9] M. Frey, A. Preuss, G. Hagemann, S. Girard, Th. Alziary de Roquefort, Ph. Reijasse, R. Stark, K. Hannemann, R. Schwane, D. Perigo, L. Boccaletto, and H. Lambaré. Joint European Effort Towards Advanced Rocket Thrust Chamber Technology. In *6th International Symposium on Launcher Technologies "Flight Environment Control for Future and Operational Launchers"*, Munich, 2005.

- [10] M. Frey, R. Stark, H. Cieski, F. Quessard, and W. Kwan. Subscale Nozzle Testing at the P6.2 Test Stand. *AIAA*, (AIAA 2000-3777), 2000.
- [11] P. Goel and R. Jensen. Numerical Analysis of the Performance of Altitude Compensating Dual Bell Nozzle Flows. *Rocketdyne Division*, 1995.
- [12] G. Hagemann and M. Frey. Dual-Bell Nozzle Flowfield Simulations. *FESTIP WP 3110*, DLR-IB 645-96/23, 1996.
- [13] G. Hagemann, M. Frey, and D. Manski. A Critical Assessment of Dual-Bell Nozzles. *33rd AIAA Joint Propulsion Conference, 6-9 July 1997, Seattle, WA*, (AIAA 97-3299), 1997.
- [14] G. Hagemann, H. Immich, T. Nguyen, and G. Dumnov. Rocket Engine Nozzle Concepts. *AIAA Journal*, pages pp 437–467, 2004.
- [15] G. Hagemann, H. Immich, T. Van Nguyen, and G. Dumnov. Advanced Rocket Nozzles. *Journal of Propulsion and Power*, 1998.
- [16] G. Hagemann, A. Preuss, F. Grauer, M. Frey, J. Kretschmer, R. Ryden, K. Jensen, R. Stark, and D. Zerjeski. Flow Separation and Heat Transfer in High Area Ratio Nozzles. *40th AIAA Joint Propulsion Conference, 11-14 July 2004, Fort Lauderdale, FL*, (AIAA 2004-3684), 2004.
- [17] G. Hagemann, C.-A. Schley, E. Odintsov, and A. Sobatchkine. Nozzle Flowfield Analysis with Particular Regard to 3D-Plug-Cluster Configurations. *AIAA*, (AIAA 96-2954), 1996.
- [18] G. Hagemann, M. Terhardt, D. Haeseler, and M. Frey. Experimental and Analytical Design Verification of the Dual-Bell Concept. *36th AIAA Joint Propulsion Conference, 17-19 July 2000, Huntsville, AL*, (AIAA 2000-3778), 2000.
- [19] F. Haidinger, J. Goergen, and D. Haeseler. Numerical Prediction of Flow Separation for Advanced Nozzle Concepts. *34th AIAA Joint Propulsion Conference, 13-15 July 1998, Cleveland, OH*, (AIAA 98-3368), 1998.
- [20] M. Horn and S. Fisher. Dual-Bell Altitude Compensating Nozzles. *Rocketdyne Division*, (NASA-CR-194719), 1994.
- [21] H. Immich and M. Caporicci. FESTIP Technology Developments in Liquid Rocket Propulsion for Reusable Launch Vehicles. *32nd AIAA Joint Propulsion Conference, 1-3 July 1996, Lake Buena Vista, FL*, (AIAA 96-3113), 1996.

- [22] H. Immich and M. Caporicci. Status of the FESTIP Rocket Propulsion Technology Programme. *33rd AIAA Joint Propulsion Conference, 6-9 July 1997, Seattle, WA*, (AIAA 97-3311), 1997.
- [23] S. Karl and K. Hannemann. Numerical Investigation of Transient Flow Phenomena in Dual-Bell Nozzles. *6th International Symposium on Launcher Technologies, Munich*, 2005.
- [24] T. Kimura, K. Niu, K. Yonezawa, Y. Tsujimoto, and K. Ishizaka. Experimental and Analytical Study for Design of Dual-Bell Nozzles. *45th AIAA Joint Propulsion Conference, 2-5 Aug. 2009, Denver, CO*, (AIAA-2009-5149), 2009.
- [25] H. Kronmüller, K. Schäfer, R. Stark, and H. Zimmermann. Kaltgas-Höhensimulationsprüfstand P6.2 des DLR Lampoldshausen. *DGLR*, 2002.
- [26] A. Kumakawa, H. Tamura, M. Niino, A. Konno, and M. Atsumi. Propulsion Research for Rocket SSTO's at NAL/KRC. *35th AIAA Joint Propulsion Conference, 20-24 June 1999, Los Angeles, CA*, (AIAA 99-2337), 1999.
- [27] K. Kusaka, A. Kumakawa, M. Niino, A. Konno, and M. Atsumi. Experimental Study on Extendible and Dual-Bell Nozzles under High Altitude Conditions. *36th AIAA Joint Propulsion Conference, 16-19 July 2000, Huntsville, AL*, (AIAA 2000-3303), 2000.
- [28] R.A. Lawrence. *Symmetrical and Unsymmetrical Flow Separation in Supersonic Nozzles*. PhD thesis, Southern Methodist University Institute of Technology, 1967.
- [29] D. Manski, G. Hagemann, M. Frey, and G. Frenken. Optimisation of Dual Mode Rocket Engine Nozzles for SSTO Vehicles. *49th International Astronautical Congress, Sept. 28-Oct. 2 1998, Melbourne, Australia*, (IAF-98-S3.08), 1998.
- [30] E. Martelli, F. Nasuti, and M. Onofri. Size Effects on the Transition in Dual-Bell Nozzles. *40th AIAA Joint Propulsion Conference, 11-14 July 2004, Fort Lauderdale, FL*, (AIAA 2004-3999), 2004.
- [31] E. Martelli, F. Nasuti, and M. Onofri. Effect of the Wall Shape and Real Gas Properties on Dual-Bell Nozzle Flowfield. *41st AIAA Joint Propulsion Conference, 10-13 July 2005, Tucson, AZ*, (AIAA 2005-3943), 2005.
- [32] E. Martelli, F. Nasuti, and M. Onofri. Similarity Rules for Dual Bell Nozzle Testing. 2006. rapport preliminaire non-officiel.

- [33] E. Martelli, F. Nasuti, and M. Onofri. Thermo-Fluid-Dynamics Analysis of Film Cooling in Overexpanded Rocket Nozzles. *42nd AIAA Joint Propulsion Conference, 9-12 July 2006, Sacramento, CA*, (AIAA 2006-5207), 2006.
- [34] E. Martelli, F. Nasuti, and M. Onofri. Numerical Parametric Analysis of Dual-Bell Nozzle Flows. *AIAA Journal*, 45(3):pp 640–650, 2007.
- [35] E. Martelli, F. Nasuti, and M. Onofri. Film Cooling Effect on Dual-Bell Nozzle Flow Transition. *45th AIAA Joint Propulsion Conference, 2-5 Aug. 2009, Denver, CO*, (AIAA-2009-4953), 2009.
- [36] M. Miyazawa and H. Otsu. An Analytical Study on Design and Performance of Dual-Bell Nozzles. *42nd AIAA Aerospace Sciences Meeting, 5-8 Jan. 2004, Reno, NV*, (AIAA 2004-380), 2004.
- [37] M. Miyazawa, S. Takeuchi, and T. Kobayashi. Propulsion and Flight Performance Evaluation of Dual-Bell Nozzles. *11th AIAA/AAAF International Conference*, (AIAA 2002-5233), 2002.
- [38] M. Miyazawa, S. Takeuchi, and M. Takahashi. Flight Performance of Dual-Bell Nozzles. *40th Aerospace Sciences Meeting, 14-17 Jan. 2002, Reno, NV*, (AIAA 2002-0686), 2002.
- [39] F. Nasuti and M. Onofri. Flow Analysis and Methods of Design for Dual-Bell Nozzles. *37th AIAA Joint Propulsion Conference, 8-11 July 2001, Salt Lake City, UT*, (AIAA 2001-3558), 2001.
- [40] F. Nasuti, M. Onofri, and E. Matelli. Role of Wall Shape on the Transition in Axisymmetric Dual-Bell Nozzles. *Journal of Propulsion and Power*, (vol. 21, No. 2), 2005.
- [41] L.H. Nave and G.A. Coffey. Sea Level Side Loads in High-Area-Ratio Rocket Engines. *AIAA*, (73-1284), 1973.
- [42] C. Nürnberger-Génin and R. Stark. Experimental Study of Dual Bell Nozzles. *2nd European Conference for Aerospace Sciences (EUCASS), 1-6 July 2007, Brussels, Belgium*, 2007.
- [43] C. Nürnberger-Génin and R. Stark. Flow Transition in Dual Bell Nozzles. *Shock Waves Journal*, 2008.
- [44] C. Nürnberger-Génin and R. Stark. Experimental Study on Flow transition in Dual Bell Nozzles. *45th AIAA Joint Propulsion Conference, 2-5 Aug. 2009, Denver, CO*, (AIAA 2009-4855), 2009.

- [45] J. Oestlund, T. Damgaard, and M. Frey. Side-Load Phenomena in Highly Overexpanded Rocket Nozzles. *Journal of Propulsion and Power*, 20(4):pp 695–704, July-August 2004.
- [46] M. Onofri, F. Nasuti, and E. Martelli. Analysis of the Transition Process in Dual-Bell Nozzles. *Abstract for 4th International Conference on Launcher Technology Space Launcher Liquid Propulsion*, 2002.
- [47] H. Otsu, M. Miyazawa, and Y. Nagata. Design Criterion of the Dual-Bell Nozzle Contour. *56th International Astronautical Congress, 17-21 Oct. 2005, Fukuoka, Japan*, (IAC-05-C4.2.08):pp 4491–4496, 2005.
- [48] D. Perigo, R. Schwane, and H. Wong. A Numerical Comparison of the Flow in Conventional and Dual-Bell Nozzles in the Presence of an Unsteady External Pressure Environment. *39th AIAA Joint Propulsion Conference, 20-23 July 2003, Huntsville, AL*, (AIAA 2003-4731), 2003.
- [49] G. Rao. Exhaust Nozzle for Optimum Thrust. *Journal of Jet Propulsion*, 26:pp 377–382, 1958.
- [50] G. Rao. Nozzle Contours. *Journal of Propulsion*, 20:pp 69–75, 1960.
- [51] P. Reijasse, D. Coponet, J-M. Luysen, V. Bar, S. Palerm, J. Oswald, F. Amouroux, J-C. Robinet, and P. Kuszla. Wall Pressure and Thrust of a Dual Bell Nozzle in a Cold Gas Facility. *3rd European Conference for Aerospace Sciences (EUCASS), 6-9 July 2009, Versailles, France*, 2009.
- [52] G. L. Romine. Nozzle Flow Separation. *AIAA Journal*, 36:pp 1618–1625, 1998.
- [53] K. Schaefer, H. Zimmermann, V. Schmidt, D. Suslov, and R. Stark. Advanced Nozzle Testing in Flight Conditions. *AIAA*, (AIAA 2006-4372), 2006.
- [54] F. Scheel, H. Ciezk, and O. Haidn. Investigation of the influence of streamwise vortices generating geometries of strut injectors on the mixing and combustion process in a scramjet model combustor. In *18th International Symposium on Airbreathing Engines, Beijing, China*, 2007.
- [55] R. Schmucker. Strömungsübergänge beim Betrieb überexpandierender Düsen Chemischer Raketenantrieb. *Berichte TB7 und TB 10, Technische Universität München*, 1973.
- [56] R. Stark. Flow Separation in Rocket Nozzles, a Simple Criteria. *AIAA*, (AIAA 2005-3940), 2005.

- [57] R. Stark, C. Boehm, O. Haidn, and H. Zimmermann. Cold Flow Testing of Dual-Bell Nozzles in Altitude Simulation Chambers. In *1st European Conference for Aerospace Sciences (EUCASS), 4-7 July 2005, Moscow, Russia*, 2005.
- [58] R. Stark and B. Wagner. Experimental Study of Boundary Layer Separation in Truncated Ideal Contour Nozzles. *Shock Waves Journal*, (DOI 10.1007/s00193-008-0174-6), 2008.
- [59] G. Sutton and O. Biblarz. *Rocket Propulsion Elements*. Wiley-Interscience, 7th edition edition, 2001.
- [60] M. Terhardt, G. Hagemann, and M. Frey. Flow Separation and Side-Load Behavior of Truncated Ideal Rocket Nozzles. *AIAA*, (AIAA 2001-3686), 2001.
- [61] T. Tomita, M. Takahashi, M. Sasaki, and H. Tamura. Investigation on Characteristics of Conventional-Nozzle-Based Altitude Compensating Nozzles by Cold-Flow Tests. *42nd AIAA Joint Propulsion Conference, 9-12 July 2006, Sacramento, CA*, (AIAA 2006-4375), 2006.
- [62] L. Torngren. Flow Separation Tests on Several Different Nozzles Suspended in a Universal Joint. *F.F.A. Project*, AU-4911, AE-4931, 1999.
- [63] S. Verma, R. Stark, C. Nürnberger-Génin, and O. Haidn. Flow Separation Studies During the Transition Modes of a Sub-Scale Dual-Bell Nozzle. *45th AIAA Joint Propulsion Conference, 2-5 Aug. 2009, Denver, CO*, (AIAA-2009-4854), 2009.
- [64] H. Wong and R. Schwane. Numerical Investigation of Transition in Flow Separation in a Dual-Bell Nozzle. In *4th International Conference on Launcher Technology - Space Launcher Liquid Propulsion, Liege, Belgium*, 2002.
- [65] M. Zheng, Y. Wang, and Y. Liu. Research for Dual-Bell Nozzle. In *International Symposium on Space Propulsion, 8-12 Oct. 2007, Beijing, China*, 2007.
- [66] Zucrow and Hoffman. *Gas Dynamics*, volume 2. Robert Krieger Publishing Company, 1977.



## **Etude expérimentale de l'écoulement et des charges thermiques dans une tuyère dual bell**

Les tuyères sont actuellement le sous-système présentant les possibilités d'optimisation les plus prometteuses pour répondre aux besoins toujours croissants de l'industrie aérospatiale. Les tuyères dual bell permettent une adaptation à l'altitude. L'écoulement est forcé à décoller de façon stable et symétrique à l'inflexion, générant ainsi une poussée optimisée pour le fonctionnement à basse altitude. Au cours du vol, lorsque la pression atmosphérique chute sous une certaine valeur, l'écoulement attache soudainement dans toute la tuyère, permettant une détente plus importante pour une poussée plus élevée.

L'étude présentée dans ce document a été réalisée au DLR (centre aérospatial Allemand) dans le cadre d'un travail de thèse. Il s'agit d'une étude fondamentale visant à comprendre le comportement de l'écoulement dans une tuyère dual bell, afin de mettre en évidence les paramètres d'influence. Une série de tests en gaz froid a été réalisée sur différentes géométries de tuyères. Des mesures de pression ainsi qu'une observation de l'écoulement à l'aide d'une méthode stéréoscopique de schlieren a permis de conclure sur l'influence de la géométrie sur le déroulement de la transition d'un mode de fonctionnement à l'autre, sa durée et sa stabilité face aux variations de pression. Une série de tests en gaz chaud a permis de réaliser des relevés de température et pression afin d'étudier les charges thermiques dans la paroi au voisinage de l'inflexion.

**Mots clés:** écoulement de tuyères, dual bell, contrôle de la séparation, adaptation à l'altitude

## **Experimental study of flow behaviour and thermal loads in dual bell nozzles**

The nozzle are currently presenting the most promising optimisation possibilities to supply the increasing needs of the aerospace industry. The dual bell nozzles allow the altitude adaptation of the flow. The inflection forces the flow to a stable and symmetrical separation, generating an optimised thrust for sea level operation. During the flight, when the ambient pressure decreases under a certain value, the flow suddenly attaches the nozzle wall down to the nozzle end, generating a higher expansion for higher performance.

The study presented in this document was made at the DLR (German Aerospace Center) as part of a PhD. This fundamental study has for objective the understanding of the flow behaviour in a dual bell nozzle, in order to define the various parameters of influence. A cold flow test series has been conducted on various nozzle geometries. Pressure measurements have been made and the flow has been observed with schlieren optics in order to determine the influence of the geometry on the evolution of the flow transition from one operating mode to the other, its duration and stability toward pressure variations. Temperature and pressure measurements were also made during a test series under warm gas conditions to investigate the thermal load in the vicinity of the wall inflection.

**Keywords:** nozzle flow, dual bell, flow separation control, altitude adaption

Bibliothèque Universitaire de Valenciennes



00900672